MODELING OF GROUND DEFORMATION USING SPATIAL ANALYSIS AND ELASTO-PLASTIC FINITE STRAIN THEORY

by

Jianping Hu

A Dissertation Presented to the
FACULTY OF THE GRADUATE SCHOOL
UNIVERSITY OF SOUTHERN CALIFORNIA
In Partial Fulfillment of the
Requirements for the Degree
DOCTOR OF PHILOSOPHY
(CIVIL ENGINEERING)

May 2004

ProQuest Information and Learning Company
300 North Zeeb Road
P.O. Box 1346
Ann Arbor, MI 48106-1346

Acknowledgements

I would like to express my deepest appreciation and profound gratitude to my academic adviser and dissertation committee chair, Dr. Jean-Pierre Bardet for his guidance, encouragement and helpful suggestion during the course of this investigation. Without his guidance and support based on deep insight and experience on the subject, I could not have completed the present work.

I would like to extend my sincere gratitude to the other members of dissertation committee; Dr. Geoffrey R. Martin, Dr. L. Carter Wellford, and Dr. Cyrus Shahabi for their constructive suggestions and active discussions.

I would like to acknowledge past and present members of the Research Center for Computational Geomechanics and other laboratories, with special mention to Dr. Tetsuo Tobita, Yangsoo Lee, Andy M. Dodds, Jamal Ramadan, Dr. Jennifer Swift, Dr. Craig Davis, Rana Al-fares, and Dr. Nicholas Mace. I also appreciate the support from the staff in the Civil Engineering Department at the University of Southern California.

My family has been a constant source of love, encouragement, and support throughout my graduate studies and my life. I am grateful to my parents and sister for their love, patience, and understanding over the last five years. Another special thanks to my wife, Wei Zhang for her love, encouragement, and happiness she has provided through all the years, and my daughter, Jenny Hu, the little angel to whom I dedicate all my love.

Table of Contents

List of Tables

List of Figures

Abstract

Earthquake-induced ground deformation is a type of permanent ground displacement observed extensively after the earthquakes. Anywhere from a few centimeters to several meters of lateral permanent displacements have been reported over large area. This caused substantial damage to lifelines and pile-foundations of buildings and bridge piers. The research work in this dissertation considers the different aspects of ground deformation induced by earthquake shaking.

Firstly, the advanced information technologies are exploited to document the case histories of earthquake-induced ground deformation. Two databases, Liquefaction-Induced ground Deformation Database (LIDD) and Borehole Database (BOD), have been constructed. A Web service architecture for promoting the exchange and utilization of geotechnical information is presented. These well-documented case histories help us to develop and improve methods for assessing and quantifying the liquefaction potentials of ground deformation.

The second part investigates the uncertainties in modeling the ground deformation over large area using empirical model. Geostatistical tools are utilized to investigate the spatial correlations of model parameters and estimate them over regional areas. The uncertainty of empirical model prediction is evaluated spatially using the geostatistical tools. The methodology for predicting liquefaction-induced ground deformation over large areas is presented and illustrated using a case study in Port Island, Kobe after the 1995 Hyogoken-Nanbu earthquake.

The third part of this research compliments the empirical and geostatistical approach by studying the physics of the ground deformation using modern approaches in continuum mechanism and numerical methods. The finite strain elasto-plastic J2 finite model and nonlinear finite elements procedure considering geometrical nonlinearities are formulated and implemented in a nonlinear finite element program to investigate the liquefaction-induced ground deformation. The transition from the initial configuration to the final equilibrium state is simulated using a dynamic analysis, which accounts for kinetic energy effects. The applicability of the implemented FE method to engineering is investigated in the case history of the Upper San Fernando Dam during the 1971 San Fernando Earthquake.

1 INTRODUCTION

1.1 Background on lateral ground deformations

Earthquakes are among the most disastrous natural phenomena that mankind may face without appropriate engineering countermeasures. Earthquake may cause tremendous damage to structures and take thousands of human lives. Past earthquake caused many millions or even billions of dollars in damage to infrastructures in addition to the human suffering. In the 1995 Hyogoken-Nanbu (Kobe) earthquake, the total cost of direct lost was estimated as \$100 ~ \$150 billion (Hamada et al. 1996a). One of the main causes of damage to structures and man-made facilities was the failure, cracking and permanent displacement of the ground, which associated with strong ground shaking. This caused substantial damage to lifelines and pile-foundations of buildings and bridge piers. It is of prime importance to evaluate and mitigate this hazard by determining how and how much the ground will deform, and establishing what displacements or deformations are acceptable to constructed facilities.

Liquefaction-induced ground deformation is a type of permanent ground displacement observed extensively after the earthquakes. It is defined as lateral spreading when the ground has a gentle slope and there is no structure on top (e.g., Kramer 1996). Anywhere from a few centimeters to several meters of lateral permanent displacements have been reported. Cumulatively, more damage has been caused by lateral spreads than by any other form of liquefaction-induced ground failure. During the 1964 Alaska earthquake, more than 250 bridges were damaged due to liquefaction-induced lateral spreading. Hamada et al. (1986) measured ground deformations in Noshiro City, Japan, after the Nihonkai Chubu Earthquake in 1983. When the 1971 San Fernando earthquake hit the Van Norman Complex in San Fernando Valley, which has water facilities belongs to Los Angeles Department of Water and Power (LADWP), severe damage was observed for buried conduits, including water supply, gas, liquid fuel, and water pipeline (Hamada and O'Rourke 1992). Damage from large ground deformation resulted in the loss of gas supply to 17,000 customers. In the same area of Van Norman Complex, sand boils, liquefaction induced lateral spreading, and ground cracks were observed during the 1994 Northridge earthquake (Davis and Bardet 1996). The damage caused by ground deformation to both water and power facilities was estimated to exceed $75M. The 1995 Kobe earthquake caused significant soil liquefaction in an extensive area of reclaimed land in Kobe and its neighboring cities. The liquefaction-induced ground deformation resulted in serious damage to buried lifeline facilities and foundations of constructions. Numerous quay walls have been damaged due to the ground deformation as large as 5 m in magnitude along the Kobe Port Island (Iai et al., 1997; Tokimatsu et al., 1996).

Shaking table tests and centrifuge tests have shown that permanent displacement stops when shaking is terminated (e.g., Fiegel and Kutter 1994). This may suggest that the cyclic mobility of liquefied soil determines the permanent deformation. In contrast to this assumption, there are observations that the deformation of liquefied soils can continue after the end of shaking when the sand density is extremely low (Towhata et al. 1997). The lateral flow along the Shinano River dike during the 1964 Niigata earthquake destroyed the foundation of a bridge after the end of shaking (Horii 1968). Seed et al. (1975) reported that the failure of the Lower San Fernando dam occurred after the shaking ended.

1.2 Review of past work

Many methods, either experimental or numerically have been used to investigate the ground deformation. Hereafter, these methods are briefly reviewed (Bardet et al. 1999b).

1.2.1 Experimental study of lateral ground deformations

Shaking table test

Liquefaction-induced lateral deformations were extensively investigated using shaking tables (Sasaki et al. 1992; Towhata et al. 1997). In these types of experiments, a reduced-scale model of soil deposits is subjected to short pulses or continuous time history of acceleration simulating the earthquake ground motion. The acceleration, pore pressure, and displacement are measured at various locations in the reduced-scale model.

A 1D model of saturated loose sand with a seam of silt sandwiched in it was investigated by Kokusho (1999) to understand water film effect on lateral spread. 2D shaking table model test shows that the deformations of sand take place even after the shaking ends, by exploiting some part of water films. This gives clues to explain case histories that lateral spread or slope failure was witnessed not only during but also after earthquake shaking. Several small scale and large scale shaking table tests were conducted to focus on the thickness of liquefied layer, the surface slope and the inclination of the bottom plane of liquefied layer (Sasaki et al. 1992), which aimed at understanding of the basic nature and mechanism of the ground displacement.

Results from shaking table test, combined with field observations remark that 1) permanent displacement is influenced by gravity force, 2) liquefied material behaves similarly to viscous flow, 3) volume of liquefied material keeps constant during lateral flow, and 4) the overall topography of regional area will effect the final displacement, so do the boundary condition.

Centrifuge test

The interpretation of lateral spread with centrifuge experiments is described by Dobry et al. (1995). Centrifuge modeling is very useful for simulation of effects of earthquakes on geotechnical structures. The principle is to produce stresses, strength, and stiffness of small-scale model that are similar to those in a prototype by obeying the scaling raw.

Taboada and Dobry (1998) use centrifuge modeling to study the influence of the ground surface topography (slope), as well as of the intensity and frequency of the shaking on the measured lateral displacement. It is found that if thickness of liquefied layer is considered, lateral displacement only depends on slope and thickness of liquefied layer, with no influence of peak acceleration and frequency. A series highly instrumented centrifuge models have been tested to study the settlement, sliding and liquefaction remediation of layered soil by Balakrishnan & Kutter (1999).

Typical centrifuge results indicate that 1) the lateral ground deformation is associated with unsymmetrical spikes of ground acceleration in the downhill direction, 2) there are negative pore pressure spikes which increase the effective stress and stop the downhill ground deformation (soil dilatancy), 3) the lateral ground deformation does not continue after the shaking, and 4) the lateral displacement and the thickness of the liquefied layer decreases with relative density.

1.2.2 Numerical analysis of lateral ground deformation

Permanent lateral deformation in soil subjected to earthquake induced strong shaking is a very difficult nonlinear problem. Intensive research efforts on the liquefaction-induced ground deformation are currently underway. Based on field observation and experiment study, several numerical analysis methods, either empirically or analytically, have been proposed to predict the ground displacement.

Empirical methods

Most of the empirical methods for predicting lateral ground deformation are proposed using regression analysis based on the observed displacement data set. Youd and Perkins (1987) proposed LSI (Liquefaction Severity Index) model. It relates the amplitude of horizontal ground deformation to distance from seismic energy source and moment magnitude. Based on aerial photo data and field observation, Hamada et al (1986) predict the amplitude of horizontal ground deformation only in terms of slope and thickness of liquefied layer. Based on the collected liquefaction-induced case histories data up to 1992, Bartlett and Youd (1992) proposed a multiple linear regression model to predict the permanent lateral ground deformation for both ground slope of infinite extent and the free face scenario. The model combines the parameters of earthquake magnitude, source distance, liquefied layer thickness, soil particle size and fine content to represent the earthquake motion and local soil conditions. Rauch (1997) considered liquefaction-induced ground deformation as slides of finite area, instead of individual displacement vectors. He applied multiple-linear-regression methods to these liquefaction-induced slides. Rauch proposed three different models for the average lateral ground displacement, which are referred to as regional, site and geotechnical.

Bardet et al. (1999b, 2002) reevaluated the previous regression model from Bartlett & Youd and proposed a four-parameter MLR model to provide a first-order approximation of liquefaction-induced displacement. This model simplified Bartlett & Youd formula by eliminating 2 parameters with the assumption that some soil parameters, such as fines content and grain size corresponding to 50 % finer, might not be available or very scattered over a large area where liquefaction-induced ground deformation is concerned. They also probabilistically estimated the magnitude of lateral spread exceeding certain range.

Empirical relationships are valuable as they directly include the intangible aspects of field response. They are often limited to specific topographic and material conditions. Most of the empirical methods treat the observed displacement as independent event. In reality, lateral ground deformation are distributed spatially associated with topographic and local soil condition. Spatial correlation must be taken into account to evaluate the observed data using regression analysis.

Newmark sliding block

As a simplified model, sliding block analysis (Newmark 1965) is widely used to evaluate permanent displacements related to slope failure and lateral spreads under earthquake shaking. Newmark sliding block assumes that soil is rigid and slides when acceleration due to shaking exceeds certain yield condition, which corresponds to factor of safety one against slope instability. Several models have been proposed based on the concept that Newmark (1965) developed for calculating the deformation of earth dams during earthquakes. Yegian et al. (1991) proposed that the amplitude D of permanent displacement. Baziar et al. (1992) proposed that D depends on peak velocity. Jibson (1994) proposed that D (cm) depends on the Aria intensity. Byrne (1991) modified the concept of the sliding block to include displacements resulting from softened soil. Byrne et al. (1992) extended the method in two dimensional analyses.

The models based on Newmark sliding blocks assume that the deformation takes place on a well-defined failure surface, the yield acceleration remains constant during shaking, and the soil is perfectly plastic. However, these assumptions do not hold in the case of liquefied soils and lateral spreads, because (1) the shear strain in liquefied soil does not concentrate within a well defined surface, (2) the shear strength (and yield acceleration) of saturated soils varies during cyclic loading as pore pressure varies, and (3) soils are generally not perfectly plastic materials, but commonly harden and/or soften. Also original sliding block model considers only the longitudinal component of earthquake excitation. The investigation has addressed to consider three components excitation for Newmark model (Elms 2000).

Constitutive modeling

Constitutive models used to predict lateral ground deformations are usually based on plastic theory in terms of effective stress, the Biot dynamic consolidation theory, and a finite element or finite difference computer program with step-by-step time integration (e.g., Zienkiewicz et al. 1990). Nonlinear effective stress methods have been formulated for more advanced analyses (e.g., Dafalias and Hermann 1982; Bardet 1986 and 1995; Adachi and Oka 1982; and Tateishi et al. 1995). Effective stress models are largely based on nonlinear finite element solution of small-strain transient consolidation. There are several constitutive models that reproduce important aspects of the dilative shear mechanism currently available (Iai 1991, Yang 2000).

Energy model

Byrne (1991) extended the concepts of Newmark sliding block by introducing a resisting force varying with displacement. The mass *M* with an initial velocity *V* is subjected to a driving force *D* due to the gravity and slope inclination α, and a resisting force *R*. The mass stops when the initial kinetic energy (i.e., $MV^2/2$) is dissipated by the resisting force *R*. Byrne's method requires the selection of a final residual shear strength S_R and limiting strain γ_R.

Byrne (1997) proposed to calculate the final position of a slope that liquefies by using the finite difference program FLAC (1995). The initial kinetic energy is dissipated by soil resistance. Dynamic equation of motion has been employed to calculate the final position of slope. In the zone of liquefaction, the material is assumed to be free of shear stress initially. Following onset liquefaction, the shear stress is assumed to increase with shear strain until it reaches some residual shear strength.

Towhata et al. (1997) developed a minimum potential energy model to predict the possible maximum ground movement. Soil layers of irregular shape are divided into vertical slices in which the lateral displacement is assumed to vary as a sine function with depth. The model determines the final position of the soil layers that liquefy by invoking the principle of minimum potential energy. The model also predicts the variation of displacement with time by using Lagrangian equations of motion. The model was successfully applied to model various shaking table test results.

1.3 Research objectives

The case histories of earthquake-induced ground deformation, with the underground soil information, are very important data sets to understand fully the mechanism of permanent ground deformation. Tremendous amount of earthquake-induced ground deformation have been measured through ground survey and aerial photo measurements after several devastating earthquakes (Hamada and O'Rourke 1992, Bartlett and Youd 1992, Bardet et al. 1999a). It is becoming complicated to manage and utilize efficiently the data sets with the increasing volume and diversity data types including earthquake data, topographic information and geotechnical data. The first objective of the present research is to take advantages of the modern information technology to document the case histories of the ground deformation from the past earthquakes. Modern information technologies such as database, GIS and Web Service will be utilized to construct infrastructures of ground deformation data and geotechnical information storage and exchange system. The well documented case histories of ground deformation will help us to develop and improve methods for assessing and quantifying the liquefaction potentials of ground deformation, and ultimately to produce deterministic/probabilistic models of liquefaction-induced ground displacement useful for seismic zoning, estimating the cost of damage and repair to lifeline distribution networks and preventing catastrophic damage of building foundations during future earthquakes.

Liquefaction-induced ground deformation was observed after earthquakes to cover areas as large as a few square kilometers. Empirical models of ground deformation (Hamada et al. 1986, Bartlett and Youd 1992, Ranch 1997, Bardet et al. 1999b and 2002, Youd et al. 2002) offer the most pragmatic approach for predicting the liquefaction-induced ground deformation over large areas due to their limited number of model parameters. They can be applied for mapping areas prone to deformation due to liquefaction during future earthquakes. The use of empirical models for mapping ground-deformations hazards raises many questions. For instance, can empirical models, although based on spatially unrelated data, describe the spatial variation of ground deformation? What are the uncertainties of empirical model in predicting liquefaction-induced ground deformation? The second objective of the present research will investigate the uncertainties in modeling the ground deformation over large area from the empirical models. A methodology for predicting earthquake-induced ground deformation will be proposed to study spatial variation of the model parameters and the uncertainty of the empirical model.

The detail mechanism of liquefaction-induced ground deformation is still not clear for us although fair good understanding has been established for liquefaction. Much research work has been devoted to understanding the ground displacements induced by liquefaction after earthquakes (e.g., Ishihara 1996). Instability occurs in the liquefied soil when the shear strength required to maintain equilibrium of a soil deposit is less than the applied the shear stresses due to gravity. The soil then deforms until it reaches a configuration in which the applied shear stresses do not exceed the shear strength. The amount of deformation required to reach a stable configuration is strongly influenced by the difference between the applied shear stresses and the available shear strength of the liquefied soil. Very few analyses account for the gravity effects caused by large amount of deformation, i.e., change in gravity-induced shear stress decrease with the development of deformation (e.g., Towhata et al. 1997). One of the objectives of the present research is to study the mechanism of ground deformation using modern approaches in continuum mechanics and numerical methods. The third objective of the research investigates liquefaction-induced ground deformation in the framework of nonlinear finite elements and finite deformation plasticity, and studies the effects of geometrical nonlinearities on ground deformation processes. The applicability of the proposed method to engineering is investigated in the case of well-documented case histories of liquefaction-induced ground deformation.

1.4 Organization of present work

The liquefaction-induced ground deformation and geotechnical information database have been introduced in Chapter 2. The design and construction of the geotechnical database is first explained. The detailed data structure and data dictionary for geotechnical information including geotechnical boring, CPT sounding and displacement vector are defined. Several liquefaction-induced ground deformation case histories are included in this database and the content of the database is summarized. A geotechnical data exchange format based on eXtensible Markup

Language (XML) has been proposed to store and exchange the existing geotechnical data. Furthermore, a system architecture called GIME which emerging Web services standard has also been proposed to build infrastructures in the geotechnical and other distributed data integration projects. This system handles geotechnical data via an XML format on a distributed platform that interoperates via Web services.

Chapter 3 proposes the detailed methodology of ground deformation prediction using the geotechnical information managed in the database. This methodology utilizes the empirical Multiple Linear Regression (MLR) model to predict the magnitude of lateral ground movement. The geostatistics tools for spatial analysis over large areas to access the geotechnical parameters of prediction have been addressed. Following that, the uncertainty of ground deformation predication has been discussed to consider the spatial interpolation error and empirical MLR model error. The applicability of the methodology has been examined in a case study in Port Island of Kobe city, Japan, after the 1995 Hyogoken-Nanbu earthquake.

The numerical algorithm based on finite strain elasto-plastic theory has been introduced in Chapter 4 to investigate the large ground deformation. This chapter will review the basic concepts of continuum mechanics which help to understand the effect of large deformation in liquefaction-induced ground deformation analysis. The general concept of strain and strain rate measurement in nonlinear continuum mechanics is presented. Different measurements of stress and objective stress rates, which are commonly used in large deformation computations, are reviewed. The general procedure for finite strain elasto-plasticity model has been summarized based on hypoelastic theory.

Chapter 5 applies the finite strain elasto-plastic theory to implement the finite element procedure. GEOFEEX, an existing finite element program developed by Bardet (1986), is extended to large deformation computation. A generalized J2 elasto-plastic model is first introduced with the radial return algorithm for numerically integration. The strong and weak formulation for boundary value problems in finite strain has been examined to take into account material and geometrical nonlinearities. Explicit dynamic computation method has been exploited to solve for the high nonlinear system driven by gravity force and very low shear resistance in liquefied soil. Several simulation problems have been solved using the implemented large strain finite element computation. The case history of the Upper San Fernando Dam deformation analysis has been conducted to demonstrate the usage of this nonlinear finite element method.

Finally, conclusion is presented in Chapter 6.

2 DATABASE OF CASE HISTORIES OF EARTHQUAKE-INDUCED GROUND DEFORMATION

2.1 Introduction

Liquefaction-induced ground deformation data, upon with the geotechnical information such as borehole data, are the very important data that help to fully understand the mechanism of permanent ground deformation (PGD). These type of critical resource will help us to develop and improve methods for assessing and quantifying the liquefaction potentials of ground deformation, and ultimately to produce deterministic/probabilistic models of liquefaction-induced ground displacement useful for seismic zoning, estimating the cost of damage and repair to lifeline distribution networks and preventing catastrophic damage of building foundations during future earthquakes.

Tremendous geotechnical information has been generated from field investigation, laboratory test and engineering analysis. The best choice is to use database management system to store and organize the tremendous amount of data. Consequently with the blast of information science, specially combined with geographic information system (GIS), research activity based on geotechnical database has been speed up. Nowadays GIS-based hazard estimation using database has been applied extensively in local or regional earthquake analysis (Friberg et al. 1991, Borcherdt 1993, Doroudian et al. 1996). GIS-based database system can be used to map earthquake hazard zonation, predict liquefaction potential, and monitor the landslide hazard. All these analysis should be supported by a completely geotechnical database. Academic, government, agency have extensively used GIS tool, but still not so many work to be carried out to describe the standard and structure of geotechnical database system. It is inconvenient to communicate between all these databases. It is necessary to design a geotechnical database, which has a consistent data structure and compatible data format that data can be easily retrieved and exchange according to different purpose of the projects through different organizations.

This chapter describes the research efforts focused on the storage and exchange of high-quality case histories of geotechnical information and liquefaction-induced ground deformation including those from the 1994 Northridge and 1995 Hyogoken-Nanbu earthquakes. The specific objectives of the research are:

(1) Identify, collect, organize and digitize the existing data sets on liquefaction-induced ground displacement including those from the 1994 Northridge earthquake and 1995 Hyogoken-Nanbu earthquake.

(2) Develop a relational database framework capable of hosting the large amount of data on liquefaction-induced ground deformation and geotechnical borehole information.

(3) Propose system architecture for geotechnical data exchange and dissemination through Internet using Web Services and XML data format.

The research activities were divided into three main branches entitled data processing, GIS based RDBMS developing and geotechnical data exchanging and management. This chapter will describe the tasks and results of the three branches. Following the introduction, the second section describes the lengthy data processing procedure, which consists of the identification, selection, collection, documentation, scanning, and preparation of data on liquefaction-induced ground deformation from various sources. The third section presents the construction and contents (RDBMS) of the databases – Liquefaction-Induced ground Deformation Database (LIDD) and Borehole Database (BOD), which contain a large amount of geotechnical borehole and liquefaction-induced ground deformation during several past earthquakes. The GIS platform will be introduce to visualize, maintain and model the databases LIDD and BOD by combining the digital ground elevation models and base maps of the case histories of liquefaction-induced ground deformation. The last section proposes a distributed platform that interoperates via Web services for exchanging and utilizing geotechnical information using the eXtensible Markup Language (XML) format.

This chapter summarizes the research efforts solely devoted to ground deformation database development and exchange. The modeling and analysis of these data will be presented in the next several chapters.

2.2 Data processing phase

The first and critical step in the creation of a database of case histories on liquefaction-induced ground deformation and corresponding geotechnique data is the data processing phase. There are a number of steps that need to be undertaken before any data is ready for entry into computer databases. In addition, with a project of this size and scope, it is imperative to keep track of a large volume of incoming data, i.e., hardcopy documents and drawings. The basic procedure is outlined in Figure 1. It has four stages as detailed below.

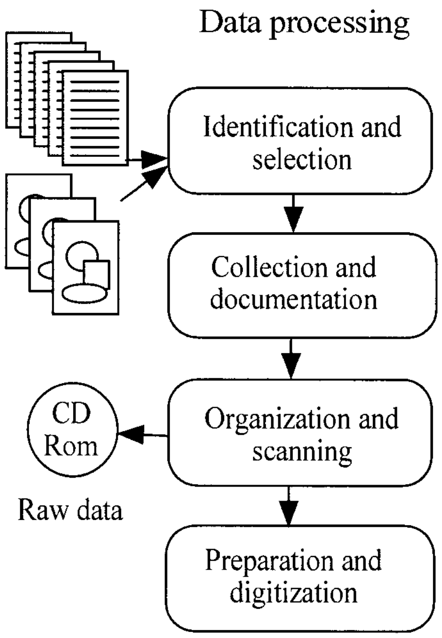

Figure 2-1. Main steps in processing data on case histories of liquefaction-induced ground deformation.

Data identification and collection are fundamental parts of database process. Which kind of data should be identified and selected into database is depended on purpose of geotechnical data management system. Boring database should include borehole information, soil properties and so on, while ground deformation database needs information of topology, displacement vector that boring database will not supply. Some times more data does not always mean better comprehensive ground truth. The basic prerequisite for including case histories in the database is the availability of information on ground deformation. Five main categories of data are defined for this study:

- Displacement vector – location, magnitude and direction of ground deformation
- Soil investigation data
  - CPT – cone penetration test data
  - Borehole – borehole test data (including SPT, soil samples etc.)
- Seismic data – main earthquake characteristics
- Ground elevation models
- Base maps and aerial photographs – raster image of sites of interest

Displacement vector can be obtained either through ground survey or aerial photogrammetry. The soil investigation data includes data characterizing local geotechnical subsurface conditions, i.e., cone penetration data and standard penetration data. The third category describes the main earthquake characteristics, (e.g., magnitude, epicenter location, and type of fault rupture mechanism). The fourth category is about digital ground elevation models (such as DEM), which give information on ground-slope and free-face conditions – one of the main physical parameters controlling liquefaction-induced ground deformation (e.g., Bardet et al. 1999b). The last category includes base maps and aerial photographs, which are most useful to represent and analyze data with GIS tools, as explained in a later section.

Having selected the types of data of interest, the next step in the process is to identify suitable sources for data. In this present study, eight case histories listed in Table 1 were considered for inclusion in the database. It was decided to retain only those case histories that can be supported with original data (e.g., borehole logs from original ground investigation reports). This is to ensure that the data in the database can be directly traced back to the source of data as originally measured and reported. This direct link is critical for examining the original data, should some doubts or conflicts arise about some data. This link also guarantees that the data is free from analysis and assumptions as much as possible. The direct-link criterion for data inclusion is intended for verifying that data has been correctly entered in databases and meets certain quality standards.

Table 2-1. Earthquakes considered for inclusion in databases of case histories of liquefaction-induced ground deformations.

Japan	US
1964 Niigata	1971 San Fernando
1983 Nihonkai-Chubu	1979 Imperial Valley
1995 Kobe	1987 Superstition Hills
	1989 Loma Prieta
	1994 Northridge

For US case histories, most of the data were obtained through organizations such as the US Geological Survey (USGS) and the Los Angeles Department of Water and Power (LADWP). For the Japanese case histories, the assistance of Prof. Hamada of Waseda University has been invaluable. It is clear that Japanese researchers have devoted a lot of time and effort into compiling data for studies similar to this one. Data obtained from various sources (including organization, agency and personal) should integrate and validate and make the results readily available for analyses and models. The procedure includes checking the data for completeness and quality, and loading it into the technical database. Data collected from different agency, public and private usually come with all kinds of format, and most of them are hardcopy reports or drawings, with fewer in electronic form, which greatly aids the data processing procedure. Various methods, such as scanning and digitizing, are employed depending on the form of the original data. Electronic data-loading tool should be developed to support the easy and fast data entry, ensuring that the data are sufficient quality to support the analysis and models. Data quality control has been carried on this step to evaluate the quality of data set. Depending on the particular purpose of data set application, different kinds of data quality control can be adopted.

2.3 GIS based Relational Database Management Systems

The previous section identified and processed a large volume data from several case histories on liquefaction-induced ground deformation. Such a large volume of data can only be handled and utilized using relational database management systems

(RDBMS). RDBMS organizes and links a large amount of relevant data from various origins, and allows data to be queried to extract smaller data sets relevant to specific analyses including analysis of relationships among various variables and data visualization using Geographic Information Systems (GIS).

Two separated databases, the Liquefaction-Induced ground Deformation Databases (LIDD) and BOrehloe Database (BOD) have been developed using Microsoft Access (Viescas 1997). Microsoft Access was selected because it is readily available on most computers and can make direct connection with GIS. The choice of a particular RDBMS is not critical provided that it is compatible with other RDBMS. This section is devoted to a concise description of RDBMS and GIS.

2.3.1 Basic definitions of RDBMS

A database is a large collection of interrelated data stored within a computer environment. In such environment, the data is persistent, which means that it survives unexpected software or hardware problems (except severe cases of disk crashes). Traditional applications of databases include management of personnel, stocks, travel reservations, and banking. Many new applications have emerged in the past decades, among them spatial databases in GIS application, images, computer-aided design and manufacturing (CAD/CAM), and software engineering.

A database management system (DBMS) is a collection of software that manages the database structure and controls access to data stored in a database. Generally speaking, a DBMS facilitates the process of defining, constructing, manipulating, querying and updating the database. A DBMS acts as a mediator between users or application programs and the devices where data resides. It can clearly show that users interact with a representation of data independently of the actual physical storage, and the DBMS is in charge of translating the user's manipulations into efficient operations on physical data structures.

Relational database management systems (RDBMS) store and handle information using the relational database management model. RDBMS have a solid mathematical foundation (e.g., Codd 1970). The term *relational* stems from the fact that each record in the database contains information related to a single subject and only that subject. A RDBMS manages data in tables. By definition, a *table* is an object that is defined and used to store data. Each table contains information about a particular subject. Tables contain fields (or columns) that store different kinds of data. In the table, a *primary key* is used to define one or more fields that have a unique value for each record. *Primary key* can be used to link other table that contains relative information. Tables can also be linked using a *secondary key* (foreign key). A RDBMS has three main types of capabilities: data definition, data manipulation, and data control. Rules can be defined to ensure RDBMS data integrity.

RDBMS provide many ways to work with data, especially using the powerful database language SQL (Structured Query Language). SQL is the common language of client/server database management (Jennings 1997). The principal advantage of SQL is standardization, that is, everybody uses a common set of SQL statements with all SQL-compliant database management systems. SQL has three different methods of implementation:

- Direct invocation sends a series of SQL statements to the RDBMS; the RDBMS responds to the query by creating a table that contains the result and displays the table.
- Module Language lets you write a text file of SQL statements that later are executed by an application.
- Embedded SQL is the most common implementation; the SQL statements are generated by the application or included as strings of text in a command of an application language.

By querying the table, particular data information can be extracted. RDBMS permits to share the data with other users, or distribute all the data with other databases (e.g., dBASE and FoxPro).

2.3.2 Geographic Information Systems (GIS)

Geographic Information Systems (GIS) are widely used in diverse applications by business, government, and academia. GIS is an information system that is designed to work with data referenced by geographic coordinates, and to handle information keyed with locations (Star and Estes 1990). The key features that differentiate GIS from other information systems are modules that focus on spatial entities and relationships with specific attention to spatial analyses and modeling operations (Maguire 1991). The basic processing steps of GIS are:

- data input
- data management (update, storage and retrieval)
- analysis
- output.

Spatial data stores the geometric location of geographic features, along with attribute information describing what these features represent. In GIS, usually the location data is stored in a vector or raster data structure, and corresponding attribute data is stored in a set of tables related geographically to the features they describe. This is also known as a georelational data structure. All these spatial data is organized thematically into different layers, or themes. There is one theme for each set of geographic features or phenomena for which information will be recorded. For example, streams, land use, elevation, and buildings will each be stored as a separate spatial data sources, rather than trying to store them all together in one. This makes it easier to manage and manipulate the data, especially as much of the power of working geographically comes from being able to analyze the spatial relationships between different geographic themes.

Rapidly development of digital computer systems has made GIS affordable to an increasingly wider audience. Using GIS, we can ensure the continuing usefulness of data throughout the investigations and analyses, platforms for the storage, update, and management of data. Some GIS programs (e.g., ArcView and ArcInfo) can read the data of relational database provided that those refer to data with coordinates, and follow the Open DataBase Connectivity standard (ODBC). As shown in Fig. 2, data in the database can be read and queried directly by Arcview/ArcInfo using ODBC. The queries are formulated by using SQL, which is commonly used as a standard database query language.

Figure 2-2. Data exchange between GIS and ACCESS database through ODBC drivers.

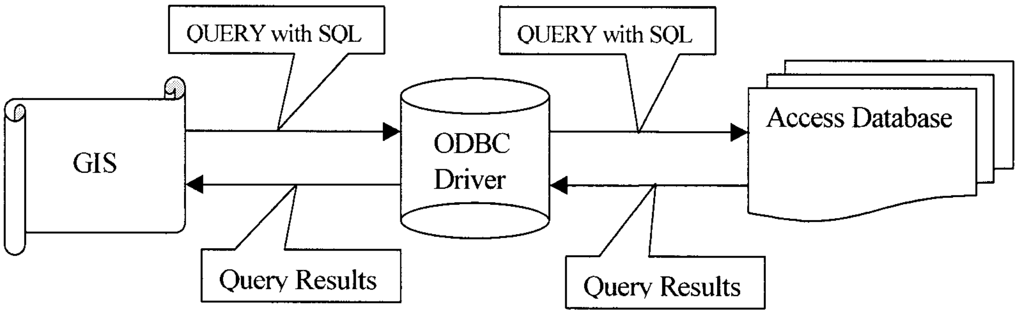

GIS application in geotechnical engineering field is boosted by the advanced information technologies. Frost and Chameau (1993) summarize the views on issues critical to the application of GIS in geotechnical earthquake engineering. Several databases have been developed to storage and manipulate geology and geotechnical data sets. GIS can be a useful data storage and display tool for ground motion amplification analysis (Borcherdt, R.D 1997). Currently it has been applied to lifeline earthquake engineering to deal with pipeline damage and electrical distribution system (O' Rourke, T.D. 1998). Liquefaction hazard mapping can also be done on the local or regional spatial analysis. GIS-based procedure has been developed by Frost et al. (1997) to review liquefaction potential.

GIS also has potential to predict the landslide hazard and slope stability. Carrara, A. et al. (1999) uses GIS technology to predict and monitor the landslide hazards. Miles and Ho (1999) apply the Newmark's method to landslide hazard zonation using GIS. Earthquake-induced lateral-spread ground failure has been predicted base on the data in geographic information system (Taguchi and Hamada 1994).

2.4 LIDD and BOD database structure, definition and content

Two separate databases were developed using the relational data model from Access:

- LIDD: Liquefaction-Induced ground Deformation Database
- BOD: BOrehole Database.

The database on soil boreholes BOD stands on its own. It can be applied to many other geotechnical engineering projects. The separation in two databases does not affect the usability of these databases in the analysis of liquefaction-induced ground deformation. This section will describe the detail of data structure and definition in LIDD and BOD.

2.4.1 LIDD structure and Tables definitions

As shown in Table 2, LIDD contains six tables. *TblCoordSys* defines the coordinate of a location relative to a specified coordinate system. *TblEarthquake* provides the main earthquake characteristics. *TblSite* defines the physical parameters common to a site, e.g., the peak ground acceleration. *TblVector* defines the vectors of permanent ground displacement. *TblReference* describes the references used in the study. *TblReflist* is used for multiple references on identical subjects. Both *TblCoordSys*, *TblReference* and *TblReflist* have multi-purpose applications in other engineering databases, and also have been used in BOD.

Table 2-2. Tables defined in LIDD.

Table Name	Description
TblCoordSys	Different coordinate systems used in database
TblEarthquake	General information on earthquakes
TblSite	Common parameter related on the site
TblVector	Permanent ground displacements
TblReference	Reference on data resource
TblReflist	Multiple list of reference

As shown in Fig. 3, relationships between tables have been constructed by using two basic types of relationships: *one-to-many* and *one-to-one*. *TblCoordsys* is an important table that is used for all the spatial coordinates, including those of displacement vectors (*TblVector*), and site specific data (*TblSite*). *TblEarthquake* and *TblSite* are linked through *EqID*, which gives the earthquake parameters within an area. All one-to-many relationships have referential integrity, which means that if one record in “one” side table is updated, the “many” side tables are updated accordingly. It makes easier to check data and maintain data integrity. Earthquake related displacement vector can be related to the site using *SiteID*.

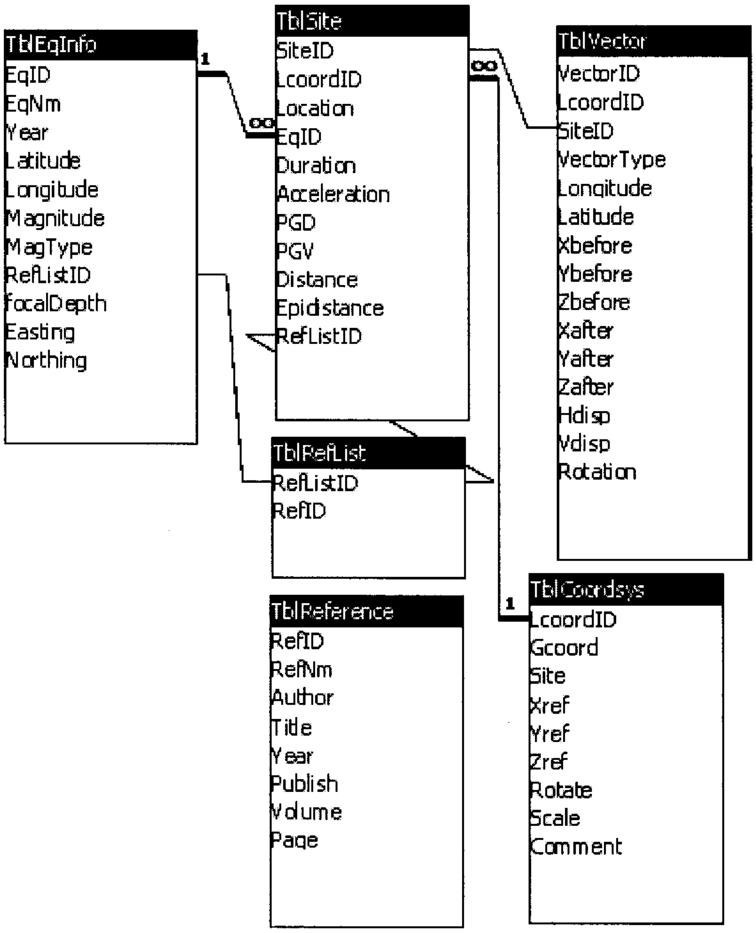

Figure 2-3. Relationships between tables in LIDD.

As shown in Table 3, *TblCoordsys* is a table used in BOD and LIDD for defining the global coordinates of observations, based on local coordinates. *LcoordID* is the primary key, which identifies the user-defined local (UDL) coordinate system. UDL coordinates are usually defined by the user before digitizing drawings. *Gcoord* gives the name of the global cartesian coordinate system which is related to the selected UDL coordinate system. The global coordinate systems (e.g., UTM and Japan cartesian coordinate system) are particular cases of UDL coordinate systems. *Xref,* *Yref, Zref* are the global coordinates of a reference point that has zero UDL coordinate values. *Rotation* is the rotation angle between the axis of global and UDL coordinates systems. *Scale* is the scaling factor from global to UDL coordinates. The values of *Xref, Yref, Zref, Rotation* and *Scale* define the transformation from UDL coordinates to global coordinates. *Comment* is a commentary that describes the selection of the reference point and some additional information useful to convert UDL to global coordinates.

Table 2-3. Dictionary of Table *TblCoordsys*.

Field Name	Data Type	Description
LcoordID	Integer	ID of local coordinate system
Gcoord	Text	Name of global coordinate system
Xref	Double	X coordinate of reference point of UDL coordinate system
Yref	Double	Y coordinate of reference point of UDL coordinate system
Zref	Double	Z coordinate of reference point of UDL coordinate system
Rotation	Double	Rotation angle of UDL coordinate system (degree)
Scale	Double	Scale of UDL coordinate system
Comment	Text	Description of reference point and coordinate transformation

All the tables that contain coordinate values are systematically linked to *TblCoordsys*. The global coordinates X, Y and Z, which are required by GIS, are calculated from the UDL coordinates x, y and z by applying the following transformation:

$$\begin{pmatrix} X \\ Y \end{pmatrix} = \begin{pmatrix} X_{ref} \\ Y_{ref} \end{pmatrix} + f \begin{bmatrix} \cos\theta & \sin\theta \\ -\sin\theta & \cos\theta \end{bmatrix} \begin{pmatrix} x \\ y \end{pmatrix} \quad \text{and} \quad Z = z - Z_{ref} \qquad (2\text{-}1)$$

where Scale $= f$ is the scale ratio between local and global coordinates, Rotation = θ is the rotation angle of axis-coordinates (generally set to zero), and X_{ref}, Y_{ref}, Z_{ref} are the global coordinates of the reference point. Figure 4 gives examples of values for Table *TblCoordsys*.

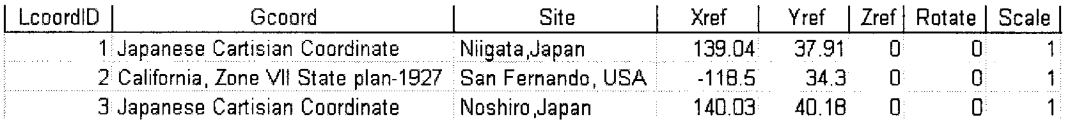

LcoordID	Gcoord	Site	Xref	Yref	Zref	Rotate	Scale
1	Japanese Cartisian Coordinate	Niigata,Japan	139.04	37.91	0	0	1
2	California, Zone VII State plan-1927	San Fernando, USA	-118.5	34.3	0	0	1
3	Japanese Cartisian Coordinate	Noshiro,Japan	140.03	40.18	0	0	1

Figure 2-4. Example of values for Table *TblCoordsys.*

As shown in Table 4, *TblEarthquake* contains the main earthquake characteristics. The primary key *EqID* links this table to Table *TblSite*. *EqNm* and *Year* describes the name and occurrence date of the earthquake, respectively. *Latitude* and *Longitude* supply the epicenter location. *Magnitude* gives the earthquake magnitude, and *MagType* is the corresponding type of magnitude (e.g., moment magnitude). *RefListID* links to Table *TblRefList*, which identifies a list of references about the earthquake.

Several types of magnitude can be used to measure the earthquake size: local magnitude (M_L), surface wave magnitude (M_S), body wave magnitude (M_b), duration magnitude (M_D), coda magnitude (M_c), and moment magnitude (M_w). M_w is commonly used because it is a better estimate of the amount of seismic energy released by a given earthquake than other measures of earthquake magnitude, especially for $M > 8$ events. Other earthquake magnitude measures become less sensitive to the size of the earthquake for strong earthquake, the body wave and local magnitudes saturate at magnitudes of 6 to 7 and the surface wave magnitude saturates at about $M_s = 8$. In LIDD, most of the magnitudes are moment magnitude. *MagType* has been used to identify different magnitude types. Figure 5 gives some example of values stored in Table *TblEarthquake*.

Table 2-4. Dictionary of Table *TblEarthquake*.

Field Name	Data Type	Description
EqID	Integer	ID of earthquake
EqNm	Text	Earthquake name
Year	Date	Date of occurrence
Latitude	Text	Latitude of epicenter
Longitude	Text	Longitude of epicenter
Magnitude	Double	Earthquake magnitude
MagType	Text	Type of magnitude
RefListID	Integer	ID of reference document

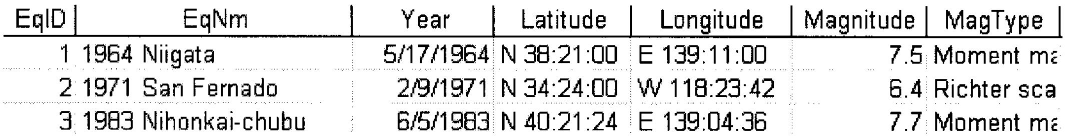

EqID	EqNm	Year	Latitude	Longitude	Magnitude	MagType
1	1964 Niigata	5/17/1964	N 38:21:00	E 139:11:00	7.5	Moment ma
2	1971 San Fernado	2/9/1971	N 34:24:00	W 118:23:42	6.4	Richter sca
3	1983 Nihonkai-chubu	6/5/1983	N 40:21:24	E 139:04:36	7.7	Moment ma

Figure 2-5. Example of values in Table *TblEarthquake*.

The structure of *TblVector*, which collects the liquefaction-induced ground displacement vectors, has been listed in Table 5. *LcoordID* is the primary key to identify each vector. *Xbefore, Ybefore*, and *Zbefore* are the coordinates before the earthquake. *Xafter, Yafter,* and *Zafter* are the coordinates after the earthquake. The coordinates can be changed to global coordinate by using a transformation matrix associated with *LcoordID.* When the Z-coordinate is not specified, *Settlement* is used to record the vertical displacement. The vector length can be easily calculated from the data before and after the earthquake. Figure 6 gives an example of vectors stored in Table *TblVector*.

The displacement data is recorded in two different ways. When the displacement is measured on the ground, the data includes the horizontal displacement and vertical displacment. When the displacement is measured above the ground, such as on the top of buildings, only the horizontal displacement is recorded. The displacement vector is defined by two points, one before earthquake and the other after the earthquake.

Table 2-5. Dictionary of Table *TblVector*.

Field Name	Data Type	Description
VectorID	Integer	ID of vector
LcoordID	Integer	ID of local coordinate system
Xbefore	Double	X-coordinate before the occurrence of earthquake
Ybefore	Double	Y-coordinate before the occurrence of earthquake
Zbefore	Double	Z-coordinate before the occurrence of earthquake
Xafter	Double	X-coordinate after the occurrence of earthquake
Yafter	Double	Y-coordinate after the occurrence of earthquake
Zafter	Double	Z-coordinate after the occurrence of earthquake
Settlement	Double	Vertical displacement

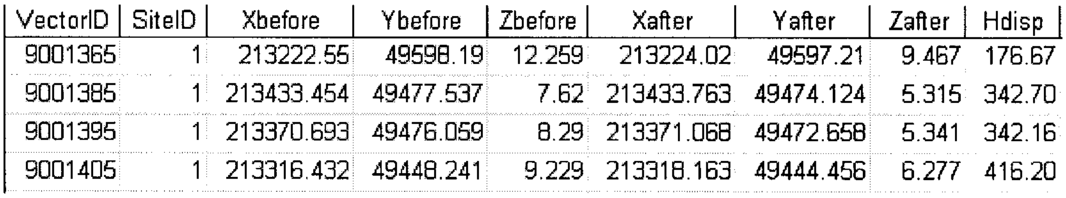

VectorID	SiteID	Xbefore	Ybefore	Zbefore	Xafter	Yafter	Zafter	Hdisp
9001365	1	213222.55	49598.19	12.259	213224.02	49597.21	9.467	176.67
9001385	1	213433.454	49477.537	7.62	213433.763	49474.124	5.315	342.70
9001395	1	213370.693	49476.059	8.29	213371.068	49472.658	5.341	342.16
9001405	1	213316.432	49448.241	9.229	213318.163	49444.456	6.277	416.20

Figure 2-6. Example of vectors data in Table *TblVector*.

As shown in Table 6, Table *TblReference* is a generic table useful for recording bibliographic references, including journal papers, maps, books and technical reports. *RefID* is the primary key. *RefNm* is the reference names. *Title, Author* and *Year* supply the title of the reference, author and year of publication. There may be more than one author. *Document* gives the reference source (e.g., name of journal and institution). Figure 7 gives some example of reference data stored in Table *TblReference*.

Table 2-6. Dictionary of Table *TblReference*.

Field Name	Data Type	Description
RefID	Integer	ID of reference document
RefNm	Text	Name of reference
Title	Text	Title of reference
Author	Text	Author of reference
Year	Date	Published year of reference
Document	Text	Resource of reference

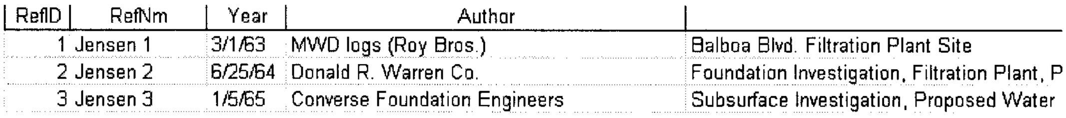

RefID	RefNm	Year	Author	
1	Jensen 1	3/1/63	MWD logs (Roy Bros.)	Balboa Blvd. Filtration Plant Site
2	Jensen 2	6/25/64	Donald R. Warren Co.	Foundation Investigation, Filtration Plant, P
3	Jensen 3	1/5/65	Converse Foundation Engineers	Subsurface Investigation, Proposed Water

Figure 2-7. Example of reference data in Table *TblReference*.

Records that have multiple references cannot be described only with Table *TblReference*. Instead, those records are described using Table *TblRefList,* which defines a list of references. In *TblRefList,* only two fields are defined. As shown in Table 7, *RefListID* is the ID link to another table, *RefID* is the ID link to *TblReference*. As shown in Fig. 8, one earthquake (*EqID* =1) has *RefListID* = 1, it includes three different references (i.e., *RefID* = 1, 2, 3). By using two one to many relationships, one between *TblEarthquake* and *TblRefList* and the other between *TblReference* and *TblRefList*, it is possible to have multiple references.

Table 2-7. Dictionary of Table *TblRefList*.

Field Name	Data Type	Description
RefListID	Integer	ID of reference list
RefID	Integer	ID of reference

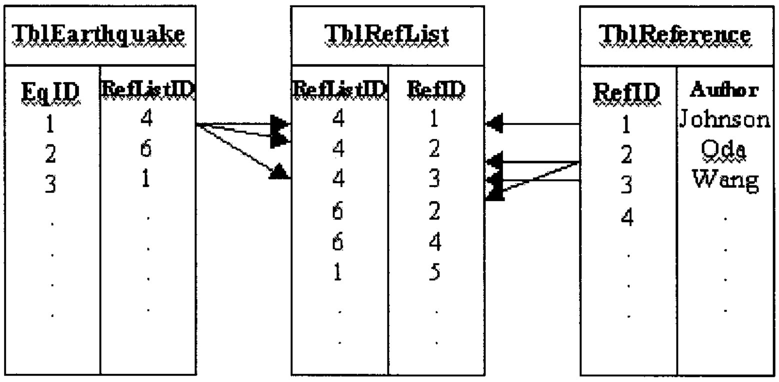

TblEarthquake	
EqID	RefListID
1	4
2	6
3	1
.	.
.	.
.	.
.	.

TblRefList	
RefListID	RefID
4	1
4	2
4	3
6	2
6	4
1	5
.	.
.	.

TblReference	
RefID	Author
1	Johnson
2	Oda
3	Wang
4	.
.	.
.	.
.	.

Figure 2-8. Role of Table *TblRefList.*

2.4.2 BOD structure and Tables definitions

In general, boreholes may be defined as any vertical, inclined or horizontal holes drilled in the ground for the primary purpose of obtaining samples of the overburden or rock material present and thereby permitting the determination of the stratigraphy and/or engineering properties of those materials (Fang, 1991). In this study, the boreholes that characterize soil deposits at specific sites of liquefaction-induced ground deformation have been organized into a database called BOD, which stands for BOrehole Database. The databases BOD and LIDD were intentionally kept separate because BOD may have many other applications in geotechnical engineering. BOD was developed using ACCESS for the same reasons as LIDD.

As shown in Table 8, BOD is made of nine tables. The structure and definition of *TblCoordsys* and *TblReference* are the same as those of LIDD. The other tables are defined in the following sections.

Table 2-8. Tables used in BOD.

Table Name	Description
TblCoordSys	Coordinate systems and UDL conversion
TblReference	Reference on data origins
TblRefList	Multiple reference list
TblSPT_Info	General information on SPT test
TblSPT_Sample	Sample taken from SPT log
TblSPT_Soil	Soil profile of each SPT test
TblSPT_Blow	Blow count of each SPT test
TblCPT_Info	General information on CPT test
TblCPT	Various measured values of CPT variables

Figure 9 shows the relationships between the tables of BOD. Table *TblCoordsys* is an table that linked all the tables together, and also connects BOD and LIDD. Based on the one to many relationships, all the CPT and SPT profiles information can be extracted from Tables *TblCPT* and *TblSPT_Blow* using SQL query. Tables TblReference and TblReflist are the same tables that have been used in LIDD. Ay new type of field investigation data can be populated to BOD by adding new tables defined similarly as SPT or CPT data model.

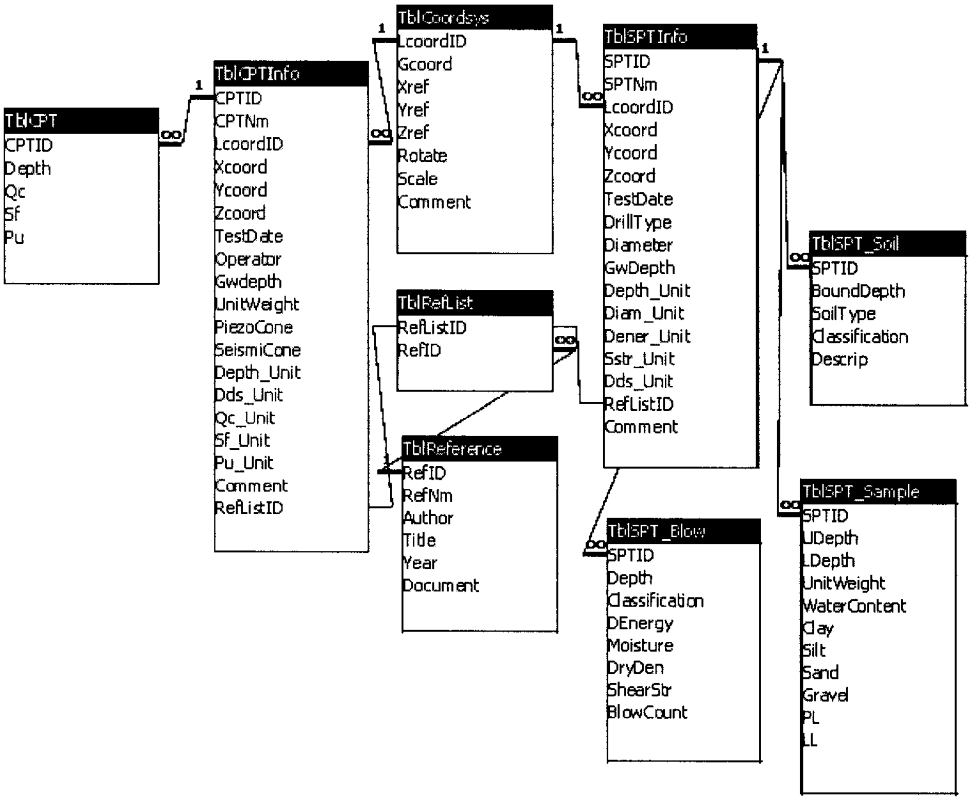

Figure 2-9. Relationships between tables of BOD.

As shown in Table 9, Table *TblSPTInfo* contains general SPT information. It is linked to other databases through the key *LCoodID* that identifies an UDL coordinate system. Each borehole is identified by *SPTID* which uniquely locates SPT data. *XCoord*, *YCoord* and *ZCoord* are the x, y, and z coordinates, respectively, of the UDL coordinate system defined by *LCoodID*. *SPTNm* and *TestDate* are the original SPT name and test date, respectively. *DrillType* supplies the type of drilling used by this SPT test. *Diameter, Hammer* and *GwDepth* are the sampler diameter, hammer energy ratio and depth of ground water table, respectively. In *TblSPTInfo* all the units of physical variables used in reporting SPT data have been defined. *Depth_Unit* gives the SPT depth unit, usually in meter or feet. *Diam_Unit* specifies the SPT hammer diameter unit. *Dener_Unit* supplies the drive energy unit. *Dds_Unit* and *SStr_unit* give the dry density unit and shear strength unit, respectively. *RefListID* gives the reference list for each SPT test. *Comment* supplies some description about the SPT data. Figure 10 gives some examples of SPT data stored in Table *TblSPTInfo*.

Table 2-9. Dictionary of Table *TblSPTInfo*.

Field Name	Data Type	Description
SPTID	Integer	ID of SPT test
SPTNm	Text	Original SPT name given by operator
LcoodID	Integer	ID of UDL coordinate system
Xcoord	Double	x-coordinate in UDL coordinate system
Ycoord	Double	y-coordinate in UDL coordinate system
Zcoord	Double	z-coordinate in UDL coordinate system
TestDate	Date	Test date (dd/mm/yy)
DrillType	Text	Drilling type
Diameter	Double	Diameter of sampler
Hammer	Double	Hammer energy ratio
GwDepth	Double	Depth of ground water table
Depth_Unit	Text	SPT depth unit (m, ft)
Diam_Unit	Text	SPT hammer diameter unit (inch, mm, cm)
Dener_Unit	Text	Drive energy unit
SStr_Unit	Text	Shear stress unit
Dds_Unit	Text	Dry density unit
RefListID	Text	Reference list ID
Comment	Text	Comment about SPT data

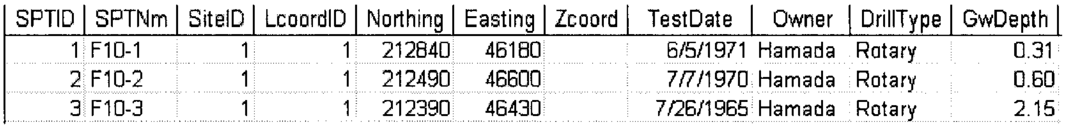

SPTID	SPTNm	SiteID	LcoordID	Northing	Easting	Zcoord	TestDate	Owner	DrillType	GwDepth
1	F10-1	1	1	212840	46180		6/5/1971	Hamada	Rotary	0.31
2	F10-2	1	1	212490	46600		7/7/1970	Hamada	Rotary	0.60
3	F10-3	1	1	212390	46430		7/26/1965	Hamada	Rotary	2.15

Figure 2-10. Example of SPT data in Table TblSPTInfo.

As shown in Table 10, Table *TblSPT_Soil* includes the soil description obtained from SPT sampling. Each data is identified with *SPTID. BoundDepth* is the depth of the soil strata boundary. *Soil_Type* is a soil description observed from SPT sampling (e.g., gravelly sand). Soil type are entered as a number sequence as defined in Table 11. Additional marks "/, +, -, *" are used to express the combination of different soil types. These number sequences are automatically changed into a text that defined soil types. For example, the entry "2/3+4" is converted into "Silty sand and clay". Figure 11 lists some examples of data stored in Table *TblSPT_Soil.*

Table 2-10. Dictionary of Table *TblSPT_Soil.*

Field Name	Data Type	Description
SPTID	Integer	ID of SPT test
BoundDepth	Double	Location of the boundary of soil strata (m)
Soil_Type	Text	Soil description directly observed from SPT sampler

Table 2-11. Soil type name system introduced in the present study.

ID	Soil Type	ID	Soil Type	ID	Soil Type
1	Fill	11	Cobbles	2.4	Coarse
2	Sand	12	Gravel	2.5	Very
3	Silt	20	Sandstone	2.6	Well
4	Clay	21	Siltstone	2.7	Uniform
5	Sand & Gravel	22	Claystone	/	With
6	Humus	23	Conglomerate	+	And
7	Shell	24		-	To
8	Polluted Sludge	2.1	Very fine	*	Layered
9	End	2.2	Fine		
10	Loam	2.3	Medium		

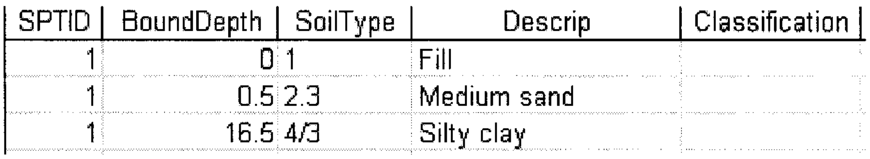

SPTID	BoundDepth	SoilType	Descrip	Classification
1	0	1	Fill	
1	0.5	2.3	Medium sand	
1	16.5	4/3	Silty clay	

Figure 2-11. Example of soil data in Table *TblSPT_Soil*.

As shown in Table 12, Table *TblSPT_Sample* includes the information that was obtained from laboratory tests performed on soil samples. At some depth, soil samples are taken and subjected to classification tests in the laboratory. Each data is identified with *SPTID*. *UDepth* and *LDepth* are the depths of upper and lower boundary of the soil sample. *UnitWeight* and *WaterContent* are the unit weight of soil sample and water content, respectively. *Clay, Silt, Sand* and *Gravel* are the fraction of each content of the soil sample in %. *PL* and *LL* are the plastic limit and the liquid limit, respectively. *RefListID* defines the references. Figure 12 gives some examples of sample data stored in Table *TblSPT_Sample*.

Table 2-12. Dictionary of Table *TblSPT_Sample*.

Field Name	Data Type	Description
SPTID	Integer	ID of SPT test
Udepth	Double	Depth of upper bound of a lump which soil sample was taken(m)
Ldepth	Double	Depth of lower bound of a lump which soil sample was taken(m)
UnitWeight	Double	Unit weight of soil sample (kN/m^3)
WaterCont	Double	Water content of soil sample (%)
Clay	Double	Clay fraction of soil sample (%)
Silt	Double	Silt fraction of soil sample (%)
Sand	Double	Sand fraction of soil sample (%)
Gravel	Double	Gravel fraction of soil sample (%)
PL	Double	Plastic limit of soil sample
LL	Double	Liquid limit of soil sample

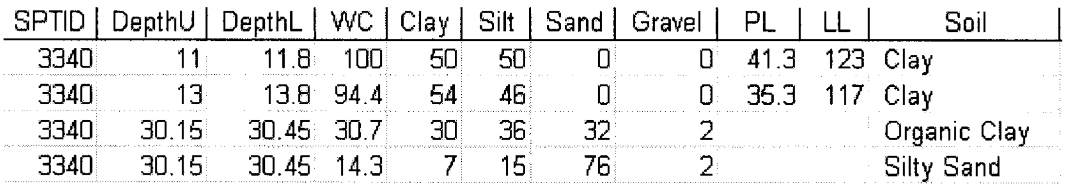

SPTID	DepthU	DepthL	WC	Clay	Silt	Sand	Gravel	PL	LL	Soil
3340	11	11.8	100	50	50	0	0	41.3	123	Clay
3340	13	13.8	94.4	54	46	0	0	35.3	117	Clay
3340	30.15	30.45	30.7	30	36	32	2			Organic Clay
3340	30.15	30.45	14.3	7	15	76	2			Silty Sand

Figure 2-12. Example of SPT sample data in *TblSPT_Sample.*

As shown in Tabel 13, Table *TblSPT_Blow* contains the SPT blow counts. Each data is identified with *SPTID. Depth* is the depth in m or ft where the blow count was obtained. *BlowCount* is the SPT standard N value. *DEnergy*, *Moisture, DryDen* and *ShearStr* record driving energy, moisture, dry density and shear stress at different depth. Figure 13 gives some examples of SPT blow count data stored in Table *TblSPT_Blow.*

Table 2-13. Dictionary of Table *TblSPT_Blow.*

Field Name	Data Type	Description
SPTID	Integer	ID of SPT test
Depth	Single	Depth where blow count was obtained (m)
Denergy	Single	Drive energy of SPT test
Moisture	Single	Moisture content
DryDen	Single	Dry density
ShearStr	Single	Shear strength
BlowCount	Integer	SPT blow count

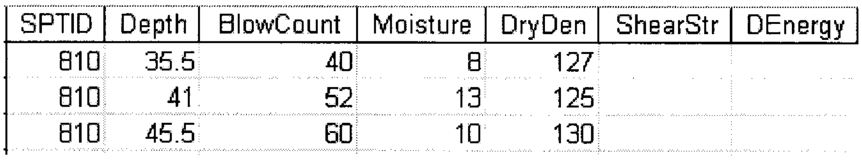

SPTID	Depth	BlowCount	Moisture	DryDen	ShearStr	DEnergy
810	35.5	40	8	127		
810	41	52	13	125		
810	45.5	60	10	130		

Figure 2-13. Example of SPT blow count data in Table *TblSPT_Blow.*

As shown in Table 14, Table *TblCPTInfo* contains general CPT information. Table *TblCPTInfo* can be linked to other databases through *LCoodID* which identifies local coordinate system. Each borehole is identified by *CPTID*, which locates uniquely the CPT data in the database. *XCoord, YCoord* and *ZCoord* are x, y, and z coordinates, respectively, in the local coordinate system defined by *LCoodID*. *CPTNm, TestDate* are original CPT name and test date, respectively. *PiezoCone* and *SeismiCone* identify the penetration cone type used in the test. *Depth_Unit* gives the CPT depth unit, usually in meter or feet. *Dds_Unit* supplies unit of dry unit weight. *Qc_Unit, Sf_Unit* and *Pu_Unit* represent the unit of tip resistance, unit of sleeve friction and unit of pore water pressure, respectively. *RefListID* describes the references. Figure 14 gives some examples of CPT data stored in Table *TblCPTInfo*.

Table 2-14. Dictionary of Table *TblCPTInfo*.

Field Name	Data Type	Description
LcoodID	Integer	ID of local coordinate system
CPTID	Integer	ID of CPT test
XCoord	Double	X-coordinate in the local coordinate system
YCoord	Double	Y-coordinate in the local coordinate system
ZCoord	Double	Z-coordinate in the local coordinate system
CPTNm	Text	Original CPT name given by operator
TestDate	Date	Test date (dd/mm/yy)
Gwdepth	Single	Ground water depth
PiezoCone	Yes/No	Piezo cone test
SeismiCone	Yes/No	Seismic cone test
Depth_Unit	Text	CPT depth unit (m, ft)
Dds_Unit	Text	Unit of dry density
Qc_Unit	Text	Unit of tip resistance
Sf_Unit	Text	Unit of sleeve friction
Pu_Unit	Text	Unit of pore water pressure
Comment	Text	Description of CPT data
RefListID	Integer	ID of reference list

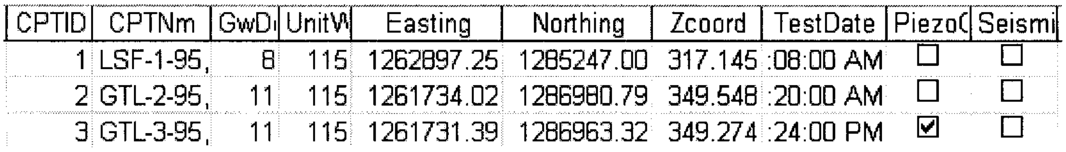

CPTID	CPTNm	GwDi	UnitW	Easting	Northing	Zcoord	TestDate	PiezoC	Seismi
1	LSF-1-95,	8	115	1262897.25	1285247.00	317.145	:08:00 AM	☐	☐
2	GTL-2-95,	11	115	1261734.02	1286980.79	349.548	:20:00 AM	☐	☐
3	GTL-3-95,	11	115	1261731.39	1286963.32	349.274	:24:00 PM	☑	☐

Figure 2-14. Example of CPT data in Table *TblCPTInfo*.

As shown in Table 15, Table *TblCPT* contains CPT profiles. Each data is identified with *CPTID*. *Depth* is the depth where the CPT data was obtained. *Qc, Sf* and *Pu* are the tip resistance, sleeve friction and pore water pressure, respectively.

Table 2-15. Dictionary of Table *TblCPT*.

Field Name	Data Type	Description
CPTID	Integer	ID of CPT test
Depth	Double	Depth where CPT data obtained
Qc	Double	Tip resistance
Sf	Double	Sleeve friction
Pu	Double	Pore water pressure

2.4.3 Contents of LIDD and BOD

Table 16 summarizes the actual contents of the LIDD database in terms of numbers of displacement vectors. There are 16,221 vectors originating from eight earthquakes and six regions in California and Japan.

Table 2-16. Earthquakes and displacement vectors in LIDD.

Earthquake	Year	Area Name	LIDD	Bartlett (1998)
Niigata	1964	Niigata, Japan	2498	299
San Fernando	1971	Jensen Filtration Plant	864	28
Imperial Valley	1979	Imperial Valley	32	32
Nihonkai-Chubu,Japan	1983	Noshiro,Japan	2954	72
Superstition Hill	1987	Imperial Valley	4	6
Loma Prieta	1989	San Francisco, USA	-	-
Northridge	1994	Van Norman Complex	1011	-
Hyogoken Nanbu Earthquake	1995	Kobe, Japan	8894	-

The displacement data ran`ge has been listed in Table 17 per earthquake. Most displacements are between 1 and 200 cm. In some case, such as Niigata, Japan 1964 earthquake, the maximum horizontal displacement is as large as 11 m.

Table 2-17. Number of displacement vectors and amplitude range of horizontal and vertical displacement data in LIDD.

Earthquake Name	Number of vectors	Horizontal displacement (cm)	Vertical displacement (cm)
Niigata,1964	2498	2.2 - 1131	-378 - 262
San Fernando, 1971	836	2 - 385	-267 - 187
Nihonkai-chubu, 1983	2954	1 - 565	-138 - 110
Northridge, 1994	1011	1 - 120	-101 - 167
Hyogoken Nanbu, 1995	8897	0.3 - 671	-590 - 745

All the displacement vector data, except those of the 1987 Superstition earthquake, were generated by the method of aero-triangulation (e.g., Sano 1998). Systematic errors and random errors are introduced when the method of aero-triangulation is used to generate ground displacement data (Sano 1998). Correction should be made according to ground control points. Table 18 lists the accuracy of absolute ground displacements for the 1994 Northridge and 1995 Hyogoken-Nanbu earthquakes. The accuracy of liquefaction-induced ground displacement is given as a root-mean square of two accuracy before and after the earthquake, as shown in Table 18, are estimated as ± 33 cm and ± 39.2 cm in the horizontal and vertical directions, respectively, for the 1994 Northridge earthquake cases, and ± 33 cm and ± 53 cm in the horizontal and vertical directions, respectively, for the 1995 Hyogoken-Nanbu earthquake cases.

For the data collected from Japan, the VectorID has the format which can be used to identify the measured displacement type. The last digit of the unique id denotes the location of points as specified in Table 19, such as on the ground or on top of roofs.

Table 2-18. Accuracy of measurement of ground displacement (after Sano 1998, and Hamada, et al. 1996b).

Region	Accuracy of absolute ground displacement (m)		Accuracy of relative ground displacement (m)	
	Horizontal	Vertical	Horizontal	Vertical
Northridge, 1994	±0.330	±0.392	±0.197	±0.326
Hyogoken-Nanbu, 1995	±0.330	±0.530	±0.140	

Table 2-19. Definition of vector data type in Japan case histories of liquefaction-induced ground deformation.

ID	Specification
9*****1	Manhole, signal on road, etc.
9*****2	Foot of pole type (electric pole, etc.)
9*****3	Foot of fence or guard rail
9*****4	Other point on ground
9*****5	Non-ground (bridge, house, etc.)

Table 20 summarizes the seismic parameters of the eight earthquakes in the database. It includes the magnitude (moment magnitude), peak ground acceleration (PGA), duration and epicenter distance (distance between the earthquake epicenter and area in which ground displacements are measured). These parameters characterize the earthquake properties.

Table 2-20. Seismic parameters of earthquakes in LIDD.

Earthquake Name	Magnitude	PGA (g)	Duration (sec)	Epicenter Distance (km)
Niigata,1964	7.5	0.19	20	21
San Fernando, 1971	6.4	0.55	12	0.2-0.5
Imperial Valley, 1979	6.6	0.21	6	0
Nihonkai-chubu, 1983	7.7	0.25	12	27
Superstition Hill, 1987	6.6	0.21	21	28
Loma Prieta, 1989	7.0	0.45	-	80
Northridge, 1994	6.7	0.7	20	2.5
Hyogoken Nanbu, 1995	6.9	0.7	-	-

BOD contains a total of 5,133 borehole tests consisting of 4904 SPT and 229 CPT soundings. Table 21 gives the total number of SPT and CPT per region.

Table 2-21. Total number of SPT and CPT soundings per region in BOD.

Location	SPT	CPT
Niigata, Japan	645	-
Noshiro, Nihonkai-chubu, Japan	71	-
Kobe, Hyogoken Nanbu, Japan	4002	-
Van Norman Complex, USA	257	230
Loma Prieta, USA	-	9

GIS platform has been extensively used to collect and store other non-tabulated data for liquefaction-induced ground deformation including topographical maps, street maps, aerial photographs, and digital elevation models (DEM) of pre- and post-earthquake conditions. All these type of data are useful to overlay maps in the background and data in the foreground.

Street maps were collected from various sources, and stored as raster images keyed with coordinates. As shown in Table 22, a large number of aerial photographs were collected in the present study. Aerial stereo photographs are used not only to produce topographic maps and GIS background, but also for aero-triangulation. Aerial photographs were stored as raster images and keyed with coordinates like base maps. The individual aerial photographs, which were obtained from several sources, were scanned and assembled into large images, after applying some corrective measures. The display of data with precise geographic coordinates over raster images (e.g., aerial photographs) require base maps to be free of distortions, which may be caused by scanning, optical effects and/or projections. ArcGIS has special features for correcting raster images. These programs require the visual identification of a few control points on the raster images which have precisely known geographic coordinates. These programs correct the images so that all the control points assume their specified coordinates.

Table 2-22. Summary of aerial photographs collected in the present study.

Earthquake	Number of Photo	Scale	Photo Date	Reference
1964 Niigata	18	1:8000-11000	June, 1964	Hasshu, Co. Ltd., 1999c
1971 San Fernando	0	-	-	-
1979 Imperial Valley	1	-	-	Hamada et al. 1992
1983 Nihonkai-chubu	4	1:8000	6/3/83	Hasshu, Co. Ltd., 1999b
1987 Superstition Hills	1	-	-	Hamada et al. 1992
1989 Loma Prieta	1	1:1200	10/26/89	City and County of San Francisco, 1989
1994 Northridge	68	1:6000	2/10/94	I. K. Curtis Services Inc., 1994
1995 Hyogoken N.	56	1:8500	1/18/95	Hasshu, Co. Ltd., 1999a

The surface elevation before the earthquake is an important factor for the analysis of liquefaction-induced permanent ground deformation (Hamada et al. 1986, Bartlett et al. 1992 and 1995, and Bardet et al. 1999a). The data on surface elevation was collected as spot heights, contour on topographic maps, and digital elevation models

(DEM). The elevation data can be digitized from topographical maps using elevation contours and spot heights, and then converted to ASCII format.

The contents of the databases LIDD and BOD can be visualized using ArcGIS (2002) and Surfer (Golden Software 1997). All the spatial data in database are accessed directly from LIDD and BOD by ArcGIS using ODBC. Basemaps and aerial photographs were imported as images and assigned coordinates in ArcGIS by identifying control points. Figure 15 shows one example of the borehole locations in Niigata City and locations of ground displacement vectors after the 1964 Niigata earthquake

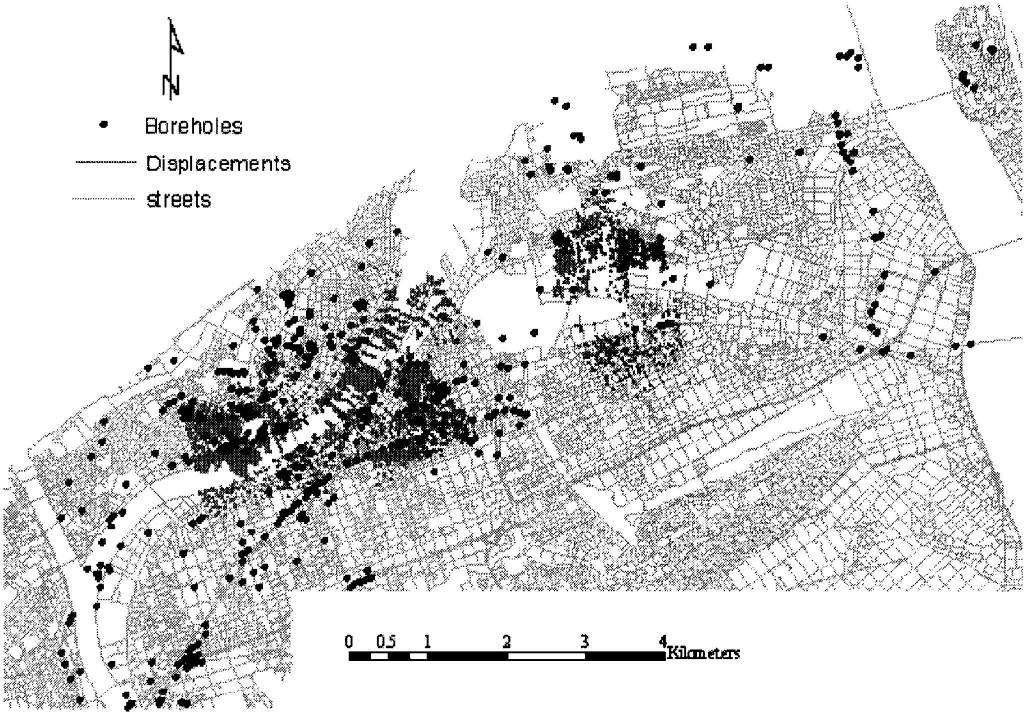

Figure 2-15. Borholes and ground displacement vectors of 1964 Niigata earthquake collected in LIDD and BOD (street map of Niigata city used as basemap).

2.5 Geotechnical data exchange using Web Service

In this section, a information architecture using Web services for exchanging and utilizing geotechnical information in an environment of multiple data sources will be presented using data from LIDD and BOD. The exchange of geotechnical information is via an XML format on a platform that interoperates via Web services. Such architecture is of critical interest to a large number of municipal, state and federal agencies as well as private enterprises involved with civil infrastructures. For example in the case of soil liquefaction hazard assessment, the necessary geotechnical data can be retrieved from the system for evaluating potential earthquake risks and hazard intensity.

2.5.1 XML exchange format for geotechnical information

In view of the diversity of geotechnical boreholes, there is no accepted common format for storing and displaying their data, and sharing them among researchers and practitioners. Investigators usually store the results of geotechnical studies in tabular (text, numbers) or graphic (plot) formats. There are great amount of geotechnical test results still in plain paper format (legacy data). To date, the most commonly used formats for representing geotechnical borehole data include the Association of Geotechnical and Geoenvironmental Specialists (AGS 1999), the Log ASCII Standard (LAS 1999) for well logging in petroleum engineering, and the National Geotechnical Experimental Site (NGES) format that adopt the AGS data dictionary and expand to cover more research based geotechnical test (Benoit 1999). Formats such as AGS, LAS, and NGES are already available and can be adapted for use as a geotechnical data standard. But most of them are the format mixing data content and data dictionary. This type of data-format mixture structure is very difficult to exchange data through Internet or application. For certain complicated data set, such as audio, video from VisCone (Raschke and Hryciw 1997), AGS or LAS has no capability to handle them according to current specification. As a pure ASCII file format, it is impossible to link to external files that may come with borehole test such as laboratory test.

It is proposed to apply XML to store, retrieve and display borehole data in geotechnical engineering. Similar efforts are underway in the oil industry, which is considering XML in addition to LAS. The World Wide Web Consortium (W3C, 2000) developed XML for facilitat.ing the use and distribution of richly structured documents, such as databases. The first official XML specification was published in 1998. The greatest advantage of XML is its ability to define an interchange format for transferring data between databases that work using different software and operating systems.

XML is originated for document and data exchange, and is more flexible for storing data than LAS or AGS, because it is free of restrictive ASCII format with fixed sections and mnemonics. XML can organize and name data in many ways. XML is similar to HTML (Hyper Text Markup Language). However unlike HTML, XML supports a larger set of document elements, and has no limited or fixed sets of tags.

XML uses elements and attributes, which are either free formation or defined using markup rules. This ensemble of rules is called a Document Type Definition (DTD). A DTD can specify rules for how the XML document elements, attributes and other data are defined and logically related in an XML-compliant document (Eckstein 1999). A DTD can be in a separate document (preferably if it is to be used repeatedly) or inserted at the head of XML documents. The DTD defines the overall structure and syntax of XML documents. It specifies everything an XML parser needs to know. An XML document that conformed to DTD is called as validated XML document.

Basically XML organizes the data as a tree structure. The root element is the access point of the XML file. It contains multiple child elements that can have their own attributes and sub child element. All the elements must have a start tag and an end tag, and they must be nested in a certain order. The tree structure of the XML make it very flexible to extend or expand the structure based on the exist data.

Figure 16 presents an example of geotechnical borehole in XML format. One can see that this tree structure is ready to expand to fit the growing data. Unlike LAS or AGS, which stores data in tabular format with delimiting characters, XML stores each part of the data set in fields with separating spaces. As shown in Fig. 16, XML files start with a line called an instruction command, which indicates the version of XML and the type of encoding:

```
<?xml version="1.0" encoding="UTF-8" standalone= "no"?>
```

XML, designed to be an Internet-friendly syntax for information exchange, has internationalization at its very core. The encoding attribute specifies which character encoding the file used. The standalone attribute "no" informs the program that an outside DTD is needed to correctly interpret the document. In this case the DTD will reside in a separate file called `<!DOCTYPE BOREHOLE SYSTEM "Borehole.dtd">`, which identifies which tags you can use to describe data in the XML document. The second line the in the XML file is to call a style sheets file to control how this XML documents are displayed in the browser. '`<BOREHOLE>`' is the root element. The root element will be referred to later in the XSL file that formats XML files. All elements and attributes are in capital letters to prevent any conflicts within the file. The root element has two child elements namely `PROJ, HOLES` that have been defined in DTD file. The child elements `PROJ, HOLES` must appear in this order in the XML documents. The tree structure of XML is more versatile for storing geotechnical data than LAS and RDBMS. Each child element has its own sub elements or attributes. For the fields without any information are displayed as empty elements. For instance, dates are stored as '`<DATE>` *the date in the format we want* `</DATE>`', otherwise their field can be left empty as '`<DATE/>`'. Under the HOLES element, multiple drilling holes can be recorded by the element HOLE. The HOLE_DETAILS element contains all the general information about the SPT borehole test, such a drilling location, date, operator and contractor. The GEOL, INSITU_TEST, and SAMPS have been used to define the soil strategy, multiple insitu-test such as standard penetration test and soil samples activity respectively. The XML structure is very easy to expand. For example, ISPT element has been defined under the INSITU_TEST to record the information of SPT, other type of test such as insitu permeability test also can be added under the INSITU_TEST element as an new sub element. Laboratory test information can be append to SAMP element as a sub element, any new properties associated with the laboratory test for the samples can be defined without ruin the entire structure.

XML data format for geotechnical information separates distinctively raw data from ancillary data used to display format. XML data can be formatted for display using XSL (Extensible Stylesheet Language) and for vector graphical display using SVG Scalable Vector Graphic (SVG 2003). SVG (Scalable Vector Graphic) is a specification developed to display the vector graphic in document or Internet. The curves sections of XML CPT files can be plotted by adding an HTML command to the XSL file, which inserts an SVG file. The SVG file encloses graphic data and commands to display the graphics such as point, line, polyline or rectangle.

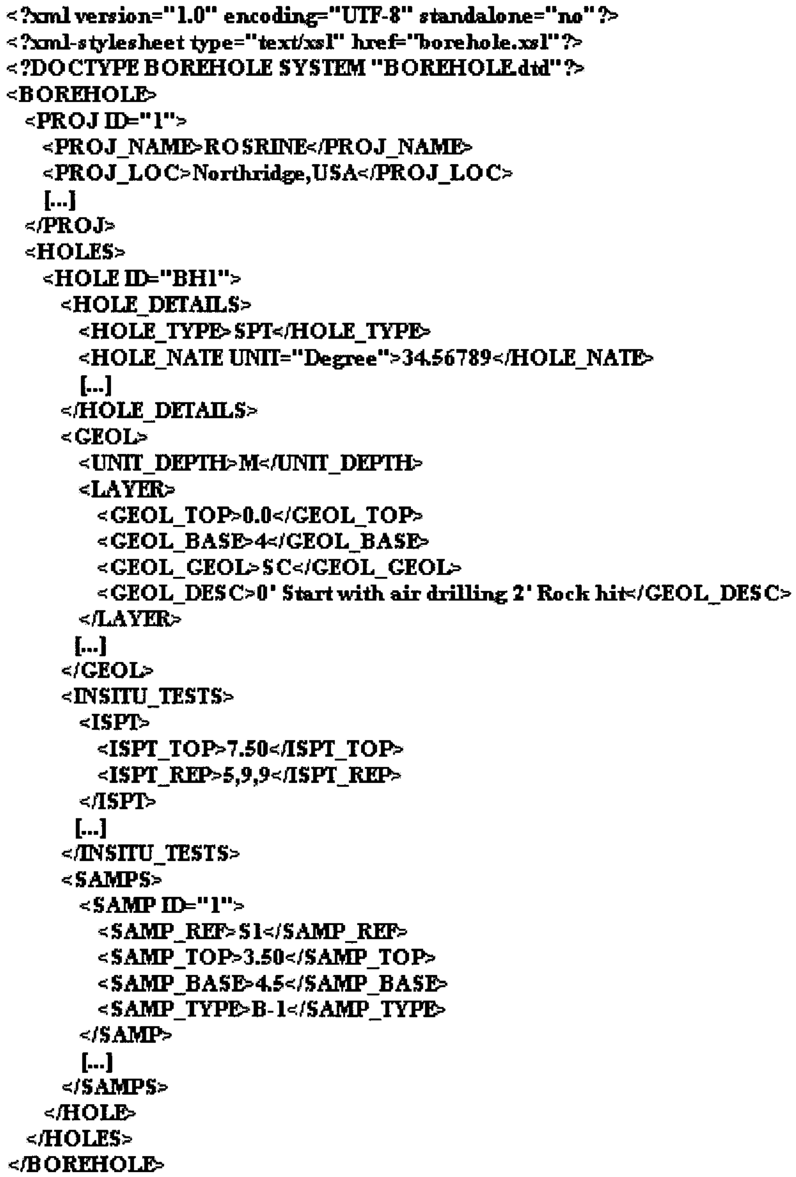

```xml
<?xml version="1.0" encoding="UTF-8" standalone="no"?>
<?xml-stylesheet type="text/xsl" href="borehole.xsl"?>
<?DOCTYPE BOREHOLE SYSTEM "BOREHOLE.dtd"?>
<BOREHOLE>
  <PROJ ID="1">
    <PROJ_NAME>ROSRINE</PROJ_NAME>
    <PROJ_LOC>Northridge,USA</PROJ_LOC>
    [...]
  </PROJ>
  <HOLES>
    <HOLE ID="BH1">
      <HOLE_DETAILS>
        <HOLE_TYPE>SPT</HOLE_TYPE>
        <HOLE_NATE UNIT="Degree">34.56789</HOLE_NATE>
        [...]
      </HOLE_DETAILS>
      <GEOL>
        <UNIT_DEPTH>M</UNIT_DEPTH>
        <LAYER>
          <GEOL_TOP>0.0</GEOL_TOP>
          <GEOL_BASE>4</GEOL_BASE>
          <GEOL_GEOL>SC</GEOL_GEOL>
          <GEOL_DESC>0' Start with air drilling 2' Rock hit</GEOL_DESC>
        </LAYER>
       [...]
      </GEOL>
      <INSITU_TESTS>
        <ISPT>
          <ISPT_TOP>7.50</ISPT_TOP>
          <ISPT_REP>5,9,9</ISPT_REP>
        </ISPT>
       [...]
      </INSITU_TESTS>
      <SAMPS>
        <SAMP ID="1">
          <SAMP_REF>S1</SAMP_REF>
          <SAMP_TOP>3.50</SAMP_TOP>
          <SAMP_BASE>4.5</SAMP_BASE>
          <SAMP_TYPE>B-1</SAMP_TYPE>
        </SAMP>
        [...]
      </SAMPS>
    </HOLE>
  </HOLES>
</BOREHOLE>
```

Figure 2-16. XML file for SPT borehole test.

2.5.2 Geotechnical Information Management and Exchange (GIME) Design

Geotechnical information on soil deposits is critical for our civil infrastructure. Local, state and federal agencies, universities, and companies need this information for a variety of civil engineering and urban policies applications, including land usage and development, and mapping of natural hazards such as soil liquefaction and earthquake ground motions. Along the improvement of data collection and digital technologies, more and more geotechnical borehole data from the field, laboratory or office are directly produced in, or converted to a digital format. This makes its possible to use, share and disseminate geotechnical data nationwide by coordinating geotechnical data standard and Internet dissemination activities within large organization or government agencies. With the recent ubiquity of communication networks – particularly the Internet – the trend towards electronic storage and exchange of geotechnical borehole data has accelerated. We have proposed the use of XML as the preferred format for storage and exchange of borehole data. XML offers many advantages over other data formats for borehole data. However, in addition to new data formats for borehole data, there is much research to be done to improve the exchange and utilization of geotechnical information over the Internet.

In this section we introduce our prototype for Geotechnical Information Management and Exchange -- GIME. The architecture makes extensive use of Web services to provide access to these valuable data sets for the expert practitioners as well as the general public. Each component of the proposed system is described in detail.

Figure 17 illustrates the architecture of the GIME system. Multiple, distributed geotechnical data archives are accessible via the Internet. These repositories are under different administrative control, for example, the US Geological Survey provides some of their information to the public. We distinguish two types of archives on the basis of what data access they allow: read-write (RW) or read-only (RO). RW archives host three geotechnical Web services, an XSLT (XSL Transformations) processor, and a database (with XML and spatial data query support). The three Web services that are implemented within the application server provide the interface for distributed applications to store (File Storage Web Service, FSWS), query and retrieve (Query & Exchange Web Service, QEWS) and visualize (Visualization Web Service, VWS) the geotechnical information. RO archives implement only the QEWS Web service to access their database.

The services use the Simple Object Access Protocol (SOAP) as the communication protocol between the server and clients. A complete Web Service Description Language (WSDL) file of the system provides two pieces of information: an application-level service description (abstract interface), and the specific protocol dependent details that users must follow to access the service at a specified concrete service endpoint. These services will be registered to an Universal Description Discovery and Integration (UDDI) server and users can retrieve the information about these services from the Internet. The client program can use its service proxy to request these services from the GIME system.

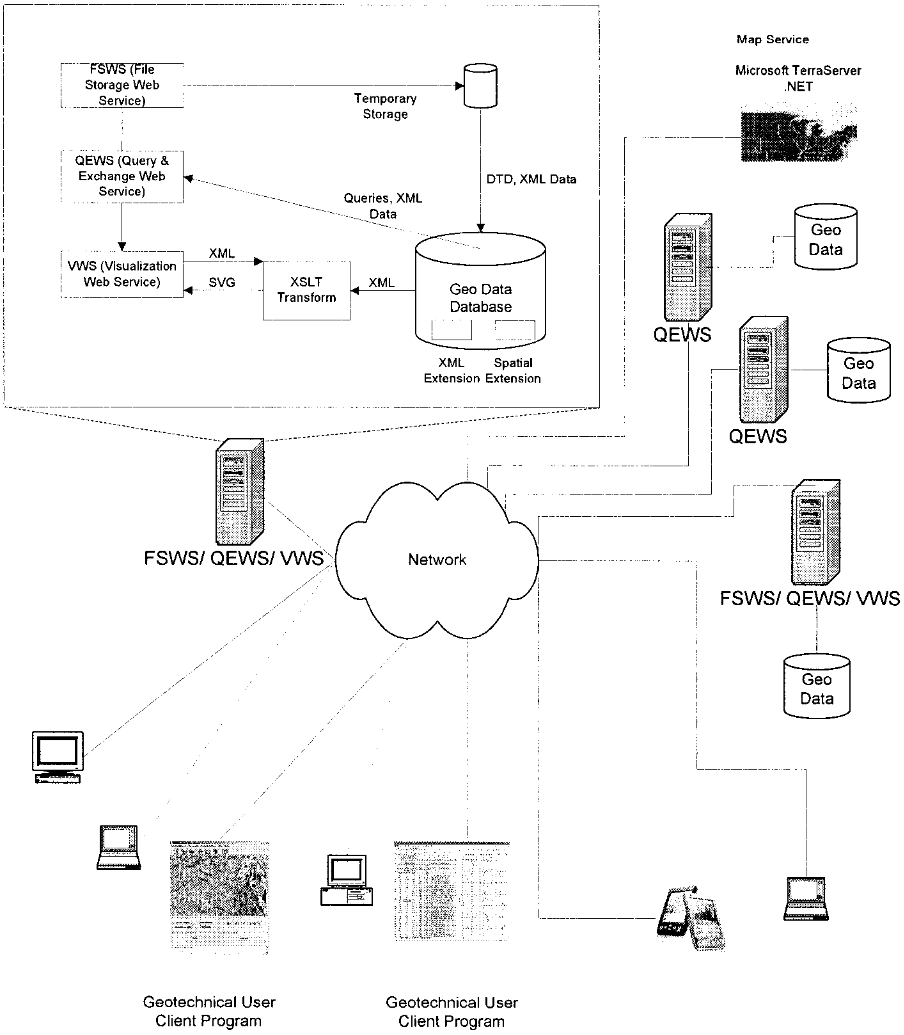

Figure 2-17. Geotechnical Information Management and Exchange (GIME) architecture.

All the GIME functions are implemented with Web Service technology. One major advantage of Web Service is that users can use their familiar programming languages or tools (e.g. Microsoft Visual Studio .NET, IBM WebSphere) to develop the client programs. Once users got the Web Service Definition Language (WSDL) file, they can invoke these remote functions via using their ports and function names defined in the WSDL file. All the communication data are in XML format and follow the

Simple Object Access Protocol (SOAP). The Apache Axis component is responsible for adding and removing SOAP envelops during the communication. All the parameters and names of functionalities are defined in the WSDL file which can be accessed from GIME archive (http://datalab.usc.edu:8080/axis/jdbc_db2s.jws?wsdl) hosted at a server physically located at the University of Southern California. The detail information about the three Web services has been explained in the following.

Functions of the Query & Exchange Web Services

The functions here are for users to query and download these borehole files inside the GIME database. The query function is the most common use method in the GIME system. Users can use the six query conditions for getting the borehole meta-data which fulfill their terms. All the result information (borehole meta-data) are stored in a struct and returned to users. Users can utilize these borehole meta-data directly or take one step ahead to download the complete borehole XML file.

Functions of the Visualization Web Services

The information which users can get from the borehole meta-data is kind of limited. Therefore, the visualization function is provided and users can see the two dimensional (2-D) SVG images of borehole files. The geology layers and geotechnical test information (e.g. CPT, SPT, etc.) are rendered in the SVG image. Users can make their decision if they want to download the complete borehole XML file after seeing the 2-D image.

Functions of the File Storage Web Services

The main purpose of these file storage service is for users to upload their borehole files and share them with other users. Users can upload their own borehole files into the GIME database. All the uploaded files must follow the DTD of this project. The GIME server will verify the uploaded file and if the file is not valid, it will be rejected and an error message is prompted.

2.5.3 Soil classification client application using GIME

Lots of geotechnical engineering softwares utilize borehole data to carry out the geotechnical tasks for subsurface investigation, seismic liquefaction analysis and ground deformation assessment. Using GIME system, not only the geotechnical borehole data can be distributed and exchanged more efficiently, at the mean time the existing engineering software can directly access the large amount the geotechnical information through the web methods provided by the GIME web service WSDL file. In this section, a detail implementation of a client application for soil classification using the GIME archive remotely has been explained, which illustrate the seamless integration of GIME web methods with existing engineering program.

This client software was developed based on an existing soil classification Excel VBA program. The existing VBA program uses borehole data residing in local hard drive. In this enhanced client application, the borehole data will be queried and retrieved through the GIME Web service, and imported to the VBA program for analysis. Figure 18 shows the framework of this soil classification client application using Web services. The application has three main functionalities; 1) data query and retrieval via Web service; 2) borehole XML format viewing and converting; and 3) soil classification which is existing VBA program.

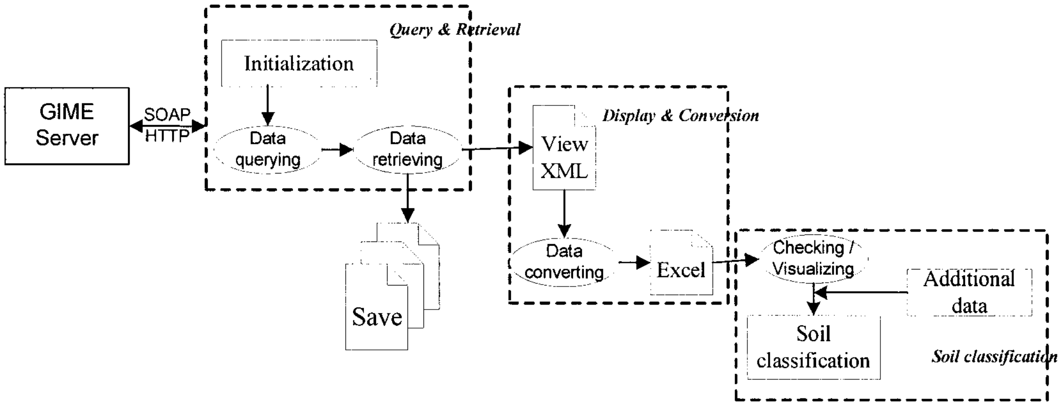

Figure 2-18. Framework of the VBA client application for soil classification.

In order to utilize Web service functionalities in Excel VBA environment, the Web service References Tool 2.0 has been added into Visual Basic Editor. The Web service References Tools is a program interface distributed with the Office XP Web services Toolkit free of charge, which provides an interface to wrap the necessary function calls for discovering Web services, selecting the services, and creating classes that act as Web service proxies for the VBA program. Using the Web service References Tools, single or multiple the GIME Web services WSDL file can been imported into VBA directly, and automatically a proxy class is added to the VBA program. The proxy class is added to the VBA program as a class module named automatically as "clsws_jdbcdb2sService", which is a VBA class representation of the Web service as defined by http://datalab.usc.edu/axis/jdbc_db2s.jws?wsdl. Since this proxy class wraps calls to the GIME Web service, a client developer or user does not need to write any code to directly interact with SOAP and MSXML, which greatly reduces the complexity of the Web service application development. The nomenclature of the class module is the name of the Web service prefixed with "clsws_". To use this class, user can dimension a variable as new clsws_jdbcdb2sService, for instance,

Dim geoWS As New clsws_jdbcdb2sService

Here *geoWS* is the variable that contains all the remote functions (web methods) provided in GIME WSDL file and ready for use as the local function for VBA user modules.

Figure 19 shows the interface of the Web service client application for soil classification. The three main functionalities in Figure 18 are implemented through this user friendly interface. When the user want to query and retrieve borehole data from a remote Web service, the initialization module will make the connection with the GIME File Storage and Query Web service (FSWS and QWS) to check the availability of those service. If service is available, meta data will be send back to client application to inform about where are the sites that contain borehole data and how many borehole data sets can be provided in each of these sites. This information is then added to the "Site" list box to assist with a specific user query as seen in Figure 19. A text based query interface has been designed to facilitate the user to specify the desired parameters to search the GIME database for more specific borehole information. The text based query will be formed as a standard SQL query by the VBA module and sent to the Web service via the SOAP protocol. The query has been submitted to the GIME system through the network by the following code ,

```
sqlrst = geoWS.wsm_geoQueryExcel(sqltext)
```

function *geoQueryExcel* has been invoked with standard query lined up in string *sqltext*. The remote GIME Web service response the inquire by sending back a string *sqlrst* contains a set of the unique identification number of each qualified borehole file. Each unique borehole file identification number has been intercepted from string *sqlrst* and listed in the query result box as shown in left bottom part of Figure 19. Clicking any one of the identification number in the list box, the individual XML borehole file will be retrieved through the following code

```
xmltext = geoWS.wsm_geoGetXMLFile(uid)
```

where geoGetXMLFile will invoke the SOAP call to the GIME web service, *uid* represents the file identification number, and *xmltext* is returned XML borehole file.

The retrieved XML borehole file will be loaded into memory and processed in this liquefaction program using XML Document Object Model (DOM) (W3C 2002). The XML DOM, which represents a tree view of the XML document, is a programming interface for HTML and XML documents. It defines the way a document can be accessed and manipulated. Using a DOM, a programmer can create a document, navigate its structure, and add, modify, or delete its elements. The XML document object contains several child objects to represent different node in the XML file such as element, attribute, and declaration. The following code create the DOM in VBA user module by instantiating the XML document class

```
Dim xmldoc as New XmlDocument()
```

The detail explanation and programming of XML document object can be found in any standard XML programming books (Fred Barwell et al. 2002; Balena, F. 2002). Figure 20 shows the subroutine that can load an XML file into an XMLDocument object and display the XML borehole file in a TreeView control (as shown in Figure 19). The hierarchy structure of XML file has been disassembled using the recursive calling of this subroutine. Each child note of element "BOREHOLE" has been visited and presented in the tree view control box. The liquefaction application program also provide the option to save the queried results onto the local computer system in XML format.

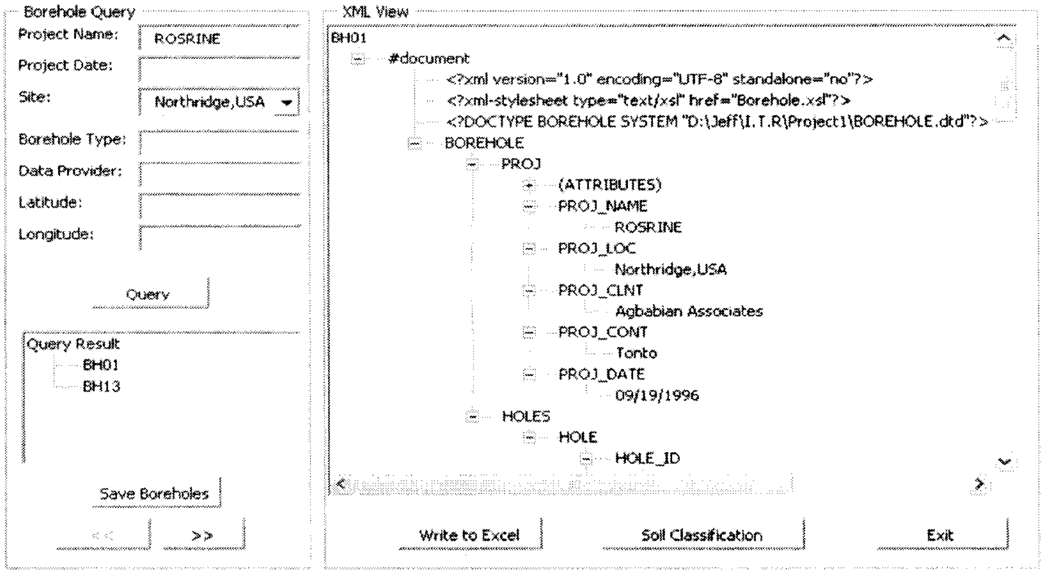

Project Name: ROSRINE
Project Date:
Site: Northridge,USA
Borehole Type:
Data Provider:
Latitude:
Longitude:

Query Result
- BH01
- BH13

```
BH01
#document
    <?xml version="1.0" encoding="UTF-8" standalone="no"?>
    <?xml-stylesheet type="text/xsl" href="Borehole.xsl"?>
    <?DOCTYPE BOREHOLE SYSTEM "D:\Jeff\I.T.R\Project1\BOREHOLE.dtd"?>
    BOREHOLE
        PROJ
            (ATTRIBUTES)
            PROJ_NAME
                ROSRINE
            PROJ_LOC
                Northridge,USA
            PROJ_CLNT
                Agbabian Associates
            PROJ_CONT
                Tonto
            PROJ_DATE
                09/19/1996
        HOLES
            HOLE
                HOLE_ID
```

Figure 2-19. User interface of the soil classification program showing the queried result and XML tree structure of the borehole.

```
Sub DisplayXMLNode(ByVal xmlnode As IXMLDOMNode, ByVal root As String, ii)
    ' Add a TreeView node for this XmlNode.
    ' (Using the node's Name is OK for most XmlNode types.)
    Dim tvnode As Node
    Set tvnode = tvXML.nodes.Add(root, tvwChild, xmlnode.nodeName & ii, xmlnode.nodeName)
    root = xmlnode.nodeName & ii
    ii = ii + 1
    Select Case xmlnode.nodeType
       Case NODE_ELEMENT
         {...}
      Case NODE_TEXT, NODE_CDATA_SECTION
         {...}
      Case NODE_COMMENT
         {...}
      Case NODE_PROCESSING_INSTRUCTION, NODE_NOTATION
         {...}
      Case Else           ' ignore other node types.
    End Select
    Dim xmlChild As IXMLDOMNode
   Set xmlChild = xmlnode.FirstChild
    Do Until xmlChild Is Nothing              ' Call this routine recursively for each child node.
      Call DisplayXMLNode(xmlChild, root, ii)
      Set xmlChild = xmlChild.nextSibling
    Loop
  End Sub
```

Figure 2-20. Sample code of subroutine to convert the XML file into a tree view control box.

The user can inspect each borehole in the XML view box and convert the XML data to a spreadsheet in tabulated format. The application will automatically convert boreholes to different tabulated formats according to each borehole type. Sample code that transfer the contents of "CPT" element in XML borehole file into Excel spreadsheet has been illustrated in Figure 21. The XML file has been loaded using *LoadXML* function, which is one method provided in XML document object. The "CPT" element in the hierarchy structure of XML file is been accessed through *getElementsByTagName*. Each "CPT" element, which contains the values for depth, CPT tip resistance qc and sleeve friction Sf, is parsed and written sequentially onto spreadsheets (Figure 22). Figure 22 illustrates the CPT soil classification obtained by CSC. The contents of other elements can be retrieved and transferred to spreadsheet using similarly manner. As pointed in the Figure 18, one should be aware that XML borehole file can be converted to any type of engineering preferred format using same approach which not only limited to Excel spreadsheet.

```
i = 7   'row number in spreadsheet for pasting CPT data
Set xmln = xmldoc.getElementsByTagName("CPT")
For k = 1 To xmln.Length 'read Qc and Sf at each depth
 Set xmlnode = xmln.Item(k - 1)
 Set xmlChild = xmlnode.FirstChild
 j = 0
 Do Until xmlChild Is Nothing
  j = j + 1
  .Cells(i, j).Value = xmlChild.nodetypedvalue
  Set xmlChild = xmlChild.nextSibling
 Loop
 i = i + 1
Next k
```

Figure 2-21. Excerpt from VBA code extracting names and values of variable CPT from a XML borehole file and pasting them into an Excel spreadsheet.

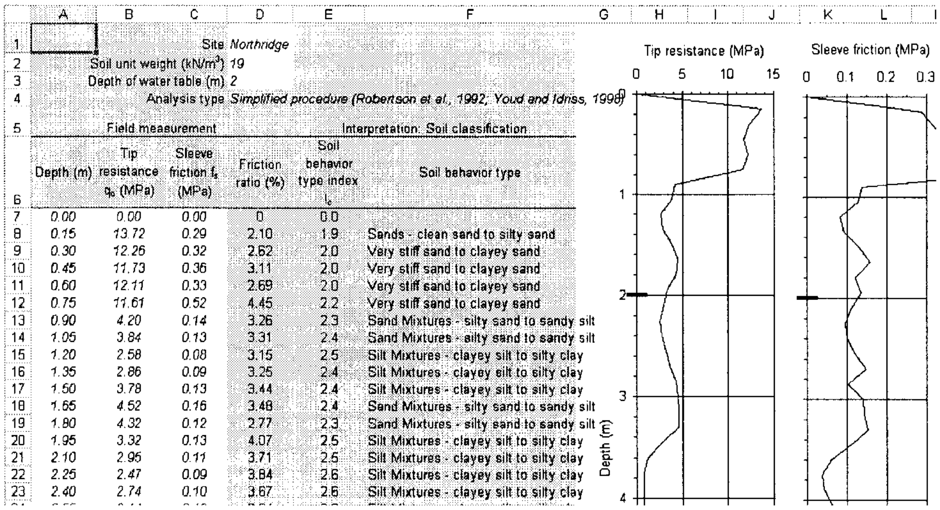

Site *Northridge*
Soil unit weight (kN/m^3) *19*
Depth of water table (m) *2*
Analysis type *Simplified procedure (Robertson et al., 1992; Youd and Idriss, 1998)*

Field measurement			Interpretation: Soil classification		
Depth (m)	Tip resistance q_c (MPa)	Sleeve friction f_s (MPa)	Friction ratio (%)	Soil behavior type index I_c	Soil behavior type
0.00	*0.00*	*0.00*	0	0.0	
0.15	*13.72*	*0.29*	2.10	1.9	Sands - clean sand to silty sand
0.30	*12.26*	*0.32*	2.62	2.0	Very stiff sand to clayey sand
0.45	*11.73*	*0.36*	3.11	2.0	Very stiff sand to clayey sand
0.60	*12.11*	*0.33*	2.69	2.0	Very stiff sand to clayey sand
0.75	*11.61*	*0.52*	4.45	2.2	Very stiff sand to clayey sand
0.90	*4.20*	*0.14*	3.26	2.3	Sand Mixtures - silty sand to sandy silt
1.05	*3.84*	*0.13*	3.31	2.4	Sand Mixtures - silty sand to sandy silt
1.20	*2.58*	*0.08*	3.15	2.5	Silt Mixtures - clayey silt to silty clay
1.35	*2.86*	*0.09*	3.25	2.4	Silt Mixtures - clayey silt to silty clay
1.50	*3.78*	*0.13*	3.44	2.4	Silt Mixtures - clayey silt to silty clay
1.65	*4.52*	*0.16*	3.48	2.4	Sand Mixtures - silty sand to sandy silt
1.80	*4.32*	*0.12*	2.77	2.3	Sand Mixtures - silty sand to sandy silt
1.95	*3.32*	*0.13*	4.07	2.5	Silt Mixtures - clayey silt to silty clay
2.10	*2.95*	*0.11*	3.71	2.5	Silt Mixtures - clayey silt to silty clay
2.25	*2.47*	*0.09*	3.84	2.6	Silt Mixtures - clayey silt to silty clay
2.40	*2.74*	*0.10*	3.67	2.6	Silt Mixtures - clayey silt to silty clay

Figure 2-22. Soil classification using CPT data fetched through GIME Web service.

This client application for soil classification demonstrates a fundamentally new framework and set of standards that can integrate servers, workstations, and desktop clients using Web service for routine engineering analysis. Because Web services can utilize the combined information and services that are maintained on a distributed network, they are appealing to local governments, academic and other organizations that have departments that independently collect and manage data but must integrate these datasets. At the mean time, it brings a new vision to broaden the way for engineering software application.

2.6 Conclusion

The existing data sets on liquefaction-induced ground displacement were identified, collected, organized and digitized especially those from the 1994 Northridge earthquake and 1995 Hyogoken-Nanbu earthquake. A relational database framework was developed for storing the large amount of data on liquefaction-induced ground deformation, including the data sets on displacement vectors and soil SPT and CPT boreholes. Two relational databases LIDD and BOD were developed for structuring and storing the large amount of data on liquefaction-induced ground deformation, including the data sets on displacement vectors and soil SPT and CPT boreholes. LIDD, which stands for Liquefaction-Induced ground Deformation, contain displacement vectors and earthquake characteristics. BOD, an acronym for BOrehole Database, contains all soil properties profiles in the areas of liquefaction-induced ground deformation. Both LIDD and BOD are compatible with GIS techniques. The LIDD database contains 16,000 displacement vectors, and the BOD database 902 SPT and 229 CPT soundings. The complete set of ground deformation data and geotechnical information provide enough information for developing and improving the methods for assessing and quantifying the liquefaction potential of ground deformation, and developing new generations of models for liquefaction-induced deformation.

For geotechnical data exchange, we propose a system architecture called GIME which emerging Web services standard to build infrastructures in the geotechnical and other distributed data integration projects. This system handles geotechnical data via an XML format on a distributed platform that interoperates via Web services. The functionality and usability of GIME was illustrated with a VBA client applications program for soil classification. GIME demonstrates that Web services can efficiently integrate across servers and clients the geotechnical information and services which are distributed geographically and maintained independently.

3 SPATIAL MODELING OF EARTHQUAKE-INDUCED GROUND DEFORMATION AND CASE STUDY IN KOBE PORT-ISLAND

3.1 Introduction

Liquefaction-induced ground deformation was observed after earthquakes to cover areas as large as a few square kilometers. With amplitude ranging anywhere from a few centimeters to several meters, liquefaction-induced ground deformation caused substantial damages to lifelines and pile-foundations of buildings and bridge piers during past earthquakes (e.g., Hamada et al. 1996a; Hamada and O'Rourke 1992). Liquefaction-induced ground deformation was studied using different approaches, including empirical models, centrifuge models, shake table models, and computational models (e.g., Bardet 2003). Among all existing models, empirical models offer the most pragmatic approach for predicting the liquefaction-induced ground deformation over large areas due to their limited number of model parameters. Present empirical models include Hamada et al. (1986); Youd and Perkins (1987); Bartlett and Youd (1992, 1995); Rauch (1997); Bardet et al. (1999b and 2002); and Youd et al. (2002). Empirical models predict liquefaction-induced ground displacements in terms of seismic, topographical and geotechnical parameters. They can be applied for mapping areas prone to deformation due to liquefaction during future earthquakes. Such a liquefaction hazard mapping, which is under evaluation by the California Geological Survey, has far-reaching implications in assessing and mitigating the risks to lifeline networks and civil infrastructures.

The use of empirical models for mapping ground-deformations hazards raises many questions. For instance, can empirical models, although based on spatially unrelated data, describe the spatial variation of ground deformation? What are the uncertainties of empirical model in predicting liquefaction-induced ground deformation? Can empirical models, although calibrated from case histories prior to 1990, describe case histories after 1990? In an attempt to answer some of these questions, this chapter proposes a methodology for predicting liquefaction-induced ground deformation, which is based on geostatistics (e.g., Chiles and Delfiner 1999; and Wackernagel 1995) and the Multiple Linear Regression (MLR) ground deformation model of Bardet et al. (2002).

Following the introduction, the first section proposes the detailed methodology of ground deformation prediction. The second section describes the geostatistics tools for spatial analysis over large areas. Following that, the uncertainty of ground deformation predication has been addressed to consider the spatial interpolation error and empirical MLR model error. The fourth section examines the applicability of the methodology in a case study in Port Island of Kobe city, Japan, after the 1995 Hyogoken-Nanbu earthquake, and attempts to examine the performance of MLR model for an earthquake from which it was not calibrated. Based on the case history, the last section investigates the uncertainties in predicting ground deformations, and makes some recommendation for improving liquefaction hazard mappings.

3.2 Methodology for prediction of earthquake induced ground deformation

Figure 1 summarizes the proposed methodology for predicting liquefaction-induced ground deformation, which includes the extraction and generation of model parameter values over areas under consideration, spatial analysis of model parameters and MLR empirical model application.

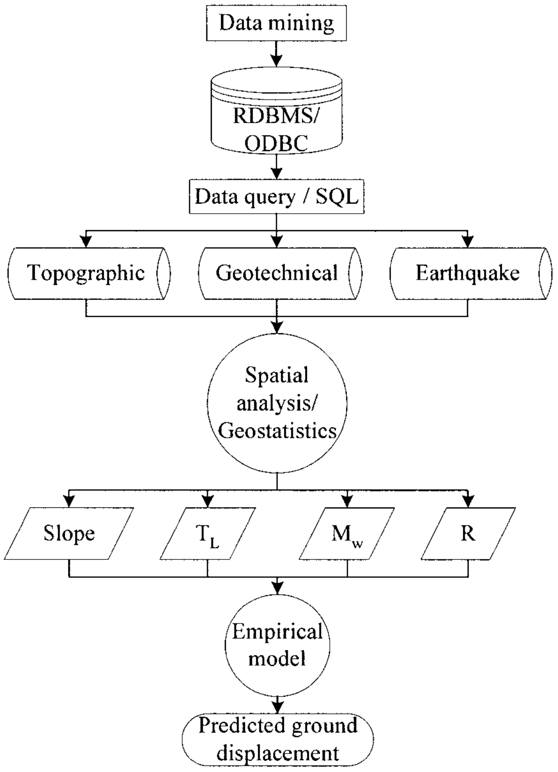

Figure 3-1. Methodology for extracting/generating model parameters and predicting liquefaction-induced ground deformation.

One should obtain the necessary data such as elevation, borehole information for the analysis region through different sources. The more efficient way is to query from the liquefaction-induced ground deformation database LIDD and BOD through

ODBC (Open Database Connection) or other geotechnical database system. Geostatistical spatial analysis tools will be used to explore the spatial continuity and generate the regional surface data, including slope, liquefied layer thickness and corresponding earthquake information such as magnitude and source distance. Based on the surface information in the region, permanent ground deformation will be calculated using the four-parameter MLR model. This framework to predict liquefaction induced ground deformation has been developed using the spatial analysis and database capabilities of GIS system. The computation result can be manipulated by additional GIS extension such as spatial analysis or 3D analysis to study the phenomena thoroughly. Using these tools, hazard mapping of liquefaction induced ground deformation can be generated to help engineers to understand the phenomena and perform the mitigation.

3.2.1 Empirical ground deformation model

For predicting liquefaction-induced ground deformation in gently sloping grounds free of topographic irregularities, Bardet et al. (2002) proposed the following four-parameter MLR model:

$$\begin{aligned} Log(D+0.01) = &-6.815 + 1.017 M_w - 0.278 LogR - 0.026 R \\ &+ 0.454 LogS + 0.558 LogT_L \end{aligned} \tag{3-1}$$

where D is the predicted displacement (m); M_w is the moment magnitude; R is the distance to earthquake source (km); S is the ground slope (%); and T_L is the thickness of liquefiable layer (m).

When the fault rupture can be projected onto the ground surface as segment **AB**, the value of R at point M is the distance between point M and segment **AB**, i.e.:

$$R = d(M, \mathbf{AB}) = \frac{\mathbf{AB} \times \mathbf{AM}}{AB} = \frac{(y_A - y_B)x + (x_B - x_A)y + x_A y_B - x_B y_A}{\sqrt{(x_B - x_A)^2 + (y_B - y_A)^2}} \quad (3\text{-}2)$$

where (x_A, y_A), (x_B, y_B), and (x, y) are the x- and y-coordinates of points A, B and M, respectively. Recognizing that fault ruptures have finite lengths, R is calculated using Eq. 2 provided that point M projects onto segment AB; otherwise R is taken as the minimum of distances MA and MB, i.e., $R = \min(MA, MB)$. Far away from the fault, the segment AB becomes small compared to AM, which implies that $R = AM$.

The value of T_L is determined from the cumulative thickness of layers, which satisfy three conditions: (1) below the ground water table, (2) $(N1)_{60}$ less than 15, and (3) clay content f less than 15%. T_L can be expressed as follows:

$$T_L = \sum_{i=1}^{n} F\left(z_i, z_w, (N1)_{60}^{i}, f_i\right) \Delta H_i \quad (3\text{-}3)$$

where z_w is the elevation of the water table, and z_i is the elevation at the top of the i$^{\text{th}}$ layer, which has a thickness ΔH_i and properties $(N1)_{60}^{i}$ and f_i. The function F is:

$$F\left(z, z_w, (N1)_{60}, f\right) = \begin{cases} 1 & \text{if } z \geq z_w \text{ and } (N1)_{60} \leq 15 \text{ and } f < 15\% \\ 0 & \text{Otherwise} \end{cases} \quad (3\text{-}4)$$

The ground slope S is usually determined using the grid points of digital elevation models. The slope $S_{i,j}$ at grid point i,j is calculated from the elevation $z_{i,j}$ at neighboring grid points as follows:

$$S_{i,j} = \sqrt{SX_{i,j}^2 + SY_{i,j}^2} \tag{3-5}$$

where $SX_{i,j}$ and $SY_{i,j}$ are the slopes in the EW and NS-direction, respectively, which are calculated using a 3x3 moving average, i.e.:

$$\begin{aligned} SX_{i,j} &= \frac{z_{i-1,j-1} + 2z_{i-1,j} + z_{i-1,j+1} - z_{i+1,j-1} - 2z_{i+1,j} - z_{i+1,j+1}}{8\Delta x} \\ SY_{i,j} &= \frac{z_{i-1,j-1} + 2z_{i,j-1} + z_{i+1,j-1} - z_{i-1,j+1} - 2z_{i,j+1} - z_{i+1,j+1}}{8\Delta y} \end{aligned} \tag{3-6}$$

In Eq. 6, Δx and Δy are the grid spacing in the EW and NS directions, respectively.

The development of Eq. 1 is detailed in Bardet et al. (2002). The coefficients of Eq. 1 were calibrated from the Bartlett and Youd (1992) database, which contains data from earthquakes that occurred before 1990, and which excludes data from the 1994 Northridge, California, earthquake and 1995 Hyogoken-Nanbu, Japan, earthquake. In theory, other empirical models (e.g., Youd et al. 2002) could also be considered in the present study. Such comparative studies will be the subject of future work.

3.2.2 Generation of model parameters

Equation 1 requires three types of data, i.e., topographic, stratigraphic and seismic data. The data specific to the areas under study can be obtained from literatures or queried from geotechnical database (Bardet et al. 2002). The ground deformation, topographic and stratigraphic data, which are referenced with geographic coordinates, are scattered in space, and have different density and location. For instance, boreholes have locations different from measured displacements. Boreholes also do not align with the grid coordinates of digital elevation models (DEM). Geospatial analysis is required to generate continuous fields of model parameters (e.g., S and T_L) from scattered data, and is critical for determining model parameters and applying the MLR model for ground deformations. The methodology of Fig. 1 was implemented in a geographic information system (GIS) framework, which provides users with a graphical environment for identifying data in the study area, querying input data, generating continuous fields of model parameters, predicting ground displacements, and comparing predicted and measured ground displacements when those are available. The methodology of Fig.1 can be extended for mapping liquefaction hazards and risks to lifeline networks, provided that fragility curves are available for assessing damage to lifelines components. Using this methodology, engineers and planners can map the hazards of liquefaction induced ground deformation, better understand the amplitude and extent of liquefaction, and perform relevant mitigation to lifelines and civil infrastructures.

3.3 Geostatistical analysis

The model parameters S and T_L of Eq. 1 vary depending on the topography and soil stratigraphy. Their values are usually known only at scattered locations. The proposed methodology uses geostatistics (e.g., Chiles and Delfiner 1999; Wackernagel 1995) to interpolate fields of model parameters over the study area. Geostatistics is the application of the theory of stochastic processes to natural spatial phenomena. It enables us to see how variables such as soil properties measured at different points in space are related. More importantly from the practical viewpoint, such relationships can be used for estimating values at sites where no measurements are taken. Geostatistics is useful for understanding the distribution of model parameters in the study areas, and to build parameter fields from other parameter fields, e.g., ground slope from elevation data. Two types of geostatistics tools, semivariogram and Kriging, will be introduced explore the characteristics of model parameters.

3.3.1 Semivariogram of spatial data

The semivariogram and the spatial correlation coefficient are the tools that usually taken for the measurements of spatial characteristics. Considering the field measurements $Z(x_i)$ at locations x_i, $i = 1, \cdots, n$, as a particular realization of random function $Z(x)$, based on the stationary in the context of stochastic process, the mathematical expectation of the stochastic process $Z(x)$ is the mean of all possible realizations of the process at point x. The association of the values taken by the process $Z(x)$ at two point x_1 and x_2 is represented by the spatial covariance function,

$$Cov[Z(x_1), Z(x_2)] = E\{[Z(x_1) - m][Z(x_2) - m]\} = E[Z(x_1)Z(x_2)] - m^2 \qquad (3\text{-}7)$$

Here m is the mean value of the stochastic process $Z(x)$. The alternate definition, which is commonly used in the estimation problems, is that of the semivariogram, or variogram (Chiles and Delfiner 1999),

$$\gamma(x_1 - x_2) = \gamma(h) = \frac{1}{2} Var[Z(x_1) - Z(x_2)] \qquad (3\text{-}8)$$

here h is the absolute value of the distance between point x_1 and x_2. In a probabilistic framework, the definition of the semivariogram involves the assumption that although the random function varies from place to place, the semivariogram is independent of location and depends only on the distance of the pair of varieties being considered. The difference between Eq. 7 and Eq. 8 is that the covariance is a direct function of the association between two variables, whereas the semivariogram measures the disassociation.

Figure 2 shows a general semivariogram model of $\gamma(h)$. The typical semivariogram saturates to a constant value (i.e., sill) for a certain distance called *range*. The range represents the distance beyond which there is no correlation between spatial points. In theory, $\gamma(h) = 0$ when $h = 0$. However, the semivariogram often exhibits a nugget effect at very small lag distance, which reflects usually measurement errors and microstructure (e.g., Bailey and Gatrell 1996). The semivariogram does not require knowledge of the mean of the random function for its estimation. This advantage makes it a prefer estimation model for interpolation problem.

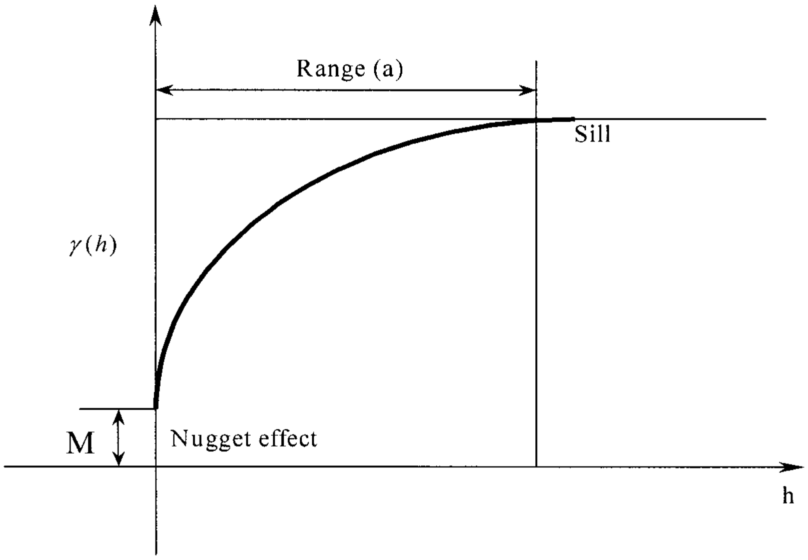

Figure 3-2. Typical variogram structure with a nugget effect indicating the sill value and range.

An estimate of the semivariogram from sample data sets is called an experimental semivariogram, i.e.:

$$\hat{\gamma}(h) = \frac{1}{2k}\sum_{i=1}^{k}\left[Z(x) - Z(x+h)\right]^2 \tag{3-9}$$

where k is the total number of observations separated by the distance h. In practice, Eq. 9 is evaluated for evenly spaced values of h using a lag tolerance Δh, and k is the number of points falling between h-Δh and h+Δh. Experimental semivariogram can be fitted using spherical, exponential or Gaussian models (e.g., Chiles and Delfiner 1999) to obtain the model semivariogram representing the spatial characteristics of the random function.

The semivariogram is considered to be isotropic when variations in the azimuth do not produce significant changes in the experimental semivariogram and otherwise is anisotropic. The isotropic variogram of Eq. 9 can be generalized for anisotropic cases when data depend not only on distance but also on direction:

$$\hat{\gamma}(\mathbf{h}) = \frac{1}{2k(\mathbf{h})}\sum_{i=1}^{k(\mathbf{h})}\left[Z(\mathbf{x}_i + \mathbf{h}) - Z(\mathbf{x}_i)\right]^2 \tag{3-10}$$

where **h** is the vector that separates point $\mathbf{x}_i$ and $\mathbf{x}_k$; $k(\mathbf{h})$ is the number of pairs of variables at distance **h** apart. Directional analysis must be performed to identify the anisotropic information for the semivariogram. In practice, anisotropic semivariograms are determined by partitioning data in directional bins (Isaaks and Srivastava 1990). Anisotropy is detected when the range or sill changes significantly with direction.

Although the semivariogram is, in general, a continuous vectorial function of h, discontinuous sampling precludes estimation of the experimental semivariogram for every possible value of the lag. In practice the estimation maybe limited to a few points and directions. A favorable situation occurs when sampling is performed at the nodes of a square grid. Then estimates can be made at fixed multiples in directions. The most common situation is that data at irregular locations. The practice in this case calls for the grouping of distances and directions into classes as shown in Figure 3. All points in the shaded area belong to the same distance class relative to the point in the upper left corner. A safe practice is to take a lag interval equal to the average distance to the nearest neighbor, lateral bounds equal to twice the lag interval, and an angular tolerance of 22.5 degrees (Olea 1999).

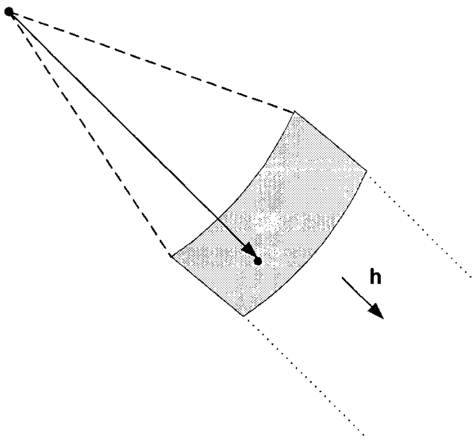

Figure 3-3. A distance class for semivariogram estimation along direction h. The shaded area is the region where pair distance belongs to same range.

3.3.2 Kriging estimation of spatial data

The semivariogram unleash the spatial characteristic of regional random function. With this information, the unknown value at specific location can be estimated using certain geostatistics tools. Assuming that the expected value $\hat{Z}(x_k)$ of variable Z at location x_k can be interpolated as follows:

$$\hat{Z}(x_k) = \sum_{i=1}^{n} \lambda_i Z(x_i) \tag{3-11}$$

where $Z(x_i)$ represents the known value of variable Z at point x_i; λ_i is the interpolation weight function, which depends on the interpolation method; and n is the total number of points used in the interpolation. Most GIS software (e.g., ArcGIS 2002; and GoldenSoftware 1997) include two types of spatial interpolation, i.e., Inverse Distance Weighting (IDW) and Kriging (e.g., Chiles and Delfiner 1999). The IDW method assumes that λ_i decreases with the distance d_i between points x_k and x_i:

$$\hat{Z}(x_k) = \sum_{i=1}^{n} Z(x_i) / d_i^{\alpha} \tag{3-12}$$

where α is a positive factor controlling the decrease in λ_i with d_i. IDW works best with evenly distributed points, but generates errors for unevenly distributed data clusters. It is vulnerable to outliers, which corresponds to "bull eyes" contours centered about unusually large or small values, and cannot assess the uncertainties of estimated values.

Kriging overcomes the shortcomings of IDW by minimizing the variance of estimation (Chiles and Delfiner 1999). Kriging is developed within the scope of a second-order statistical model involving only the mean $m(x)$ and the covariance function $\sigma(h)$ or the semivariogram $\gamma(h)$. Usually three main types of Kriging have been used more commonly as listed in Table 1.

Table 3-1. Main types of Kriging method according to mean and variance.

Type	Mean	Variance
Simple Kriging	Known, constant	Covariance
Ordinary Kriging	Unknown, constant	Semivariogram
Universal Kriging	Unknown, varying	Semivariogram

Simple Kriging assume a constant known mean value of a stationary random function $Z(x)$. If the mean value is unknown in advance, ordinary Kriging or universal Kriging can be used for interpolation.

For the point estimation using simple Kriging, the value Z_0 at given location from n observations $Z_1,\dots,Z_n$ can be estimated as

$$\hat{Z}_0 = \sum_{i=1}^{n} \lambda_i (Z_i - m) + m \tag{3-13}$$

where m is the constant known mean value and the weights λ_i are selected so as to minimize the mean square error of $E(\hat{Z}_0 - Z_0)^2$ which is defined in Eq. 14.

$$E(\hat{Z}_0 - Z_0)^2 = Var(\hat{Z}_0 - Z_0) + \left[E(\hat{Z}_0 - Z_0)\right]^2 \tag{3-14}$$

Since $E(\hat{Z}_0 - Z_0) = 0$ (constant mean value), we have

$$E(\hat{Z}_0 - Z_0)^2 = Var(\hat{Z}_0 - Z_0) = \sigma_0^2 \tag{3-15}$$

which coincides with the variance at the estimated point.

Substituting Eq. 13 into Eq. 15 and after some mathematics derivation, we can obtain

$$\begin{aligned}\sigma_0^2 &= \sum_{i=0}^{n}\sum_{j=0}^{n} \lambda_i \lambda_j Cov\left[Z(x_i), Z(x_j)\right] = Cov\left[Z(x_0), Z(x_0)\right] \\ &\quad -2\sum_{i=1}^{n} \lambda_i Cov\left[Z(x_i), Z(x_0)\right] + \sum_{i=1}^{n}\sum_{j=1}^{n} \lambda_i \lambda_j Cov\left[Z(x_i), Z(x_j)\right]\end{aligned} \tag{3-16}$$

with $\lambda_0 = -1$. To minimize the mean square error by taking the first derivatives of Eq. 16, we have

$$\frac{\partial \sigma_0^2}{\partial \lambda_i} = -2Cov\left[Z(x_i), Z(x_0)\right] + 2\sum_{j=1}^{n} \lambda_j Cov\left[Z(x_i), Z(x_j)\right] = 0 \tag{3-17}$$

and the weight λ_i of simple Kriging system is obtained by solving the system equations,

$$\sum_{j=1}^{n} \lambda_j Cov\left[Z(x_i), Z(x_j)\right] = Cov\left[Z(x_i), Z(x_0)\right], \quad i = 1, 2, \ldots, n \tag{3-18}$$

Substituting the solution of λ_i into Eq. 16, the minimum mean square error of simple Kriging, so called the simple Kriging variance σ_{SK}^2, associated with $\hat{Z}_0$ is obtained

$$\sigma_{SK}^2(x_0) = Cov\left[Z(x_0), Z(x_0)\right] - \sum_{i=1}^{n} \lambda_i Cov\left[Z(x_i), Z(x_0)\right] \tag{3-19}$$

The simple Kriging method requires the known mean value to calculate the covariance function to solve for the weights that minimize the variance of the estimation error. The mean of random function is usually not known in most practical situations. The ordinary Kriging provides the alternative way to find the minimum estimator of unknown constant mean by involving semivariogram which eliminates the requirement of mean value.

Rearranging the simple Kriging Eq. 13 as follows,

$$\hat{Z}_0 = \sum_{i=1}^{n} \lambda_i Z_i + m\left(1 - \sum_{i=1}^{n} \lambda_i\right) \tag{3-20}$$

It can be observed from this equation that the closer the sum of the weights is to 1, the smaller is the influence that the mean has in the estimation. If the simple Kriging weights sum to 1, the estimator is independent from the value of the mean. For the point estimation, we can estimate the value Z_0 at given location from n observations $Z_1, ..., Z_n$ as

$$\hat{Z}_0 = \sum_{i=1}^{n} \lambda_i Z_i + m\left(1 - \sum_{i=1}^{n} \lambda_i\right) \text{ with } \sum_{i=1}^{n} \lambda_i = 1 \tag{3-21}$$

Assuming the random function is second order stationary over the sampling domain, which implies that $E\left[Z(x)\right] = m$, it can be shown that

$$Cov\left[Z(x_i) - Z(x_0), Z(x_j) - Z(x_0)\right] = E\left[Z(x_i) - Z(x), Z(x_j) - Z(x)\right] \tag{3-22}$$

Following the same derivation as for simple Kriging, the variance of the ordinary Kriging is

$$\sigma_0^2 = Var\left[\hat{Z}(x_0) - Z(x_0)\right] = Var\left\{\sum_{i=1}^{n}[\lambda_i Z(x_i) - Z(x_0)]\right\}$$
$$= \sum_{i=1}^{n}\sum_{j=1}^{n}\lambda_i\lambda_j Cov\left[Z(x_i) - Z(x_0), Z(x_j) - Z(x_0)\right] \tag{3-23}$$

Restating the definition of semivariogram

$$\gamma(x_i - x_j) = \gamma(x_i - x) + \gamma(x_j - x) - Cov\left[Z(x_i) - Z(x_0), Z(x_j) - Z(x_0)\right] \tag{3-24}$$

Substitute the Eq. 24 into Eq. 23,

$$\sigma_0^2 = \sum_{i=1}^{n}\sum_{j=1}^{n}\lambda_i\lambda_j\left\{\gamma(x_i - x_0) + \gamma(x_j - x_0) - \gamma(x_i - x_j)\right\} \tag{3-25}$$

Expanding the equation using $\sum_{i=1}^{n}\lambda_i = 1$

$$\sigma_0^2 = 2\sum_{i=1}^{n}\lambda_i\gamma(x_i - x_0) - \sum_{i=1}^{n}\sum_{j=1}^{n}\lambda_i\lambda_j\gamma(x_i - x_j) \tag{3-26}$$

Finding the minimum of the mean square error in Eq. 26 is a constrained optimization problem with the restriction of the weights sum equal to 1. Lagrange method of multipliers allows the problem to be solved by reducing it to an unconstrained problem by means of a new objective function called the Lagrangian function (Hillier and Lieberman 1995) as follows

$$L(\lambda_i, \cdots, \lambda_n; \beta) = \sigma_0^2 + 2\beta\left(\sum_{i=1}^{n}\lambda_i - 1\right) \tag{3-27}$$

Here β is the Lagrangian multiplier. The system equations of ordinary Kriging can be formed as following,

$$\begin{aligned}&\sum_{i=1}^{n}\lambda_i\gamma(x_i,x_j)-\beta=\gamma(x_j,x_0)\quad j=1,2,\ldots,n\\&\sum_{i=1}^{n}\lambda_i=1\end{aligned}\tag{3-28}$$

and the minimum mean square error for ordinary Kriging σ_{OK}^2 is

$$\sigma(x_0)_{OK}^2=\sum_{i=1}^{n}\lambda_i\gamma(x_0,x_i)-\beta\tag{3-29}$$

Both Simple Kriging and ordinary Kriging require constant mean value of the random function, which are inadequate for the some geospatial data such as temperature in the upper part of the earth's crust and water depth near the shore. Universal Kriging fully removes the requirement of constant mean (Deutsch and Journel 1992) by the assumption that the mean of $Z(x)$ can be modeled as a linear combination of analytical functions. Usually the most common polynomial function has been used to model the mean:

$$m(x)=\sum_{l=0}^{k}a_l f_l(x),\ \text{ with }\ f_0(x)=1\tag{3-30}$$

From the estimator, we have

$$E(\hat{Z}_0)=E\left(\sum_{i=1}^{n}\lambda_i Z_i\right)=\sum_{i=1}^{n}\lambda_i E(Z_i)=\sum_{i=1}^{n}\sum_{l=0}^{k}a_l\lambda_i f_l(x_i)\tag{3-31}$$

For an unbiased estimator, that is $E\left(\hat{Z}_0-Z_0\right)=0$, we can show that

$$\sum_{i=1}^{n}\lambda_i f_l(x_i)=f_l(x_0),\quad \text{for } l=0,1,\ldots,k\tag{3-32}$$

Notice that the constraint $\sum_{i=1}^{n} \lambda_i = 1$ is included in the set of unbiased constraints for $l = 0$. Introducing the residual function $Y(x)$ which represents the difference of the random function $Z(x)$ and its expected value

$$Y(x) = Z(x) - E\left[Z(x)\right] \tag{3-33}$$

let $Cov_Y(x_i, x_j)$ the covariance of its residuals, we can find that the estimation variance σ_0^2 is equal to

$$\begin{aligned}\sigma_0^2 &= Var(\hat{Z}_0 - Z_0) = Var\left(\sum_{i=1}^{n} \lambda_i Z_i - Z_0\right) = Var\left[\sum_{i=1}^{n} \lambda_i (Y_i - Y_0)\right] \\ &= \sum_{i=1}^{n}\sum_{j=1}^{n} \lambda_i \lambda_j Cov(Y_i - Y_0, Y_j - Y_0)\end{aligned} \tag{3-34}$$

which can be represented as

$$\sigma_0^2 = \sum_{i=1}^{n}\sum_{j=1}^{n} \lambda_i \lambda_j \left\{\gamma_Y(x_i - x_0) + \gamma_Y(x_j - x_0) - \gamma_Y(x_i - x_j)\right\} \tag{3-35}$$

Expanding the equation using $\sum_{i=1}^{n} \lambda_i = 1$

$$\sigma_0^2 = 2\sum_{i=1}^{n} \lambda_i \gamma_Y(x_i - x_0) - \sum_{i=1}^{n}\sum_{j=1}^{n} \lambda_i \lambda_j \gamma_Y(x_i - x_j) \tag{3-36}$$

Finding the optimum weights for this estimator can be done employing the Lagrange method of multipliers for minimizing the estimation variance subject to the constraint of unbiased estimator. The Lagrangian function for universal Kriging is

$$L(\lambda_1, \ldots, \lambda_n; \beta_l) = \sigma_0^2 + 2\beta_0\left(\sum_{i=1}^{n} \lambda_i - 1\right) + 2\sum_{l=1}^{k} \beta_l \left(\sum_{i=1}^{n} \lambda_i f_l(x_i) - f_l(x_0)\right) \tag{3-37}$$

The system equations of universal kriging can be found as following,

$$\begin{aligned}
&\sum_{i=1}^{n}\lambda_i\gamma_Y(x_i,x_j)-\beta_0-\sum_{l=1}^{k}\beta_l f_l(x_j)=\gamma_Y(x_j,x_0) \quad j=1,2,\ldots,n\\
&\sum_{i=1}^{n}\lambda_i=1\\
&\sum_{i=1}^{n}\lambda_i f_l(x_i)=f_l(x_0) \quad l=1,2,\ldots,k
\end{aligned} \tag{3-38}$$

and the minimum mean square error for universal kriging σ_{UK}^2 is

$$\sigma_{UK}^2=\sum_{i=1}^{n}\lambda_i\gamma_Y(x_0,x_i)-\beta_0-\sum_{l=1}^{k}\beta_l f_l(x_0) \tag{3-39}$$

3.4 Uncertainties in ground deformation prediction

As any data sets, the data sets required to predict liquefaction-induced ground deformation contain systematic and nonsystematic (random) errors on topographic information and underground soil conditions. Systematic errors originate from the operations, equipment and recording procedures in field measurements; they can be reduced with accurate calibration of equipment, adequate training of operators and careful documentation. In some cases, it can even be corrected if data acquisition and processing are properly documented. In contrast to systematic errors, random errors are unpredictable and unavoidable. The present study deals with data sets that are assumed free from systematic error and focuses on the study of random errors.

The uncertainties in predicting ground deformations with Eq. 1 originate mainly from two types of error, i.e., (1) inaccurate determination of model variables, and (2) limitations inherent to the ground deformation model. In other words, uncertainties originate from the model itself, and the evaluation of model parameters.

3.4.1 Uncertainties generated from spatial modeling of *S* and T_L

Using statistical methods, the methodology examines the random errors attached to two model parameters, i.e., *S* and T_L, which are likely to generate the largest modeling errors. Other sources of errors are not included hereafter.

Slope information in the field is derived from elevation data obtained from ground survey or digital elevation model. The present analysis assesses the combined errors of spatial interpolation and model parameters using the minimum error variance. In the case of ordinary Kriging, the estimated interpolation error at location x_0 is the standard deviation of the error estimate:

$$\sigma_{OK}^2(x_0) = \sum_{i=1}^{n} \lambda_i \gamma(x_0 - x_i) - \beta \qquad (3\text{-}40)$$

where n, x_i, λ_i and β are defined in Eqs. 9 and 10.

3.4.2 Uncertainties of distance R induced from fault segment variation

The value of R, which is calculated using Eq. 2, depends on the position of the fault segment **AB**, i.e., point *A* and *B*. The position of point *M* is assumed to be well known compared to the position of points *A* and *B*, which define a fault segment. The uncertainties on the coordinates of points *A*, *B* and *M* are:

$$\Delta x_A = \Delta x_B = \Delta y_A = \Delta y_B = \Delta x \text{ and } \Delta x_M = \Delta y_M \approx 0 \qquad (3\text{-}41)$$

where Δx is the uncertainties on fault coordinates. The variance of *R* is approximated:

$$Var(R) \approx \left(\left(\frac{\partial R}{\partial x_A} \right)^2 + \left(\frac{\partial R}{\partial x_B} \right)^2 + \left(\frac{\partial R}{\partial y_A} \right)^2 + \left(\frac{\partial R}{\partial y_B} \right)^2 \right) \Delta x^2 \qquad (3\text{-}42)$$

with the derivatives of R

$$\begin{aligned} \frac{\partial R}{\partial x_A} &= \frac{y_B - y}{AB} + \frac{(x_B - x_A)R}{AB^2} & \frac{\partial R}{\partial x_B} &= \frac{y - y_A}{AB} - \frac{(x_B - x_A)R}{AB^2} \\ \frac{\partial R}{\partial y_A} &= \frac{x - x_B}{AB} + \frac{(y_B - y_A)R}{AB^2} & \frac{\partial R}{\partial y_B} &= \frac{x_A - x}{AB} - \frac{(y_B - y_A)R}{AB^2} \end{aligned} \qquad (3\text{-}43)$$

The variance of distance R can be simplified as:

$$Var(R) \approx \frac{\Delta x^2}{AB^2} \left(MA^2 + MB^2 + 2R^2 + \frac{2R}{AB} \mathbf{AB} \times (\mathbf{MA} + \mathbf{MB}) \right) \qquad (3\text{-}44)$$

When the project of point M is outside of of segment AB, point to point distance equation should be used to evaluate the variance of distance, Eq. 44 becomes:

$$Var(R) \approx \Delta x^2 \qquad (3\text{-}45)$$

3.4.3 Uncertainties of predicted ground deformation from MLR model

To access the uncertainty of predicted ground deformation, we introduce the variable $D^{'} = \log_{10}(D + 0.01)$. The MLR model (Eq. 1) is reformed as follows:

$$\hat{D}^{'} = b_0 + b_1 X_1 + \ldots + b_p X_p \qquad (3\text{-}46)$$

where b_0, …, b_p are constant coefficients, X_1 ,…, X_p are the model variables and p the total number of model variables. In the particular case of Eq. 1, p = 5 and the coefficients b_i and variables X_i are:

$$\begin{gathered} b_0 = -6.815, b_1 = 1.017, b_2 = -0.278, b_3 = -0.026, b_4 = 0.454, b_5 = 0.558 \\ X_1 = M_w, \quad X_2 = Log_{10}R, \quad X_3 = R, \quad X_4 = Log_{10}S, \quad X_5 = Log_{10}T_L \end{gathered} \tag{3-47}$$

The variance of $\hat{D}'$ can be written as follows:

$$Var(D') = s^2 \mathbf{X}_0^T \mathbf{C} \mathbf{X}_0 + b_1^2 Var(X_1) + \ldots + b_p^2 Var(X_p) \tag{3-48}$$

where $\mathbf{X}_0^T = (1 \quad X_1 \quad X_2 \quad \ldots \quad X_p)$ is the components vector of model variables, and s^2 is the residual mean square:

$$s^2 = \frac{1}{n-p-1} \sum_{i=1}^{n} \left(\hat{D}_i' - D_i' \right)^2 \tag{3-49}$$

In Eq. 49, D_i' is the ith observed value of D', and $\hat{D}_i'$ is ith predicted value corresponding to D_i' (i = 1,…,n). The value of s^2 is 0.084 and that of the covariance matrix **C** is (Bardet et al. 2002):

$$\mathbf{C} = 10^{-3} \times \begin{pmatrix} 0.46 & 0.14 & 0.00 & 0.08 & -0.03 & -0.40 & 0.02 & 0.01 \\ & 46.52 & -0.77 & -0.25 & 0.13 & -39.92 & -11.30 & -5.13 \\ & & 0.60 & -2.25 & 0.00 & -0.39 & 0.63 & -1.19 \\ & & & 24.74 & -0.53 & 6.07 & -2.71 & -5.63 \\ & & & & 0.03 & -0.18 & 0.06 & 0.11 \\ & \mathit{Symmetric} & & & & 46.84 & 0.04 & -0.16 \\ & & & & & & 44.29 & 10.62 \\ & & & & & & & 22.33 \end{pmatrix}$$

Equation 48 implies that the variance of D' is the sum of variance originating from independent terms. In theory, Eq. 48 seems useful for assessing the relative contribution of each term to the total variance on the predicted displacement D. However in practice, Eq. 48 is unfortunately nonlinear (including the logarithm terms of distance, slope and T$_L$) and requires some assumptions to introduce the standard deviations of physical meaningful variable, i.e., *D*. The variance and standard deviation of variables *D* and D' are assumed to be approximately related through:

$$\sigma^2(D) = Var(D) \approx \left(\frac{\partial \hat{D}}{\partial D'}\right)^2 Var(D') = 10^{2D'} Var(\hat{D}') \text{ and } \sigma(D) \approx D\sigma(D') \qquad (3\text{-}50)$$

The relative contribution of the model parameters (i.e., S and T_L) on D can be evaluated by assuming that the standard deviations of each model parameter are independent. The final variation of the predicted ground deformation can be determined by combining the uncertainties from R, S, T_L and model variation.

3.5 Case study in Port Island, Kobe

3.5.1 Study Area

In theory, the proposed methodology applies to all seismic regions within the world. Hereafter, it is illustrated in a particular case history in Port Island, Kobe, which took place during the 1995 Hyogoken-Nanbu, Japan earthquake. Port Island is a manmade island, the construction of which started in 1967 (Hamada and Wakamatsu, 1996b). The island is about 17 km far from the epicenter of the Hyogoken-Nanbu earthquake (As shown in Fig. 3), and about 7 km from the surface fault rupture (e.g., Wald 1996). The central part of the island contains schools, hospitals, high-rise residential buildings and hotels, and the ground surface in this area is elevated about 3-4 m higher than the surrounding area. A 1400m x 800m study area is selected for investigation as delineated in Figure 3 with a dashed line. The selected study area covers both improved and unimproved ground. It was selected about 200m far away from the waterfront to avoid interactions with the displacements of quaywalls (e.g., Hamada et al. 1996b).

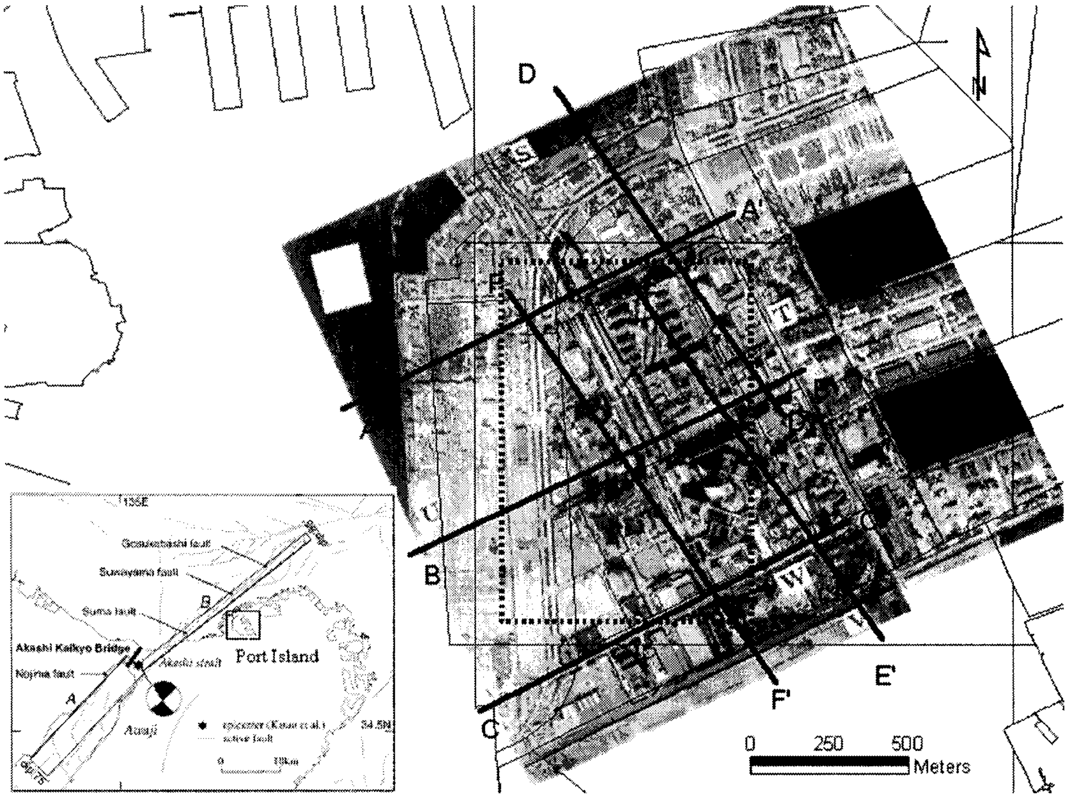

Figure 3-4. **Aerial photo of Port Island after 1995 Kobe earthquake showing study area (dotted line) and location of two-dimensional soil profiles across the study area.**

3.5.2 Available data set

The information required for predicting earthquake-induced ground deformation (i.e., ground water table, topography, and soil conditions) is available from

Jibankun, a geotechnical database which was created after the 1995 Kobe earthquake and includes about 5000 boreholes (Tanaka and Okimura 2001). During a collaborative research program between the University of Southern California and Kobe University, the geotechnical, topographic and displacement data were converted into a RDBMS-GIS platform (Bardet et al. 2002) as presented in Chapter 1. This database include compiled raw data, e.g., borehole logs, soil tests, SPT-N values, water table, ground elevations, ground displacements from the 1995 Kobe earthquake.

Figure 4 shows the location of borehole data in Port Island and the ground displacement vectors obtained using aerial photographs (Hamada et al. 1996a). The quaywalls in Port Island typically displaced 1-3 m toward the sea due to liquefaction. Near the center of the island, the ground displacements are not oriented toward the sea, which implies that the ground deformation relates not to the movement of quaywalls, but to sloping ground. This remark justifies the selection of the study area and the modeling of ground deformation using Eq. 1.

Figure 3-5. Displacement vector and borehole location in Port Island (data after Tanaka and Okimura, 2001).

Table 2 summarizes the available data in the study area. There are 330 displacement vectors, including 221 vectors on free ground; the other vectors are on non-ground locations, e.g., buildings and trees. SPT borehole data were obtained between 1970 and 1995. There are 69 boring tests available in the study area, 19 of which include information on the ground water elevation at the time of the field tests.

Table 3-2. Available information in study area in Port Island, Kobe.

Type	Quantity
Measured displacements (total)	330
Measured displacements (ground)	221
Elevation	221
SPT	69
Ground water table elevation	19

Figure 6 shows six two-dimensional soil profiles, which were constructed using SPT boreholes. These profiles are located in Fig. 4. Port Island is a reclaimed man-made island which has soil deposits made of three uniform layers. The upper 10 ~ 15 m thick layer is mostly made of artificial fill, and is underlain by a layer of clayey soil up to a depth of 30 m. The bottom layer is made of alternating sandy and clayey soils. The soil profiles of Fig. 6 are in good agreement with those independently obtained by Hamada et al. (1996a).

3.5.3 Regional parameter estimation

The study area was divided into grids with each size of 20m x 20m. The parameters M_w, R, S and T_L were determined at grid points. The earthquake magnitude M_w was set to 6.9 at all grid points. The distance R between grid points and earthquake source was calculated using the spatial positions of grid points and distance to fault rupture. The values of R vary between 6.4 and 7.4 km in the study area. The mean values of the model parameters S and T_L were determined using ordinary Kriging.

The ground elevation model in the study area is based on 221 elevation points. Figure 7 shows the directional semivariograms, which characterize the spatial variation of elevation data along six different directions. The zero direction corresponds to East-West in Fig. 4. The directional semivariograms are obtained for a lag interval of 30 m and a lag tolerance of 6 m. As shown in Fig. 7, the ground elevation is slightly anisotropic. The variograms of Fig. 7 were fitted using an exponential function with a nugget close to 0.6. This fitted semivariogram filters the high-frequency noise on measured elevations, which result from a 53-cm measurement error on elevation (Hamada et al. 1996a).

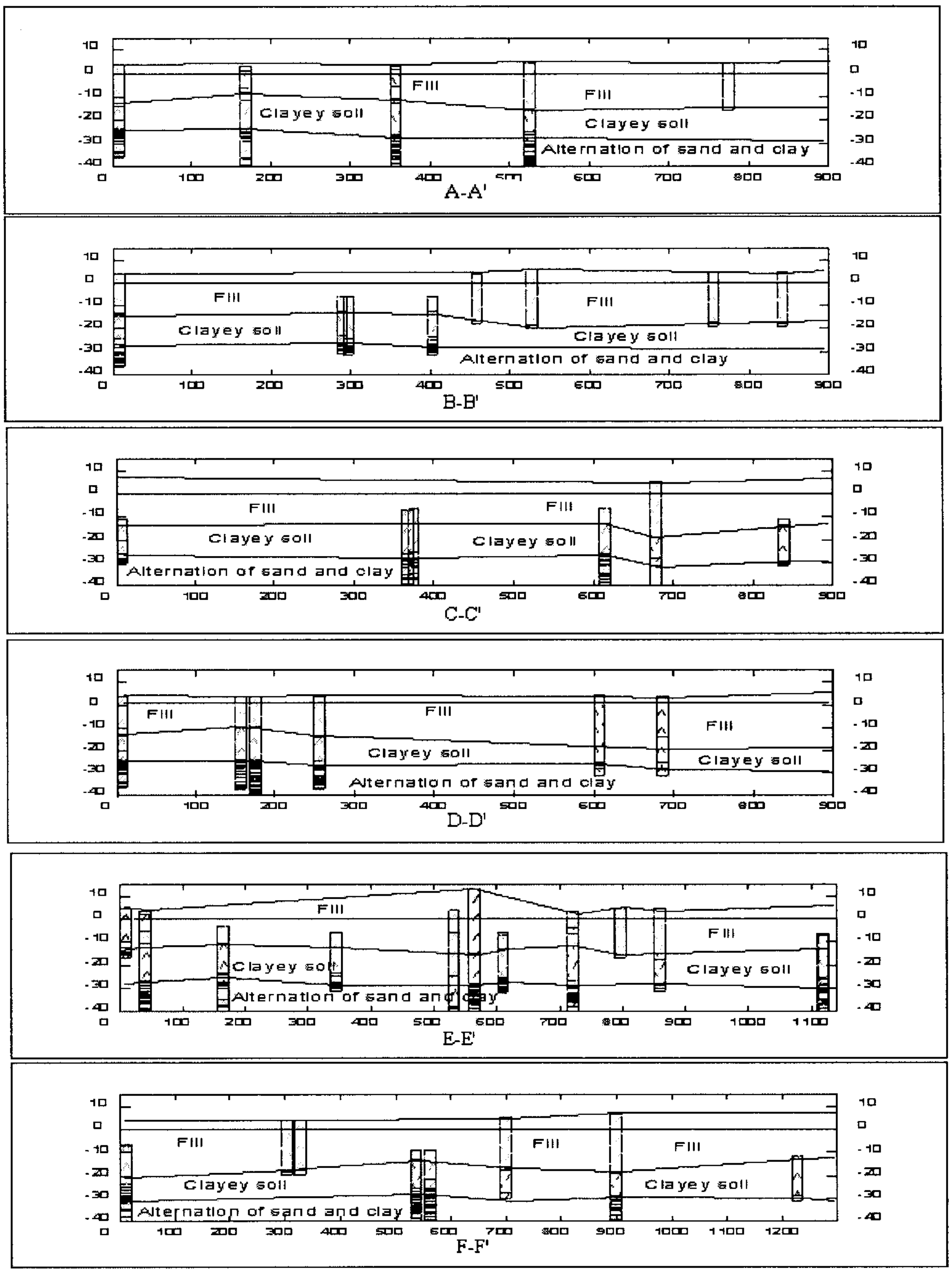

A-A'

B-B'

C-C'

D-D'

E-E'

F-F'

Figure 3-6. Two-dimensional soil profiles in Port Island along lines AA', BB', CC', DD' EE', and FF' of Fig. 3.

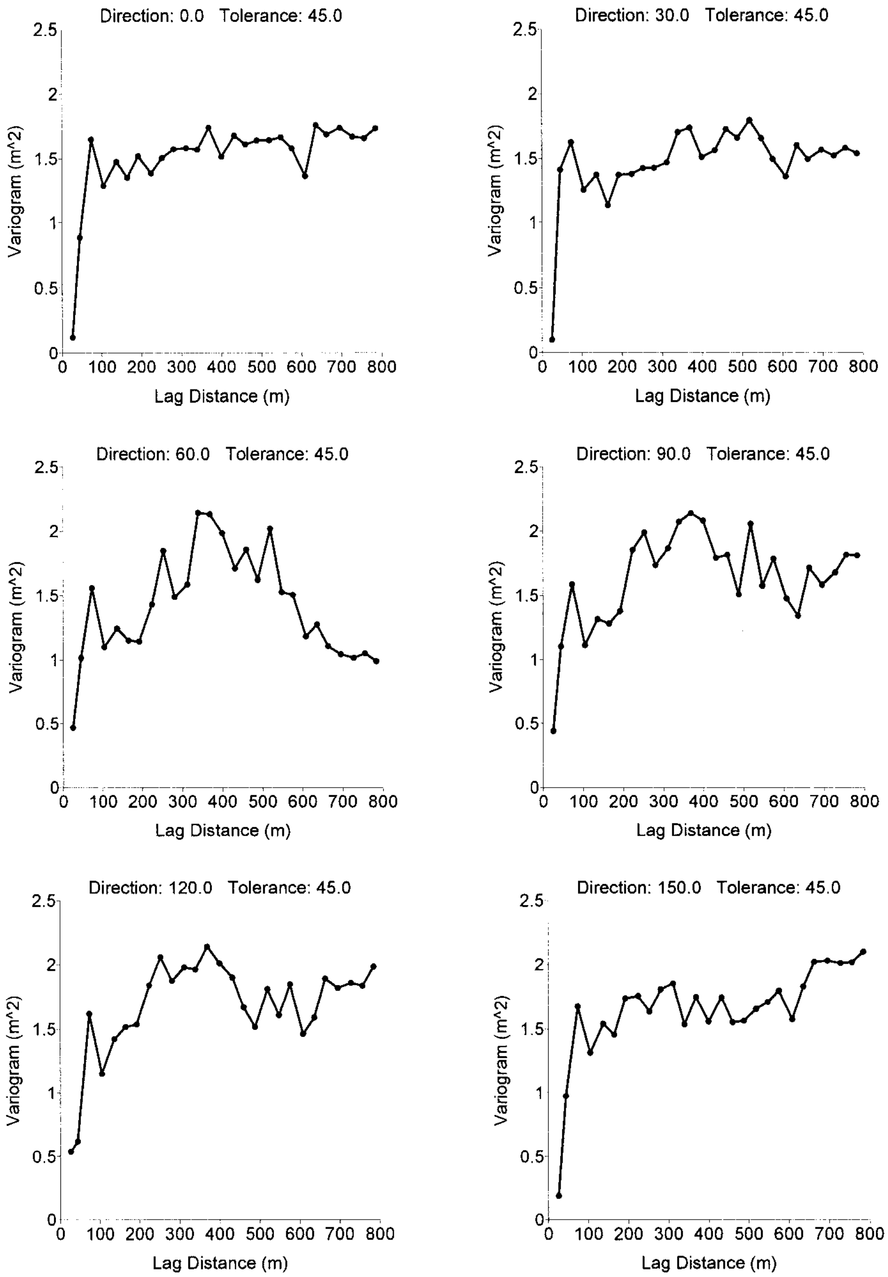

Figure 3-7. Directional semivariograms showing spatial continuity and anisotropy of elevation data.

Figure 8 shows the ground elevation generated using ordinary Kriging with and without filtering. Both IDW and Kriging without filtering produce typical "bulleyes," which are detectable in the concentration of contour lines around extreme values. As shown in Fig. 8c, the maps of filtered elevation are physically more meaningful. Figure 8d shows the standard deviation (Eq. 13) on elevation corresponding to Fig. 8c. Figure 9 displays the ground surface elevation using TIN (Triangulated Irregular Network). The eastern part of the study area has higher elevation than the western part. Covered with residential facilities, it has been elevated for various reasons including landscaping and drainage. The ground slope S in the study area was calculated from the elevation model of Fig. 8c using Eqs. 5 and 6. Figure 10a shows the map of ground slope, which ranges from 0.1% to 5%. The steeper slope values are observed in the eastern part of the study area.

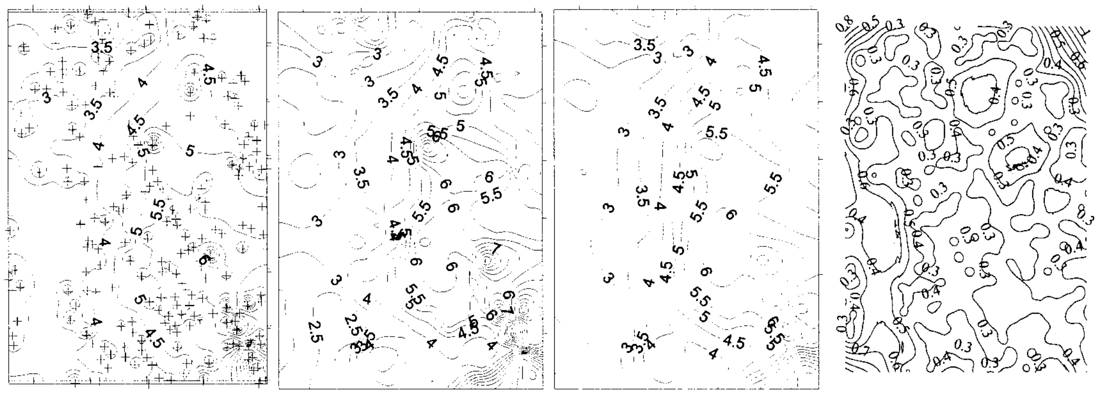

(a) (b) (c) (d)

Figure 3-8. Elevation models in study area (elevation in meter) using three spatial interpolation techniques: (a) IDW (α = 2); (b) Kriging without filtering; (c) Kriging with filtering; and (d) Standard deviation of elevation.

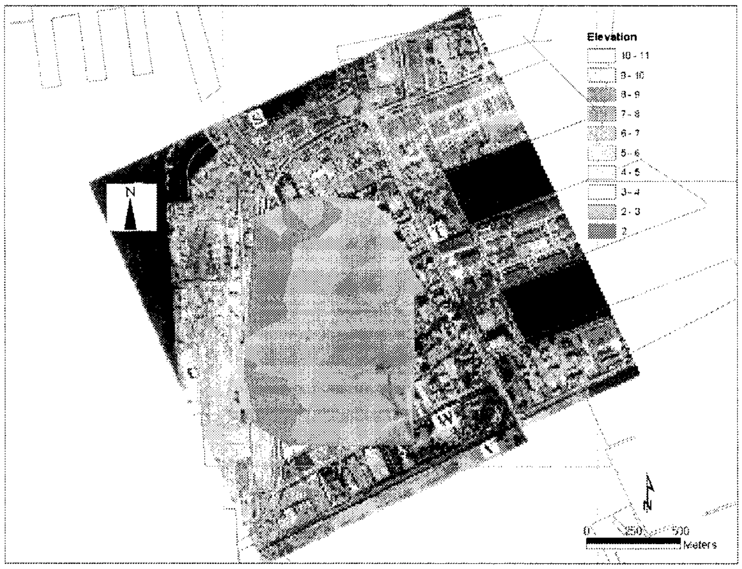

Figure 3-9. Elevation model in study area corresponding to Fig. 8c.

T_L depends on the soil properties and the elevation of the ground water table. The ground water table in Port Island varies with time and changes with the sea tide and rainfalls. There are only 19 boreholes recorded the water table information in the history, and its elevation could not be inferred from the information on water table from boreholes because these field tests were performed at various times between 1970 and 1995. In this analysis the constant ground water table at the sea level was assumed at the time of the 1995 Hyogoken-Nanbu earthquake. The effect of uncertainty of ground water table on displacement prediction will be reviewed in next section. The SPT blow counts were corrected following the procedure of Youd and Idriss (1997), which accounts for different rod energy ratio, hammer frequency and borehole diameter. SPT blow count N has to be normalized to an effective overburden pressure of 100 KPa and a hammer energy ratio of 60%. Additional correction factors need to be applied to obtain the corrected normalized $(N_1)_{60}$ as noted in Eq. 51:

$$(N_1)_{60} = N_m C_N C_E C_B C_R C_S \tag{3-51}$$

where N_m is the measured standard penetration resistance, C_N is the overburden pressure correction, C_E is the hammer energy ratio correction; C_B is the borehole diameter correction; C_R is the rod length correction; and C_S is the correction for samplers with or without liners. There is no detail information on the SPT testing, all the SPT has been assumed using standard sampler with diameter 100 mm. As recommended by Seed, et al. (1985), the energy ratio has been taken as 78% for Japanese hammer. The correction parameters are listed in Table 3.

Table 3-3. Correction parameters for $(N_1)_{60}$ calculation (*h* = depth).

Notation	Parameter	Value	
C_E	Hammer energy ratio	1.3	
C_B	Borehole diameter correction	1.	
C_B	Rod length correction	1.	
C_S	Samplers with or without liners	0.75	if $h \leq 4$ m
		0.85	if $4 \text{ m} < h \leq 6$ m
		0.95	if $6 \text{ m} < h \leq 10$ m
		1.0	if $h > 10$ m

After calculating the T_L value for each borehole location, the continuation distribution of the T_L values in selected study were interpolated using ordinary Kriging with filtering. As shown in Fig. 10b, the values of T_L in the study area range from 2 m to 14 m. The eastern part of the study area shows smaller liquefied thickness than the northwest part, which results from the ground improvement performed in this area before the 1995 Hyogoken-Nanbu earthquake (Hamada et al. 1996a).

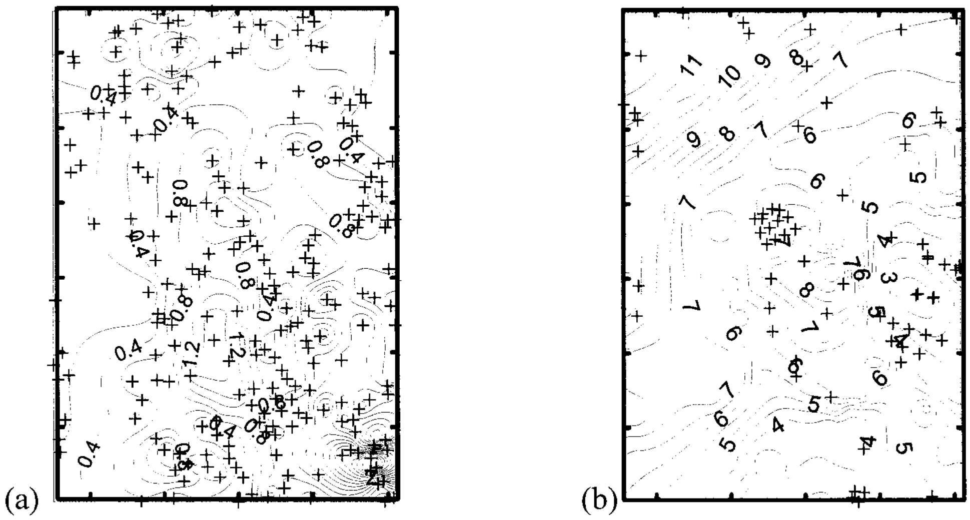

Figure 3-10. Values of model parameters interpolated using ordinary Kriging in study area: (a) slope S and (b) thickness T_L.

3.5.4 Predicted displacement

As shown in Figs. 11a and b, measured displacements vary rapidly over short distance, which results from the 33-cm errors in processing aerial photographs in the horizontal direction (Hamada et al. 1996a). The measurement errors were filtered out using the same Kriging technique as for elevation. The nugget was found to be about 276 cm^2, which corresponds to the errors in processing aerial photographs. As shown in Fig 11c, the filtered displacements are smoother than those obtained using IDW and Kriging without filtering.

Table 4 lists the range of the model parameters, which fall within the calibration ranges that are acceptable for the MLR model (i.e., Eq. 1). Figure 12 show the maps of measured displacement, predicted displacement and corresponding residual. As shown in Figs. 12a and 12b, predicted and measured displacements are in good agreement, provided that high-frequency noises are filtered out. Most residuals fall between –20 cm and 20 cm. Figure 13 give the plot of predicted displacement versus measured displacement, which are also in good agreement after filtering.

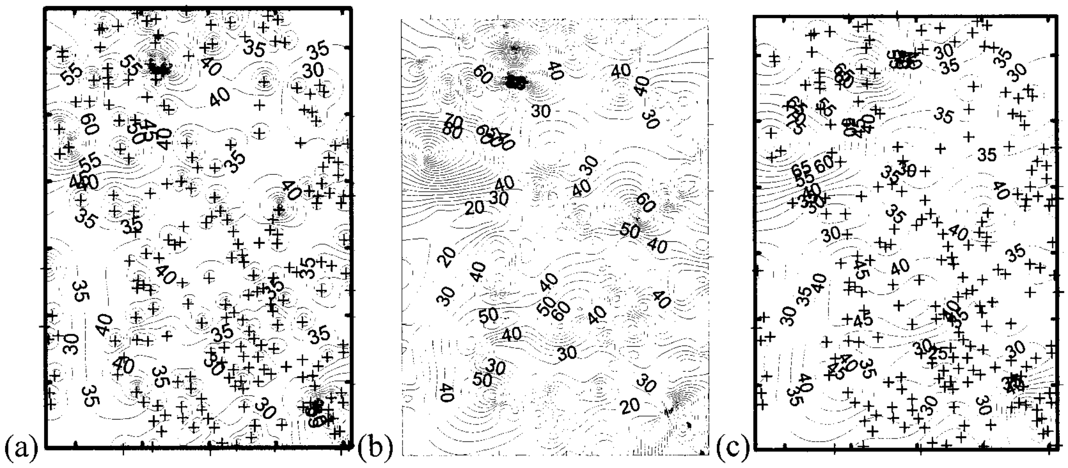

Figure 3-11. Maps of displacement amplitudes measured in study area (after Hamada et al., 1996) and interpolated using different techniques: (a) IDW (α=2); (b) Kriging without filtering; and (c) Kriging with filtering.

Table 3-4. Value range of MLR model parameters in study area.

Parameter	Study range	Calibration range
M_w	6.9	6.4-9.2
R	6.4 ~ 7.4	0.2-100
T_L	2 ~ 14	0.2-16.7
S	0.1 ~ 5	0.05-5.9

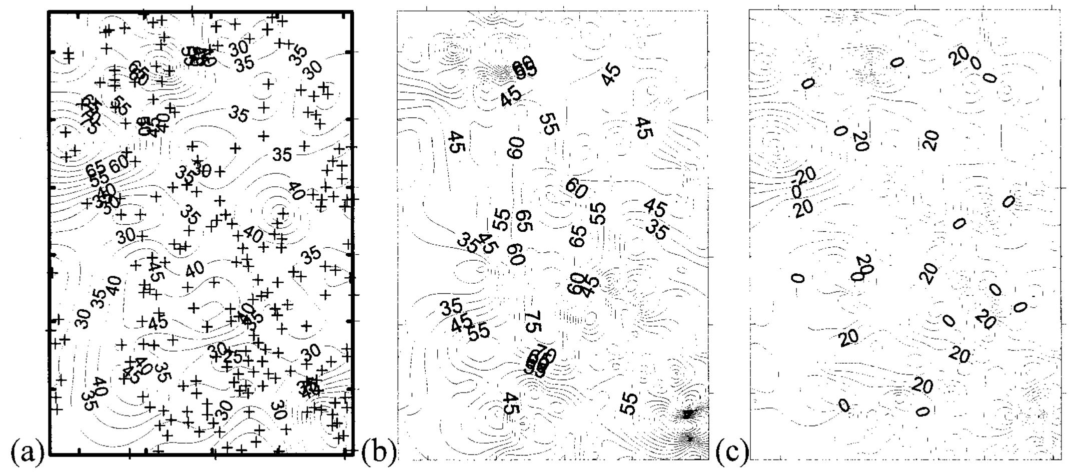

Figure 3-12. **Maps of measured and predicted displacements: (a) Measured and filtered (10- 100 cm); (b) Predicted (15- 110 cm); and (c) Residual (-60 – 40 cm.**

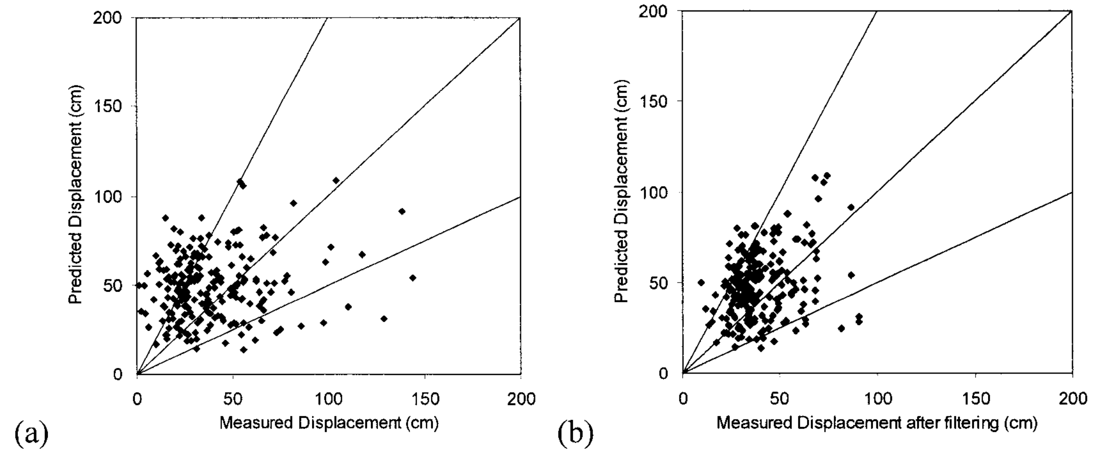

Figure 3-13. **Comparison of predicted displacement and measured displacement: (a) without filtering and (b) with filtering.**

3.6 Uncertainties on model parameters and predicted displacements

The proposed methodology, which was so far applied to predict mean values of liquefaction-induced ground deformation, can be used to examine model uncertainties and to assess possible deviations from predicted mean values. The present analysis assumes that the parameters S and T_L cause the largest uncertainties, and that M_w and R produce smaller uncertainties. The values of T_L depend on the ground water elevation and $N1_{60}$ profiles.

3.6.1 Uncertainties of water table elevation

As previously mentioned, the thickness T_L depends on the elevation of the water table. In Port Island, the water table elevation is influenced by the sea tide as the upper layer of artificial fills is pervious. Tide data in 1995 are available from the Japan Oceanographic Data Center (JODC 2003). Data include the sea level measured by the tide gauge located at the Kobe tide station operated by the Meteorological Agency of Japan. Figure 14 shows the time history of tide elevation in Port Island during a five days time window centered about the time of the earthquake, which is 5:46 AM local time on January 17, 1995. Data are recorded every hour, but are missing for about 10 hours after the earthquake because the tide station was offline due to the earthquake. Table 5 gives the mean value and standard deviation of tide elevation over one day. The average tide level is around 1.5 m with a 0.5 m standard deviation.

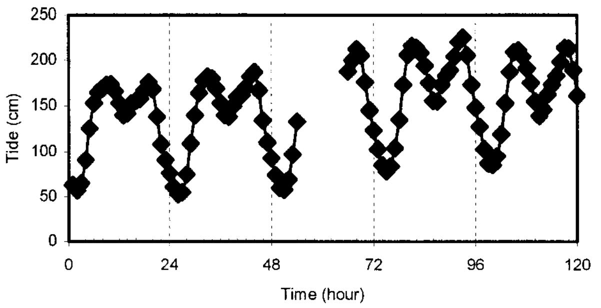

Figure 3-14. Tide data in Port Island between January 15, 1995 and January 19, 1995 (Time axis starts at 12:00am, January 15).

Table 3-5. Five days tide data statistics at Port Island.

Date	Maximum (cm)	Minimum (cm)	Mean (cm)	Standard Deviation (cm)	Count
15-Jan-95	176	57	134.5	39.6	24
16-Jan-95	187	53	138	42.9	24
17-Jan-95	212	58	133.8	58.3	13
18-Jan-95	225	78	166.9	46.5	24
19-Jan-95	214	85	161.7	41.4	24
5 days	225	53	148.3	46.23	109

3.6.2 Uncertainties on $N1_{60}$

There is no doubt that uncertainties on predicted ground deformation are influenced by T_L uncertainties, which in turn are influenced by $N1_{60}$ uncertainties. The uncertainties on the thickness T_L may become especially large for the soil profiles that have $N1_{60}$ values close to 15. However, the errors on $N1_{60}$ are complicated to evaluate in the present study due to a lack of information on the SPT test procedures between 1970 and 1995. For this reason, they are neglected hereafter.

3.6.3 Uncertainties of thickness T_L

Figure 15c shows the spatial distribution of the standard deviation of T_L, which is generated using ordinary Kriging for a well known water table elevation, i.e., z_w = 1.5 m. The maximum standard deviation of T_L, which results only from rapid changes in T_L (i.e., nugget effect), is about 1 m. Figure 15d shows the standard variation of T_L, which include additional uncertainties on the elevation z_w of the water table due to tide.

3.6.4 Uncertainties of distance R

As shown in Fig. 4, the fault model of the Hyogoken Nanbu (Koketsu et al. 1998) can be approximated using a segment, which has for coordinate uncertainty Δx = 0.67 km. Figure 15a shows the corresponding standard deviation of distance R, which was calculated using Eq. 44.

3.6.5 Uncertainties of ground slope

Figure 15b shows the spatial distribution of the standard deviation of ground slope S, which is generated by ordinary Kriging, i.e., Eq. 13. The standard deviation of S is about 0.01 – 0.5%.

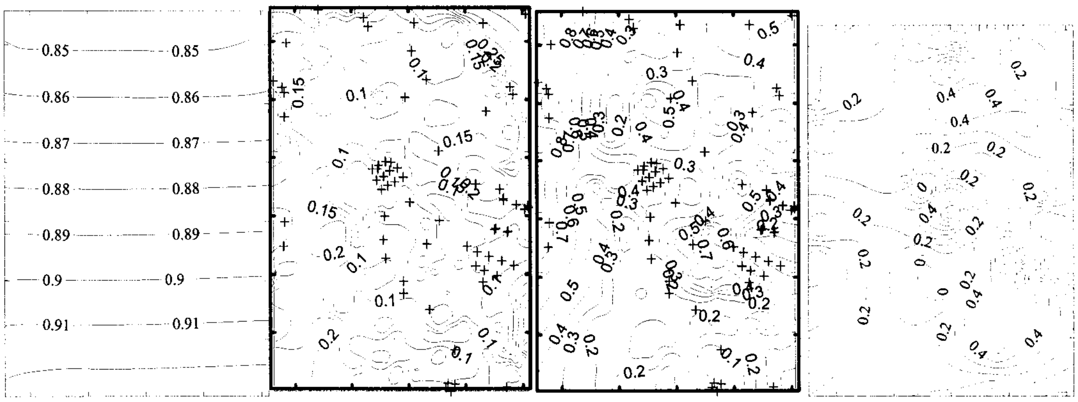

(a) (b) (c) (d)

Figure 3-15. Standard deviations for model parameters: (a) distance *R* (km); (b) Slope *S* (%); (c) T_L (m) with certain water table elevation; and (d) T_L (m) including uncertain water table elevation.

3.6.6 Uncertainties on predicted displacements

Assuming that the modeling errors can only originate from the MLR model calibration and from the model parameters *R*, *S* and T_L, the variance of $\hat{D}'$ (i.e., decimal logarithm of *D*) is approximated as follows:

$$Var(D') = s^2\mathbf{X}_0^T\mathbf{C}\mathbf{X}_0 + b_2^2Var(R) + b_3^2Var(Log_{10}R) + b_4^2Var(Log_{10}S) + b_5^2Var(Log_{10}T_L)$$

The first item in the right hand side of above equation indicates the variance of MLR model, and the other terms represent the variance originating from parameters R, *S* and T_L, respectively. The standard deviation of *D* can be approximated using Eq. 19. Figure 16a represents the standard deviation of D which is contributed from MLR model. Figures 16b shows the standard deviation of *D* which results solely from the errors on model parameters *R*, *S* and T_L as depicted in Figs. 15a and b. Figure 16c displays the standard deviation of *D* which include both the errors on *R*, *S* and T_L and the MLR modeling errors. As shown in Figs. 16, the model itself and the model parameters generate comparable errors for the predicted displacement. In view of the similarity of Figs. 15b and 16b, the slope *S* appears to control the predicted displacement errors.

Table 6 summarizes the maximum standard deviations on the values of *R*, T_L, *S* and predicted displacements. The predicted displacement error is about 70 cm because of uncertainty in *R*, T_L and *S*, and about 30 cm from the MLR model error. Overall the maximum predicted displacement error exceeds 75cm.

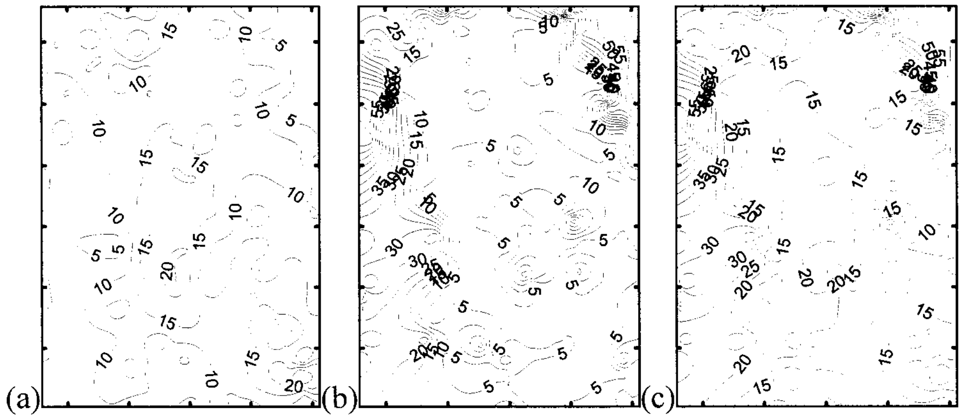

Figure 3-16. Standard deviations of predicted displacements resulting from MLR model error and model parameters: (a) MLR model only, (b) model parameters only; (c) model error and model parameters.

Table 3-6. Maximum standard deviations of model parameters and predicted displacements.

Model Parameter	Standard Deviation
Liquefied layer thickness (T_L) (m)	1
Slope S (%)	0.5
Water table elevation (m)	0.5
Normalized blow count $N1_{60}$	
Distance to seismic source (km)	
Displacement resulting from R, S and T_L (cm)	70
Displacement resulting from MLR model (cm)	30
Displacement (cm)	75

3.7 Discussion

The analysis of model uncertainties was focused on the soil parameters, and the topography in a particular case study located in Japan. More research is needed to examine the effects of other parameters, e.g., depth of water table, SPT blow counts, distance to epicenter, moment magnitude, and heterogeneous soil deposits. The present case study in Port Island only requires the use of ordinary Kriging with slight directional anisotropy. The soil deposits in Port Island were rather uniform, which simplified the generation of model parameters in the study area. The analysis of more complicated soil deposits and topography may required more advanced Kriging techniques, e.g., drift filtering, universal Krigging, Kriging across discontinuities (e.g., Chiles and Delfiner 1999). The proposed method predicted ground displacement based on an empirical MLR model. Modeling advances are likely to originate from models that are more rooted in mechanics and physics.

3.8 Conclusion

A methodology for predicting liquefaction-induced ground deformation over large areas has been presented and illustrated using a case study in Port Island after the 1995 Hyogoken-Nanbu earthquake. The methodology relies upon the ground-deformation model of Bardet et al. (2002), geotechnical database, geostatistics and geographic information system (GIS). The prediction of liquefaction-induced ground deformation over large regions requires data on soil boreholes, high resolution topography and ground water surface elevation. Geostatistics and GIS are combined to generate the model parameters over extended areas, and to examine the standard deviations of model parameters and results. The comparison of predicted and observed results shows that the methodology is capable of predicting the ground deformation observed in 1995, even though the ground de-formation model was calibrated from earthquake case histories prior to 1994. The proposed methodology is intended for the microzonation of liquefaction hazards worldwide.

4 LARGE DEFORMATION THEORY FOR MATERIAL AND GEOMETRIC NONLINEARITY

4.1 Introduction

Several meters of deformation at deformed embankment or dam have been estimated (Finn 2000) using the advances in effective stress model (e.g. Martin et al. 1975, Ishihara and Towhata 1980) and nonlinear numerical approaches (Finn et al. 1986, Prevost 1995, Bardet 1986, Iai et al. 1992). These types of approach use the small strain theory to compute the possible large deformation induced from liquefaction or flow failure. The use of classical infinitesimal elasto-plastic constitutive models in the solution of problems involving large deformation, i.e. liquefaction-induced ground deformation as large as several meters, is not appropriate, since a linear strain measure is invalid for large deformation (Simo and Hughes 1998).

On the other hand, the initial stress caused by gravity force plays an important role in the liquefaction-induced deformation. A small strain formulation can not taken consideration of configuration change of the system, therefore it is incompetent to reflect the fact that the gravity-induced shear stress decreases with the development of deformation.

It is therefore important that a numerical procedure developed to solve liquefaction induced large deformation problems has the capability to consider the material and geometrical nonlinearity. , or so called finite deformation/finite strain elasto-plastic constitutive material model. Two different approaches to the solution of finite strain plasticity problems have arisen in the literature (Simo and Pister 1984, Nagtegaal and Jong 1982, Simo and Hughes 1998). The first algorithm lies in the fact that the elastic response is formulated by a hypoelastic constitutive equation. It relates an objective rate of the stress tensor, $\dot{\boldsymbol{\tau}}$ to the rate of deformation tensor $\dot{\mathbf{d}}$, through a spatial rate constitutive equation, i.e.

$$\dot{\boldsymbol{\tau}} = \mathbf{a} : \dot{\mathbf{d}} \tag{4-1}$$

where an additive decomposition of the deformation rate tensor, $\dot{\mathbf{d}}$ is then introduced. Different objective stress rates including Jaumann rate, Green-McInnis-Naghdi rate and Trusdell rate have been used to finite strain plasticity problems (Oldroyd 1950, Truesdell 1955, Green and Naghdi 1965, Green and McInnis 1967). This class of model is currently widely used in large-scale inelastic calculations (e.g., Key 1974, Key et al. 1981).

The second approach to the solution of finite deformation elasto-plasticity problem is based on hyperelastic stress-strain relations and on the multiplicative decomposition of the deformation gradient $\mathbf{F}$ into its elastic and plastic parts, i.e.

$$\mathbf{F} = \mathbf{F}^{e}\mathbf{F}^{p} \tag{4-2}$$

The multiplicative split of $\mathbf{F}$ was first introduced by Lee and Liu (1967), and quickly accepted by many researchers to be used for the solution of finite strain elasto-plasticity problems in finite element analysis (Simo et al. 1985, Kim and Oden 1985, Simo and Taylor 1991).

The current research work is based on the hypoelastic rate model which are widely used in numerical analysis for rock and soil material which exhibit strong nonlinear behavior. This chapter will review the basic concepts of continuum mechanics (Simo and Hughes 1998) which help to understand the effect of large deformation in liquefaction-induced ground deformation analysis. The first section gives the description of deformation and motion. The second section presents a general concept of strain and strain rate measurement in nonlinear continuum mechanics. The third section reviews different measurements of stress and objective stress rates which are commonly used in large deformation computation. The hypoelastic constitutive equation based on several objective stress rates has been investigated in the fourth section. The performance of different objective stress rate under large rotation has been demonstrated using a simple shear problem. The fifth section describes the theory of finite strain elasto-plasticity based on additive theory and the steps of rotation vector calculation for Green-McInnis rate and Jaumann rate. The general procedure for finite strain elasto-plasticity model has been summarized.

4.2 Deformation

As shown in Fig. 1, the material body occupies the initial (reference) configuration Ω_0 at time $t = 0$. At time $t > 0$, the body has moved and occupies a different or deformed configuration Ω_t. In a fixed reference frame with Cartesian coordinates, the kinematics of the body is defined by the following quantities:

$\mathbf{X}$, i.e., X_i initial position of a material point at time $t = 0$

$\mathbf{x}(\mathbf{X}, t)$, i.e., x_i	position of point **X** at time *t*
$\mathbf{u}(\mathbf{X}, t)$, i.e., u_i	displacement of point **X** at time *t*

where the subscript *i* is 1, 2 and 3. The initial and present positions of a particle at time *t* are related to its displacement through:

$$\mathbf{x} = \mathbf{X} + \mathbf{u}(\mathbf{X}, t) \ \text{ i.e., } \ x_i = X_i + u_i \qquad (4\text{-}3)$$

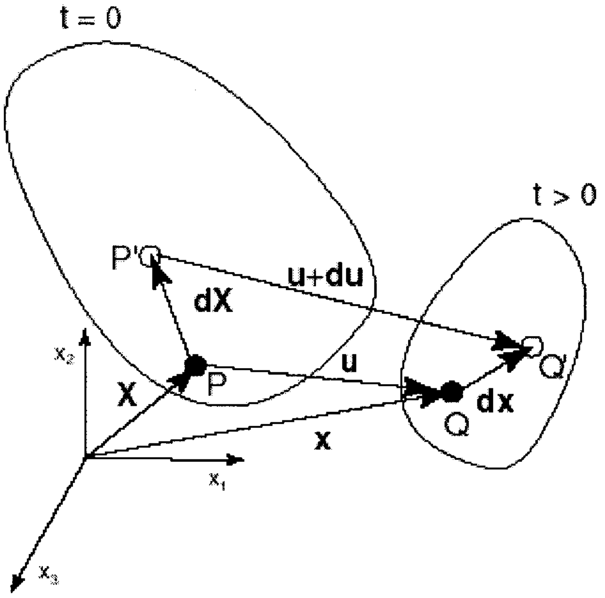

Figure 4-1. Initial and deformed configurations of a material body.

The deformation in the neighborhood of a particle **X** at time *t* is characterized by the deformation gradient **F**:

$$\mathbf{dx} = \mathbf{F}\mathbf{dX} \ \text{ i.e., } \ dx_i = F_{ij}dX_j \ \text{ implied sum on } j = 1,2,3 \qquad (4\text{-}4)$$

where **X**+**dX** and **x**+**dx** are the positions at times $t = 0$ and $t > 0$, respectively, of the particle **X**+**dX**, which is a neighbor of the particle **X**. **F** has been defined:

$$\mathbf{F} = \frac{\partial \mathbf{x}}{\partial \mathbf{X}} = \frac{\partial(\mathbf{X}+\mathbf{u})}{\partial \mathbf{X}} = \boldsymbol{\delta} + \frac{\partial \mathbf{u}}{\partial \mathbf{X}} \tag{4-5}$$

Express the deformation gradient in the index format with the configuration and displacement, we have

$$F_{ij} = \frac{\partial x_i}{\partial X_j} = \frac{\partial(X_i+u_i)}{\partial X_j} = \delta_{ij} + \frac{\partial u_i}{\partial X_j} \tag{4-6}$$

where δ_{ij} is the Kroneker symbol

$$\delta_{ij} = \begin{cases} 1 & \text{if } i=j \\ 0 & \text{if } i \neq j \end{cases} \tag{4-7}$$

The deformation gradient **F** can be decomposed as follows (Gurtin 1981):

$$\mathbf{F} = \mathbf{RU} = \mathbf{VR} \tag{4-8}$$

This is called the polar decomposition. **R** is the rotation tensor which is orthogonal. **U** and **V** are symmetric and positive definite, and are called the right and left stretch tensors (i.e., $\mathbf{U}^{\mathrm{T}} = \mathbf{U}$ and $\mathbf{V}^{\mathrm{T}} = \mathbf{V}$), respectively.

The determinant of $\mathbf{F}$ is denoted by J and called the Jacobian determinant:

$$J = \det(\mathbf{F}) \tag{4-9}$$

The surface **dA** in the initial configuration is related to the surface **da** in the present configuration as follows:

$$\mathbf{da} = \det(\mathbf{F})\left(\mathbf{F}^{-1}\right)^{T} \mathbf{dA} \quad \text{or} \quad \mathbf{dA} = \frac{1}{\det(\mathbf{F})} \mathbf{da} \cdot \mathbf{F} \tag{4-10}$$

The volume $d\Omega_0$ in the initial configuration is related to the volume $d\Omega_t$ in the present configuration as follows:

$$\frac{d\Omega_t}{d\Omega_0} = J = \det[\mathbf{F}] \tag{4-11}$$

4.3 Strains and Strain rates

In contrast to linear elasticity, many different measures of strain and strain rate are used in nonlinear continuums mechanics. A strain measure must vanish for any rigid body motion, and in particular for rigid body rotation. This is the crucial reason why that the linear strain definition cannot be used in large deformation nonlinear analysis since it produces nonzero strain during pure rotation.

4.3.1 Strain measurements

From the deformation gradient $\mathbf{F}$, we can define the right Cauchy-Green tensor as:

$$\mathbf{C} = \mathbf{F}^T\mathbf{F} \text{ or } C_{ij} = F_{ik}^T F_{kj} = F_{ki}F_{kj} = \frac{\partial x_k}{\partial X_i}\frac{\partial x_k}{\partial X_j} \tag{4-12}$$

and the left Cauchy-Green tensor $\mathbf{B}$ is:

$$\mathbf{B}^{-1} = \left(\mathbf{F}^{-1}\right)^T \mathbf{F}^{-1} \text{ or } B_{ij}^{-1} = \left(F_{ik}^{-1}\right)^T F_{kj}^{-1} = F_{ki}^{-1}F_{kj}^{-1} = \frac{\partial X_k}{\partial x_i}\frac{\partial X_k}{\partial x_j} \tag{4-13}$$

Eq. 12 and Eq. 13 lead to the definition of Lagrangian strain tensor $\mathbf{E}$:

$$\mathbf{E} = \frac{1}{2}(\mathbf{C} - \mathbf{I}) \quad \text{and} \quad E_{ij} = \frac{1}{2}\left(\frac{\partial x_k}{\partial X_i}\frac{\partial x_k}{\partial X_j} - \delta_{ij}\right) \tag{4-14}$$

and Eulerian strain tensor $\mathbf{e}$:

$$\mathbf{e} = \frac{1}{2}\left(\mathbf{I} - \mathbf{B}^{-1}\right) \quad \text{and} \quad e_{ij} = \frac{1}{2}\left(\delta_{ij} - \frac{\partial X_k}{\partial x_i}\frac{\partial X_k}{\partial x_j}\right) \tag{4-15}$$

In terms of displacements, **E** and **e** can be presented:

$$E_{ij} = \frac{1}{2}\left(\frac{\partial u_i}{\partial X_j} + \frac{\partial u_j}{\partial X_i} + \frac{\partial u_k}{\partial X_i}\frac{\partial u_k}{\partial X_j}\right) \quad \text{and} \quad e_{ij} = \frac{1}{2}\left(\frac{\partial u_i}{\partial x_j} + \frac{\partial u_j}{\partial x_i} - \frac{\partial u_k}{\partial x_i}\frac{\partial u_k}{\partial x_j}\right) \tag{4-16}$$

In the case of rigid body rotation, **F** is orthogonal, i.e., $\mathbf{F}^{-1} = \mathbf{F}^{T}$, and the tensors **C** and **B** becomes:

$$\mathbf{C} = \mathbf{F}^{T}\mathbf{F} = \mathbf{F}^{-1}\mathbf{F} = \mathbf{I} \quad \text{and} \quad \mathbf{B}^{-1} = \left(\mathbf{F}^{-1}\right)^{T}\mathbf{F}^{-1} = \left(\mathbf{F}^{T}\right)^{T}\mathbf{F}^{-1} = \mathbf{F}\mathbf{F}^{-1} = \mathbf{I} \tag{4-17}$$

which shows that **E** and **e** vanish in rigid body rotation and suitable for geometrically nonlinear theory.

For small deformation gradients (i.e., $\partial u_i / \partial X_j << 1$), both **E** and **e** becomes the infinitesimal strain tensor ε:

$$\varepsilon_{ij} = \frac{1}{2}\left(\frac{\partial u_i}{\partial x_j} + \frac{\partial u_j}{\partial x_i}\right) \tag{4-18}$$

4.3.2 Rate of deformation

In contrast to Green strain tensors, the rate of deformation **D** is also a very important kinematics measure for finite strain theory. Looking at the current configuration in Figure 1, the velocity **v**(**X**, *t*) of the particle **X** at time *t* (the particle **X** is at position **x** at time *t*) with Cartesian components v_i is related to its displacement

$$\mathbf{v} = \left.\frac{\partial \mathbf{x}}{\partial t}\right|_{\mathbf{X}} \quad \text{i.e., } v_i = \left.\frac{\partial x_i}{\partial t}\right|_{X_k} \tag{4-19}$$

The distribution of velocity about the position **x** at time *t* is defined by the velocity gradient **L**:

$$\mathbf{dv} = \mathbf{L}\,\mathbf{dx} \quad \text{i.e., } dv_i = L_{ij} dx_j \tag{4-20}$$

where **dv** is the relative velocity at time *t* of the particle **X**+**dX** with respect to the particle **X** (the particles **X** and **X**+**dX** are at position **x** and **x**+**dx** at time *t*). **L** has for Cartesian components:

$$\mathbf{L} = \left.\frac{\partial \mathbf{v}}{\partial \mathbf{x}}\right|_{\mathbf{X}} \quad \text{i.e., } L_{ij} = \frac{\partial v_i}{\partial x_j} = v_{i,j} \tag{4-21}$$

L can be decomposed into a symmetric and skew-symmetric part by

$$\mathbf{L} = \frac{1}{2}\left(\mathbf{L} + \mathbf{L}^T\right) + \frac{1}{2}\left(\mathbf{L} - \mathbf{L}^T\right) \tag{4-22}$$

The rate of deformation **D**, symmetric part of **L**, has for components:

$$\mathbf{D} = \frac{1}{2}\left(\mathbf{L} + \mathbf{L}^T\right) \quad \text{i.e., } d_{ij} = \frac{1}{2}\left(L_{ij} + L_{ji}\right) = \frac{1}{2}\left(v_{i,j} + v_{j,i}\right) = v_{(i,j)} \tag{4-23}$$

and **W** the spin tensor, skew symmetric part of **L**, has for components:

$$\mathbf{W} = \frac{1}{2}\left(\mathbf{L} - \mathbf{L}^T\right) \quad \text{i.e., } \omega_{ij} = \frac{1}{2}\left(L_{ij} - L_{ji}\right) = \frac{1}{2}\left(v_{i,j} - v_{j,i}\right) = v_{[i,j]} \tag{4-24}$$

The velocity gradient and the deformation gradient **F** are related through:

$$\mathbf{L} = \dot{\mathbf{F}}\,\mathbf{F}^{-1} \tag{4-25}$$

The time derivative of right Cauchy-Green strain can be evaluated using Eq. 25

$$\dot{\mathbf{C}} = \dot{\mathbf{F}}^T \cdot \mathbf{F} + \mathbf{F}^T \cdot \dot{\mathbf{F}} = \mathbf{F}^T \cdot (\mathbf{L}^T + \mathbf{L}) \cdot \mathbf{F} \tag{4-26}$$

which gives

$$\dot{\mathbf{C}} = 2\mathbf{F}^T \cdot \mathbf{D} \cdot \mathbf{F}\text{, or } \mathbf{D} = \frac{1}{2}\mathbf{F}^{-T} \cdot \dot{\mathbf{C}} \cdot \mathbf{F}^{-1} \tag{4-27}$$

While the rate of deformation is expressed in current configuration, the rate of Green strain is expressed in the reference configuration. The two measures are two ways of viewing the same process.

Introducing the angular velocity tensor $\mathbf{\Omega}$, which is obtained by taking the time derivative of a rigid body motion, we will have:

$$\mathbf{\Omega} = \dot{\mathbf{R}}\mathbf{R}^T \tag{4-28}$$

It can be shown that $\mathbf{\Omega}$ is skewsymmetric, i.e.:

$$\frac{d\left(\mathbf{R}\mathbf{R}^T\right)}{dt} = \frac{d(\boldsymbol{\delta})}{dt} = 0 = \dot{\mathbf{R}}\mathbf{R}^T + \mathbf{R}\dot{\mathbf{R}}^T = \mathbf{\Omega} + \left(\dot{\mathbf{R}}\mathbf{R}^T\right)^T = \mathbf{\Omega} + \mathbf{\Omega}^T \tag{4-29}$$

Invoking:

$$\begin{aligned} \mathbf{L} &= \dot{\mathbf{F}}\mathbf{F}^{-1} = \left(\dot{\mathbf{R}}\mathbf{U} + \mathbf{R}\dot{\mathbf{U}}\right)\left(\mathbf{R}\mathbf{U}\right)^{-1} = \left(\dot{\mathbf{R}}\mathbf{U} + \mathbf{R}\dot{\mathbf{U}}\right)\mathbf{U}^{-1}\mathbf{R}^{-1} \\ &= \dot{\mathbf{R}}\mathbf{U}\mathbf{U}^{-1}\mathbf{R}^T + \mathbf{R}\dot{\mathbf{U}}\mathbf{U}^{-1}\mathbf{R}^T = \dot{\mathbf{R}}\mathbf{R}^T + \mathbf{R}\dot{\mathbf{U}}\mathbf{U}^{-1}\mathbf{R}^T \end{aligned} \tag{4-30}$$

Noticing that $\dot{\mathbf{U}}$ and $\mathbf{U}^{-1}$ are symmetric, $\mathbf{W}$ and $\mathbf{\Omega}$ are related through:

$$\begin{aligned} \mathbf{W} &= \frac{1}{2}\left(\mathbf{L} - \mathbf{L}^T\right) = \frac{1}{2}\left(\mathbf{\Omega} + \mathbf{R}\dot{\mathbf{U}}\mathbf{U}^{-1}\mathbf{R}^T - \mathbf{\Omega}^T - \mathbf{R}\left(\dot{\mathbf{U}}\mathbf{U}^{-1}\right)^T\mathbf{R}^T\right) \\ &= \mathbf{\Omega} + \frac{1}{2}\mathbf{R}\left(\dot{\mathbf{U}}\mathbf{U}^{-1} - \left(\dot{\mathbf{U}}\mathbf{U}^{-1}\right)^T\right)\mathbf{R}^T = \mathbf{\Omega} + \frac{1}{2}\mathbf{R}\left(\dot{\mathbf{U}}\mathbf{U}^{-1} - \mathbf{U}^{-1}\dot{\mathbf{U}}\right)\mathbf{R}^T \end{aligned} \tag{4-31}$$

D and $\mathbf{\Omega}$ are related through:

$$\mathbf{D} = \frac{1}{2}\left(\mathbf{L} + \mathbf{L}^T\right) = \frac{1}{2}\mathbf{R}\left(\dot{\mathbf{U}}\mathbf{U}^{-1} + \mathbf{U}^{-1}\dot{\mathbf{U}}\right)\mathbf{R}^T \tag{4-32}$$

It is obviously that the spin tensor and angular velocity tensor are identical in the rigid body rotation.

4.4 Stresses and stress rates

4.4.1 Stress measures

Various stress measures can be defined in nonlinear problems. We will consider four commonly used measures of stress:

- The Cauchy stress, $\boldsymbol{\sigma}$
- The Kirchhoff stress tensor τ,
- The nominal stress, Σ, which is closely related to the first Piola-Kirchhoff stress
- The second Piola-Kirchhoff stress Π,

By definition, the contact force vector **t** acting on the deformed surface, with area *da* and unit normal vector **n**, is related to the Cauchy stress tensor $\boldsymbol{\sigma}$:

$$\mathbf{t} = \mathbf{n}\boldsymbol{\sigma}da \tag{4-33}$$

In finite element analysis, one also finds the Kirchhoff stress tensor τ, which is related to the Cauchy stress tensor σ through:

$$\boldsymbol{\tau} = \det(\mathbf{F})\boldsymbol{\sigma} = J\boldsymbol{\sigma} \tag{4-34}$$

In some circumstances, it is convenient to define stresses in relation to undeformed surfaces. Initial surface **dA** and deformed surface **da** are related through:

$$\mathbf{da} = da\,\mathbf{n} = \det(\mathbf{F})\mathbf{dA}\,\mathbf{F}^{-1} = \det(\mathbf{F})\,dA\,\mathbf{N}\,\mathbf{F}^{-1} \tag{4-35}$$

where $\mathbf{F}^{-1}$ is the inverse transformation of the deformation gradient **F**, and dA is the area of the initial surface of normal **N**.

The nominal (Piola-Kirchhoff) stress tensor Σ is related with Cauchy stress, i.e.

$$\mathbf{t} = \mathbf{n}\boldsymbol{\sigma}da = \mathbf{N}\boldsymbol{\Sigma}dA \tag{4-36}$$

Using Eq. 35, Nominal, Cauchy and Kirchhoff stresses are related through:

$$\boldsymbol{\Sigma} = \det(\mathbf{F})\mathbf{F}^{-1}\boldsymbol{\sigma} = \mathbf{F}^{-1}\boldsymbol{\tau} \tag{4-37}$$

In general Σ is not symmetric. To restore the advantage of symmetry, the second Piola-Kirchhoff Π is introduced:

$$\boldsymbol{\Pi} = \boldsymbol{\Sigma}\left(\mathbf{F}^{-1}\right)^{T} = \det(\mathbf{F})\mathbf{F}^{-1}\boldsymbol{\sigma}\left(\mathbf{F}^{-1}\right)^{T} \tag{4-38}$$

In summary, the relation between the different stress measures is given in Table 1. These relations can be verified by using the transformation of current normal to the reference normal.

Table 4-1. Relations between different stress measures.

	Cauchy stress $\boldsymbol{\sigma}$	Kirchhoff stress $\boldsymbol{\tau}$	Nominal stress $\boldsymbol{\Sigma}$	Second Piola-Kirchhoff stress $\boldsymbol{\Pi}$
$\boldsymbol{\sigma}$		$J^{-1}\boldsymbol{\tau}$	$J^{-1}\mathbf{F}\boldsymbol{\Sigma}$	$J^{-1}\mathbf{F}\boldsymbol{\Pi}\mathbf{F}^{T}$
$\boldsymbol{\tau}$	$J\boldsymbol{\sigma}$		$\mathbf{F}\boldsymbol{\Sigma}$	$\mathbf{F}\boldsymbol{\Pi}\mathbf{F}^{T}$
$\boldsymbol{\Sigma}$	$J\mathbf{F}^{-1}\boldsymbol{\sigma}$	$\mathbf{F}^{-1}\boldsymbol{\tau}$		$\boldsymbol{\Pi}\mathbf{F}^{T}$
$\boldsymbol{\Pi}$	$J\mathbf{F}^{-1}\boldsymbol{\sigma}\mathbf{F}^{-T}$	$\mathbf{F}^{-1}\boldsymbol{\tau}\mathbf{F}^{-T}$	$\boldsymbol{\Sigma}\mathbf{F}^{-T}$	

Stress tensors and strain tensors are selected jointly so that they are conjugate measures of strain energy rate (Hill 1958). By definition the stress power or rate of strain energy is:

$$\dot{W} = \int_{\Omega} \boldsymbol{\sigma} : \mathbf{D}\, dv \tag{4-39}$$

The Kirchhoff stress is conjugate to rate of deformation **D**:

$$\int_{\Omega} \boldsymbol{\sigma} : \mathbf{D}\, dv = \int_{\Omega_0} \det(\mathbf{F})\boldsymbol{\sigma} : \mathbf{D}\, dV = \int_{\Omega_0} \boldsymbol{\tau} : \mathbf{D}\, dV \tag{4-40}$$

The first Piola-Kirchhoff stress $\boldsymbol{\Sigma}$ is conjugate to deformation gradient **F**:

$$\boldsymbol{\tau} : \mathbf{D} = \det(\mathbf{F})\boldsymbol{\sigma} : \mathbf{D} = \det(\mathbf{F})\boldsymbol{\sigma} : \mathbf{L} = \det(\mathbf{F})\boldsymbol{\sigma} : \left(\dot{\mathbf{F}}\,\mathbf{F}^{-1}\right) = \left(\det(\mathbf{F})\mathbf{F}^{-1}\boldsymbol{\sigma}\right) : \dot{\mathbf{F}} = \boldsymbol{\Sigma} : \dot{\mathbf{F}} \tag{4-41}$$

The second Piola-Kirchhoff stress $\boldsymbol{\Pi}$ is conjugate to the Lagrangian strain tensor **E**:

$$\begin{aligned} \boldsymbol{\tau} : \mathbf{D} &= \det(\mathbf{F})\boldsymbol{\sigma} : \mathbf{D} = \det(\mathbf{F})\boldsymbol{\sigma} : \left(\mathbf{F}^{T}\right)^{-1} \dot{\mathbf{E}}\,\mathbf{F}^{-1} = \det(\mathbf{F})\sigma_{ij} \left(F^{T}\right)^{-1}_{jk} \dot{E}_{km} F^{-1}_{mi} \\ &= \det(\mathbf{F}) F^{-1}_{mi}\sigma_{ij} \left(F^{T}\right)^{-1}_{jk} \dot{E}_{km} = \left(\det(\mathbf{F})\mathbf{F}^{-1}\boldsymbol{\sigma}\left(\mathbf{F}^{-1}\right)^{T}\right) : \dot{\mathbf{E}} = \boldsymbol{\Pi} : \dot{\mathbf{E}} \end{aligned} \tag{4-42}$$

4.4.2 Objective stress rates

The solution of boundary value problems involving material behavior requires that the mechanical response of materials be formulated in term of stress and strain. The main restriction for stress and strain tensors to qualify for describing stress-strain relationships is referred to as the principle of material indifference or material objectivity, a principle which is credited to Truesdell and Noll (1965). The principle of frame indifference postulates that constitutive equations should remain invariant under changes of reference frame and time. The constitutive relation should truly describe the material response that results from a deformation process, and should not be influenced by a change of coordinates during the deformation process. If the stress and strain selected to formulate a constitutive relation were to be influenced by an arbitrary change of coordinates, this would imply that the constitutive relationship would create an artificial (i.e., non-physical) representation of the material response.

The representation of any two vectors **x** and **x*** can be related as follows:

$$\mathbf{x}^* = \mathbf{c} + \mathbf{Q}\mathbf{x} \tag{4-43}$$

where **Q** is a rotation. Under the change of a reference basis, vectors and tensors are frame indifferent if they transform as follows:

$$\mathbf{v}^* = \mathbf{Q}\mathbf{v} \quad \text{and} \quad \mathbf{T}^* = \mathbf{Q}\mathbf{T}\mathbf{Q}^T \tag{4-44}$$

A constitutive relation is frame indifferent when it is formulated using vectors and tensors that obey Eq. 44.

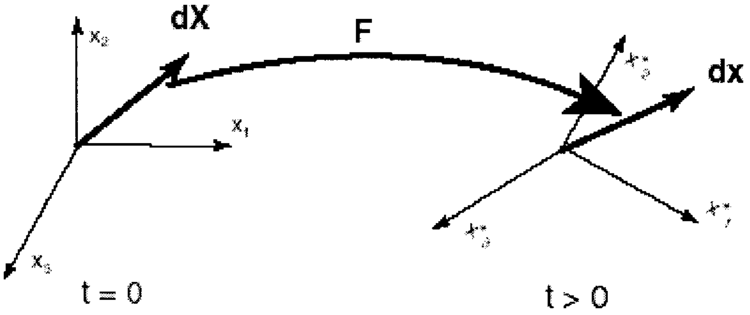

Figure 4-2. Reference frame moving with deformation process.

We will review three objective stress rates: the Jaunmann rate, the Truesdell rate and the Green-Naghdi-McInnis rate. All of these are frequently used in current finite element analysis.

One of most common rates is the Jaumann rate $\hat{\boldsymbol{\sigma}}$ of Cauchy stress (Truesdell and Noll 1965):

$$\hat{\boldsymbol{\sigma}} = \dot{\boldsymbol{\sigma}} + \boldsymbol{\sigma}\mathbf{W} - \mathbf{W}\boldsymbol{\sigma} \quad \text{i.e.,} \ \hat{\sigma}_{ij} = \dot{\sigma}_{ij} + \sigma_{ik}W_{kj} - W_{ik}\sigma_{kj} \tag{4-45}$$

where $\dot{\boldsymbol{\sigma}}$ is the material time derivative of Cauchy stress and $\mathbf{W}$ is the spin tensor defined in Eq 31. $\hat{\boldsymbol{\sigma}}$ is also called co-rotational as it represents a rate relative to a rotating frame of reference. The Truesdell rate of Cauchy stress is:

$$\breve{\boldsymbol{\sigma}} = \dot{\boldsymbol{\sigma}} - \mathbf{L}\boldsymbol{\sigma} - \boldsymbol{\sigma}\mathbf{L}^T + \boldsymbol{\sigma}\, tr(\mathbf{L}) \quad \text{i.e.,} \ \breve{\sigma}_{ij} = \dot{\sigma}_{ij} - L_{ik}\sigma_{kj} - \sigma_{ik}L_{jk} + \sigma_{ij}L_{kk} \tag{4-46}$$

It corresponds to the *Lie derivative* of Kirchhoff stress with a factor of J:

$$\widehat{\boldsymbol{\tau}} = \dot{\boldsymbol{\tau}} - \mathbf{L}\boldsymbol{\tau} - \boldsymbol{\tau}\mathbf{L}^T \quad \text{i.e.,} \ \widehat{\tau}_{ij} = \dot{\tau}_{ij} - L_{ik}\tau_{kj} - \tau_{ik}L_{jk} \tag{4-47}$$

Actually, any possible objective rate is particular instances of a general geometric concept called the Lie derivative (Marsden and Hughes, 1994).

The Green-Naghdi-McInnis rate is defined as:

$$\tilde{\boldsymbol{\sigma}} = \dot{\boldsymbol{\sigma}} - \left(\dot{\mathbf{R}}\mathbf{R}^T\right)\boldsymbol{\sigma} + \boldsymbol{\sigma}\left(\dot{\mathbf{R}}\mathbf{R}^T\right) \quad \text{i.e.,} \ \sigma_{ij} = \dot{\sigma}_{ij} + \sigma_{ik}\dot{R}_{kl}R_{jl} - \dot{R}_{ik}R_{lk}\sigma_{lj} \tag{4-48}$$

where is $\mathbf{R}$ the rotation coming from the polar decomposition of the deformation gradient defined in Eq 8.

Several objective rates (not all of them) can be written in a general form as:

$$\overset{*}{\boldsymbol{\sigma}} = \dot{\boldsymbol{\sigma}} + \boldsymbol{\sigma}\cdot\boldsymbol{\psi} - \boldsymbol{\psi}\cdot\boldsymbol{\sigma} \tag{4-49}$$

where $\boldsymbol{\psi}$ is a skew-symmetric tensor chosen so that $\overset{*}{\boldsymbol{\sigma}}$ transform objectively as defined in Eq. 44. As noted by Hughes (1984), given $\boldsymbol{\psi}$, we may generate a group of rotations $\Re$ such that:

$$\dot{\Re} = \boldsymbol{\psi} \cdot \Re \text{, and } \Re_{(t=0)} = \mathbf{1} \tag{4-50}$$

The Jaumann stress rate corresponds to the case:

$$\boldsymbol{\psi} = \mathbf{W} \tag{4-51}$$

And the Green-Naghdi-McInnis stress rate corresponds to the case:

$$\boldsymbol{\psi} = \dot{\mathbf{R}} \cdot \mathbf{R}^T \tag{4-52}$$

Defining the rotated stress using the procedure presented in Hughes (1984),

$$\boldsymbol{\sigma}_{\Re} = \Re^T \cdot \boldsymbol{\sigma} \cdot \Re \tag{4-53}$$

The time derivate of the rotated stress can be expressed as:

$$\begin{aligned} \dot{\boldsymbol{\sigma}}_{\Re} &= \dot{\Re}^T \cdot \boldsymbol{\sigma} \cdot \Re + \Re^T \cdot \dot{\boldsymbol{\sigma}} \cdot \Re + \Re^T \cdot \boldsymbol{\sigma} \cdot \dot{\Re} \\ &= \Re^T \cdot (-\boldsymbol{\psi}) \cdot \boldsymbol{\sigma} \cdot \Re + \Re^T \cdot \dot{\boldsymbol{\sigma}} \cdot \Re + \Re^T \cdot \boldsymbol{\sigma} \cdot (\boldsymbol{\psi}) \cdot \Re \\ &= \Re^T \cdot (\dot{\boldsymbol{\sigma}} + \boldsymbol{\sigma} \cdot \boldsymbol{\psi} - \boldsymbol{\psi} \cdot \boldsymbol{\sigma}) \cdot \Re \end{aligned} \tag{4-54}$$

This is obviously equivalent to:

$$\dot{\boldsymbol{\sigma}}_{\Re} = \Re^T \cdot \overset{*}{\boldsymbol{\sigma}} \cdot \Re \text{ or } \overset{*}{\boldsymbol{\sigma}} = \Re \cdot \dot{\boldsymbol{\sigma}}_{\Re} \cdot \Re^T \tag{4-55}$$

This means that a rather complicated objective stress rate can be computed as the simple time derivative of a rotated stress. As we will see in the following section, for the rate formulation of elasto-plasticity, this result allows the development of algorithms for finite strains which are identical to those for infinitesimal strains, provided that objects are rotated properly.

4.5 Hypoelastic constitutive equations using different stress rates

Most constitutive models for soils and rocks can be described using hypoelastic relations. Hypoelastic material laws relate the rate of stress to the rate of deformation. For large deformation analysis, the stress rate should be objective to satisfy the principle of material frame indifference. Some commonly used forms of hypoelastic constititutive relations are:

$$\breve{\boldsymbol{\sigma}} = \mathbf{C}^{\sigma T} : \mathbf{d} \quad \hat{\boldsymbol{\sigma}} = \mathbf{C}^{\sigma J} : \mathbf{d} \quad \tilde{\boldsymbol{\sigma}} = \mathbf{C}^{\sigma G} : \mathbf{d} \tag{4-56}$$

where $\mathbf{C}^{\sigma T}$, $\mathbf{C}^{\sigma J}$, $\mathbf{C}^{\sigma G}$ are the fourth-order tensor of elastic moduli cooresponding to the Truesdell rate, Jaumann rate, and Green-Naghdi-McInnis rate of Cauchy stress tensor $\boldsymbol{\sigma}$ respectively, which may depend upon the present states of stress and deformation.

4.5.1 Relation between tangent moduli

The tangent moduli $\mathbf{C}^{\sigma T}$, $\mathbf{C}^{\sigma J}$, $\mathbf{C}^{\sigma G}$ will be different for the same material, using the relationship between the different objective stress rate, the tangent moduli can be related. Using the definitions of the stress rate, the constitutive relation in terms of the Truesdell rate can be expressed:

$$\breve{\boldsymbol{\sigma}} = \mathbf{C}^{\sigma J} : \mathbf{d} - \mathbf{d} \cdot \boldsymbol{\sigma} - \boldsymbol{\sigma} \cdot \mathbf{d}^{T} + \boldsymbol{\sigma}\, tr(\mathbf{d}) = (\mathbf{C}^{\sigma J} - \mathbf{C}' + \boldsymbol{\sigma} \otimes \mathbf{I}) : \mathbf{d} = \mathbf{C}^{\sigma T} : \mathbf{d} \tag{4-57}$$

so the relation between the Jaumann and Truesdell moduli expressed by Cauchy stress measurement is

$$\mathbf{C}^{\sigma T} = \mathbf{C}^{\sigma J} - \mathbf{C}' + \boldsymbol{\sigma} \otimes \mathbf{I} = \mathbf{C}^{\sigma J} - \mathbf{C}^{*} \tag{4-58}$$

where $\mathbf{C}' : \mathbf{d} = \mathbf{d} \cdot \boldsymbol{\sigma} + \boldsymbol{\sigma} \cdot \mathbf{d}^T$ and

$$\mathbf{C}^* = \mathbf{C}' - \boldsymbol{\sigma} \otimes \mathbf{I}\text{, i.e., } C^*_{ijkl} = \frac{1}{2}(\delta_{ik}\sigma_{jl} + \delta_{il}\sigma_{jk} + \delta_{jk}\sigma_{il} + \delta_{jl}\sigma_{ik}) - \delta_{kl}\sigma_{ij} \tag{4-59}$$

Notice that $\mathbf{C}'$ has major symmetry, but $\mathbf{C}^*$ does not since $\boldsymbol{\sigma} \otimes \mathbf{I} \neq \mathbf{I} \otimes \boldsymbol{\sigma}$.

The relation between the Green-Naghdi moduli and the Truesdell moduli is obtained as follows.

$$\begin{aligned} \breve{\boldsymbol{\sigma}} &= \tilde{\boldsymbol{\sigma}} - (\mathbf{L} - \boldsymbol{\Omega}) \cdot \boldsymbol{\sigma} - \boldsymbol{\sigma} \cdot (\mathbf{L} - \boldsymbol{\Omega})^T + \boldsymbol{\sigma}\, tr(\mathbf{d}) \\ &= \mathbf{C}^{\sigma G} : \mathbf{d} - (\mathbf{L} - \boldsymbol{\Omega}) \cdot \boldsymbol{\sigma} - \boldsymbol{\sigma} \cdot (\mathbf{L} - \boldsymbol{\Omega})^T + \boldsymbol{\sigma}\, tr(\mathbf{d}) \\ &= \mathbf{C}^{\sigma G} : \mathbf{d} - \mathbf{d} \cdot \boldsymbol{\sigma} - \boldsymbol{\sigma} \cdot \mathbf{d}^T - (\boldsymbol{\omega} - \boldsymbol{\Omega}) \cdot \boldsymbol{\sigma} - \boldsymbol{\sigma} \cdot (\boldsymbol{\omega} - \boldsymbol{\Omega})^T + \boldsymbol{\sigma}\, tr(\mathbf{d}) \end{aligned} \tag{4-60}$$

A complex derivation (Simo and Hughes 1998; Mehrabadi and NematNasser 1987) leads to the final expression

$$\mathbf{C}^{\sigma T} = \mathbf{C}^{\sigma G} - \mathbf{C}^* - \mathbf{C}^{spin} \tag{4-61}$$

Here the fourth order tensor is a function of the left stretch tensor and the Cauchy stress given by,

$$\mathbf{C}^{spin} : \mathbf{d} = (\boldsymbol{\omega} - \boldsymbol{\Omega}) \cdot \boldsymbol{\sigma} + \boldsymbol{\sigma} \cdot (\boldsymbol{\omega} - \boldsymbol{\Omega})^T \tag{4-62}$$

The tensor does not have major symmetry but possesses minor symmetry and skew-symmetry (Simo and Hughes 1998). In other word, it follows that constitutive equation possesses nonsymmetric moduli. As a result, this formulation leads necessarily to nonsymmetric tangent stiffness matrixes in numerical implementations.

It has been seen that if the Jaumann rate or Green-Naghdi-McInnis rate of Cauchy stress had been chosen to formulate stress-strain relation, the symmetry of the stiffness matrix is lost when generalizing from small to large deformations. For this reason, the objective rate of Kirchhoff stress can be selected in the present formulation to avoid to generate a nonsymmetric stiffness matrix.

For the Jaumann rate of Kirchhoff stress, we have

$$\hat{\boldsymbol{\tau}} = \dot{\boldsymbol{\tau}} - \boldsymbol{\omega}\cdot\boldsymbol{\tau} - \boldsymbol{\tau}\cdot\boldsymbol{\omega}^T, \ \hat{\boldsymbol{\tau}} = \mathbf{C}^{\tau J} : \mathbf{d} \tag{4-63}$$

The corresponding tangent moduli can be derived as

$$\mathbf{C}^{\sigma T} = J^{-1}\mathbf{C}^{\tau J} - \mathbf{C}' \tag{4-64}$$

Since the $\mathbf{C}'$ has symmetry, the tangent moduli $\mathbf{C}^{\sigma T}$ for the Jaumann rate of Kirchhoff stress in Eq. is symmetric.

An expression for the material time derivative of the Cauchy stress can be obtained for stress update algorithms in finite element analysis from the tangent moduli $\mathbf{C}^{\sigma T}$:

$$\begin{aligned}\dot{\boldsymbol{\sigma}} &= \breve{\boldsymbol{\sigma}} + \mathbf{L}\boldsymbol{\sigma} + \boldsymbol{\sigma}\mathbf{L}^T - \boldsymbol{\sigma}\, tr(\mathbf{L}) \\ &= (\mathbf{C}^{\sigma T} + \mathbf{C}'' - \boldsymbol{\sigma}\otimes\mathbf{I}) : \mathbf{d}\end{aligned} \tag{4-65}$$

where $C''_{ijkl} = \delta_{ik}\sigma_{jl} + \delta_{jk}\sigma_{il}$.

In the case of small displacement and rate-independent materials, both sides of Eq. 65 may be multiplied by a time interval *dt*. The stress rate becomes the stress increment $\mathbf{d}\boldsymbol{\sigma}$ and the rate of deformation becomes the strain increment $\mathbf{d}\boldsymbol{\varepsilon}$. Eq. 65 becomes equivalent to the following incremental relation between stress and strain:

$$\mathbf{d}\boldsymbol{\sigma} = \mathbf{C} : \mathbf{d}\boldsymbol{\varepsilon} \ \text{ i.e., } d\sigma_{ij} = C_{ijkl}\, d\varepsilon_{kl} \tag{4-66}$$

4.5.2 Objective rate performance in simple shear condition

To understand the characteristic of the tangent moduli of different objective stress rate, consider an element in simple shear as shown in Figure 3, the element undergoes pure shearing deformation with constant volume, the motion of the element at time t is given by

$$x = X + aY, \; y = Y \tag{4-67}$$

where $a = \tan\theta$ represents rotation of the edge of the element, which vary with time.

The deformation gradient is given as:

$$\mathbf{F} = \begin{bmatrix} 1 & a \\ 0 & 1 \end{bmatrix}, \; \dot{\mathbf{F}} = \begin{bmatrix} 0 & \dot{a} \\ 0 & 0 \end{bmatrix}, \text{ and } \mathbf{F}^{-1} = \begin{bmatrix} 1 & -a \\ 0 & 1 \end{bmatrix} \tag{4-68}$$

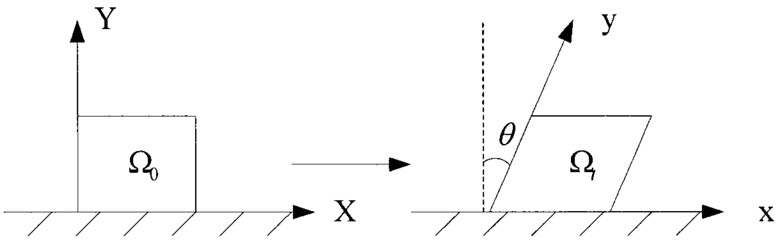

Figure 4-3. Element under simple shearing.

The velocity gradient, the rate of deformation and the spin tensor can be computed from the deformation gradient,

$$\mathbf{L} = \dot{\mathbf{F}}\mathbf{F}^{-1} = \begin{bmatrix} 0 & \dot{a} \\ 0 & 0 \end{bmatrix}, \; \mathbf{d} = \frac{1}{2}\begin{bmatrix} 0 & \dot{a} \\ \dot{a} & 0 \end{bmatrix}, \text{ and } \boldsymbol{\omega} = \frac{1}{2}\begin{bmatrix} 0 & \dot{a} \\ -\dot{a} & 0 \end{bmatrix} \tag{4-69}$$

The hypoelastic isotropic constitutive equation in terms of the Truesdell rate is given by

$$\dot{\boldsymbol{\sigma}} = \lambda^T tr(\mathbf{d}) + 2\mu^T \mathbf{d} + \mathbf{L}\cdot\boldsymbol{\sigma} + \boldsymbol{\sigma}\cdot\mathbf{L}^T - \boldsymbol{\sigma}\, tr(\mathbf{L}) \qquad (4\text{-}70)$$

Here we use the superscripts on the material constants to distinguish the material constants used with different objective rates. Using the matrix for the above equation gives

$$\begin{aligned}\begin{bmatrix} \dot{\sigma}_x & \dot{\sigma}_{xy} \\ \dot{\sigma}_{xy} & \dot{\sigma}_y \end{bmatrix} &= \mu^T \dot{a}\begin{bmatrix} 0 & 1 \\ 1 & 0 \end{bmatrix} + \begin{bmatrix} 0 & \dot{a} \\ 0 & 0 \end{bmatrix}\begin{bmatrix} \sigma_x & \sigma_{xy} \\ \sigma_{xy} & \sigma_y \end{bmatrix} + \begin{bmatrix} 0 & 0 \\ \dot{a} & 0 \end{bmatrix}\begin{bmatrix} \sigma_x & \sigma_{xy} \\ \sigma_{xy} & \sigma_y \end{bmatrix} \\ &= \mu^T \dot{a}\begin{bmatrix} 0 & 1 \\ 1 & 0 \end{bmatrix} + \dot{a}\begin{bmatrix} \sigma_{xy} & \sigma_y \\ 0 & 0 \end{bmatrix} + \dot{a}\begin{bmatrix} \sigma_{xy} & 0 \\ \sigma_y & 0 \end{bmatrix}\end{aligned} \qquad (4\text{-}71)$$

we obtain the relation of the time derivative of normal and shear stress as follows

$$\dot{\sigma}_x = 2\sigma_{xy}\dot{a}\,,\ \dot{\sigma}_y = 0\,,\ \text{and}\ \dot{\sigma}_{xy} = (\mu^T + \sigma_{xy})\dot{a} \qquad (4\text{-}72)$$

If initially all stress is zero, the solution to the above differential equation are

$$\sigma_x = \mu^T a^2\,,\ \sigma_y = 0\,,\ \text{and}\ \sigma_{xy} = \mu^T a \qquad (4\text{-}73)$$

For the Jaumann rate of Cauchy stress, the hypoelastic, isotropic constitutive equation is given by

$$\dot{\boldsymbol{\sigma}} = \lambda^J tr(\mathbf{d}) + 2\mu^J \mathbf{d} + \boldsymbol{\omega}\cdot\boldsymbol{\sigma} + \boldsymbol{\sigma}\cdot\boldsymbol{\omega}^T \qquad (4\text{-}74)$$

Using the matrix form of the Jaumann rate of Cauchy stress, the above equation can be written as:

$$\begin{bmatrix}\dot{\sigma}_x & \dot{\sigma}_{xy}\\ \dot{\sigma}_{xy} & \dot{\sigma}_y\end{bmatrix} = \mu^J\dot{a}\begin{bmatrix}0 & 1\\ 1 & 0\end{bmatrix} + \frac{1}{2}\begin{bmatrix}0 & \dot{a}\\ -\dot{a} & 0\end{bmatrix}\begin{bmatrix}\sigma_x & \sigma_{xy}\\ \sigma_{xy} & \sigma_y\end{bmatrix} + \frac{1}{2}\begin{bmatrix}0 & -\dot{a}\\ \dot{a} & 0\end{bmatrix}\begin{bmatrix}\sigma_x & \sigma_{xy}\\ \sigma_{xy} & \sigma_y\end{bmatrix}$$

$$= \mu^J\dot{a}\begin{bmatrix}0 & 1\\ 1 & 0\end{bmatrix} + \dot{a}\begin{bmatrix}\sigma_{xy} & \dfrac{\sigma_y-\sigma_x}{2}\\ \dfrac{\sigma_y-\sigma_x}{2} & -\sigma_{xy}\end{bmatrix} \tag{4-75}$$

The relation of the time derivative of normal and shear stress as follows

$$\dot{\sigma}_x = \sigma_{xy}\dot{a}\,,\ \dot{\sigma}_y = -\sigma_{xy}\dot{a}\,,\ \text{and}\ \dot{\sigma}_{xy} = \left[\mu^J + \frac{1}{2}(\sigma_y - \sigma_x)\right]\dot{a} \tag{4-76}$$

and the solution is

$$\sigma_x = -\sigma_y = \mu^J(1-\cos a)\,,\ \text{and}\ \sigma_{xy} = \mu^J \sin a \tag{4-77}$$

Same calculation can be performed for the Green-McInnis rate of Cauchy stress. We need to find the rotation matrix **R** by the polar decomposition theorem. A closed form solution has been given by Dienes (1979):

$$\begin{aligned}\sigma_x &= -\sigma_y = 4\mu^G\left(\cos 2\beta \ln\cos\beta + \beta\sin 2\beta - \sin^2\beta\right)\\ \sigma_{xy} &= 2\mu^G\cos 2\beta\left(2\beta - 2\tan 2\beta\ln\cos\beta - \tan\beta\right)\end{aligned} \tag{4-78}$$

Figure 4 illustrates the stress versus the rotation angle θ with stress normalized by shear modulus.The results in Figure 4 shows that at small deformation range ($\theta \leq 20^0$) different objective rate gives the consistent result, but at very large deformation there is no agreement between various objective rates. The Jaumann rate shows the stress oscillation at very large deformation which has been identify by Dienes (1979). In fact, it is a misuse of material models to employ the same constants with different objective rates.

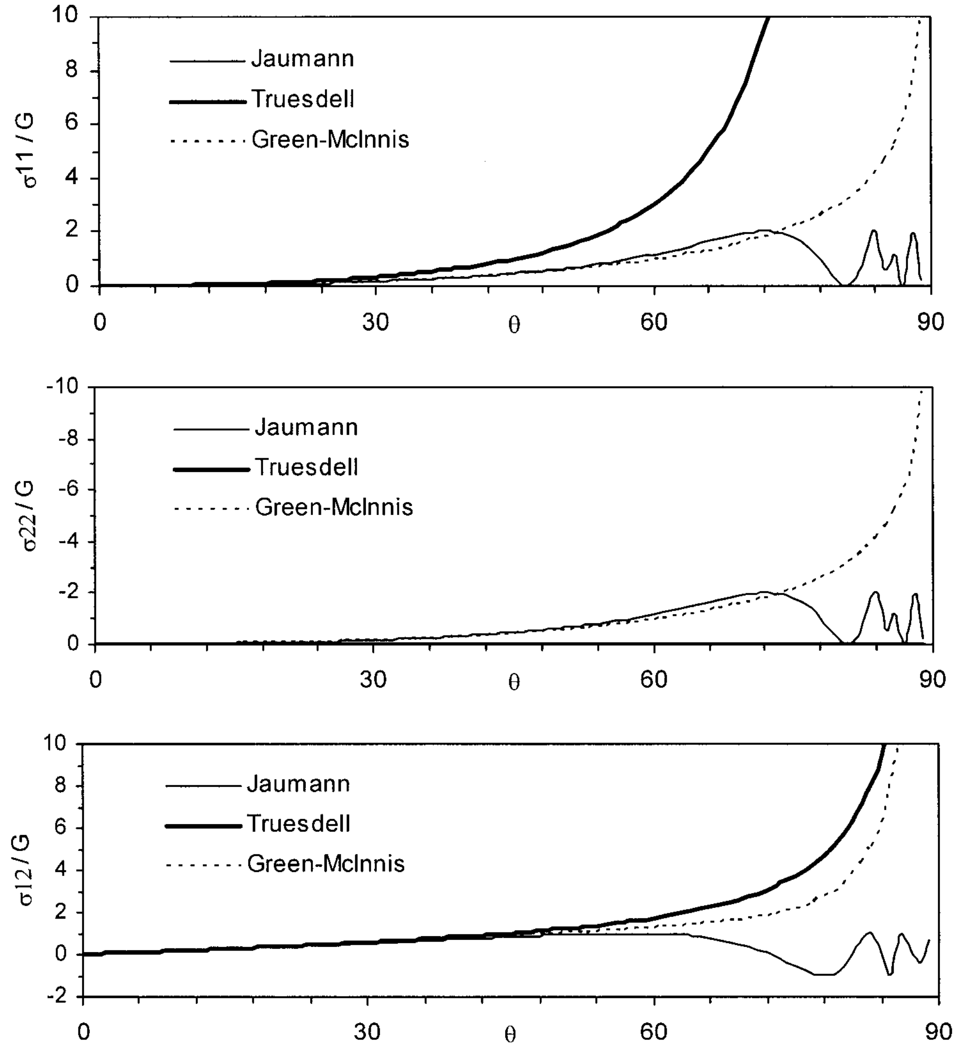

Figure 4-4. Comparison of stresses for various objective rates for simple shear problem with same material constants.

4.6 Finite strain elasto-plasticity based on additive theory

The formulation based on additive decomposition of the rate of deformation and hypoelastic constitutive relations, which is widely used in numerical analysis at geomechanics field, has been adopted in this research. In this section, the theory of finite strain elasto-plasticity is generalized. The strain increment in the spatial configuration will be formulated using deformation gradient. Two type rotation vector, one for Green-McInnis stress rate and one for Jaumann rate, are formulated to implement the algorithm for finite strain elasto-plasticity.

4.6.1 Additive decomposition of the rate of deformation and hypoelasticity

Based on an additive split of the rate of deformation into elastic and plastic parts, for finite strain elasto-plasticity, similarly as the infinitesimal elasto-plasticity, we can have tow key assumption as following,

$$\mathbf{d} = \mathbf{d}^e + \mathbf{d}^p , \ \overset{*}{\boldsymbol{\tau}} = \mathbf{c} : \left(\mathbf{d} - \mathbf{d}^p\right) \tag{4-79}$$

where $\mathbf{d}$, $\mathbf{d}^e$ and $\mathbf{d}^p$ are the total, elastic and plastic rate of deformation tensors, respectively and $\overset{*}{\boldsymbol{\tau}}$ is an objective rate of the Kirchhoff stress tensor $\boldsymbol{\tau}$.

As discussed in previous section, the objective stress rate can related to the material time derivative of rotated stress:

$$\dot{\boldsymbol{\tau}}_{\Re} = \Re^T \cdot \overset{*}{\boldsymbol{\tau}} \cdot \Re \text{ or } \overset{*}{\boldsymbol{\tau}} = \Re \cdot \dot{\boldsymbol{\tau}}_{\Re} \cdot \Re^T \tag{4-80}$$

where the rotation can be computed according to different choice of objective rate. Substitute the rate type constitutive equation derive in Eq. 57 or Eq. 58, Eq. 80 becomes:

$$\dot{\boldsymbol{\tau}}_{\Re} = \Re^T \cdot \left(\mathbf{c} : \mathbf{d}^e\right) \cdot \Re \tag{4-81}$$

Using the identity of rotation tensor $\Re^T \cdot \Re = \Re \cdot \Re^T = \mathbf{1}$, we can express the above equation in index format:

$$(\dot{\tau}_{\Re})_{ij} = (\Re_{ki}\Re_{lj}\Re_{pm}\Re_{qn}c_{klpq})(\Re_{rm}\Re_{sn}d^{e}_{rs}) \tag{4-82}$$

which can be simplified as

$$(\dot{\tau}_{\Re})_{ij} = (c_{\Re})_{ijmn}\left[(d_{\Re})_{mn} - (d^{p}_{\Re})_{mn}\right], \text{ or } \dot{\boldsymbol{\tau}}_{\Re} = \mathbf{c}_{\Re} : \left(\mathbf{d}_{\Re} - \mathbf{d}^{p}_{\Re}\right) \tag{4-83}$$

where is $\mathbf{c}_{\Re}$ the rotated Hooke's operator, $\mathbf{d}_{\Re}$ and $\mathbf{d}^{p}_{\Re}$ are the rotated total and plastic rate of deformation tensors, respectively. The format of this equation is identical to its infinitesimal strain theory except that all tensors here have to be properly rotated with $\Re$. We can formulate the finite strain elasto-plastic constitutive equation using the similar matter as in infinitesimal theory.

4.6.2 Computation of the strain increment

In most computer simulations, the incremental constitutive relation is implemented by calculating stresses resulting from a strain increment of finite amplitude. One of the efficient stress calculation algorithms is derived from the return mapping introduced by Ortiz and Simo (1986). With a generalized mid-point rule, time discretization of the basic constitutive equation over a time interval $[t_n, t_{n+1}]$ can be written as:

$$\boldsymbol{\tau}_{\Re(n+1)} = \boldsymbol{\tau}_{\Re(n)} + \mathbf{c}_{\Re(n+\alpha)} : \left(\mathbf{d}_{\Re(n+\alpha)} - \mathbf{d}_{\Re(n+\alpha)}{}^{p}\right)\Delta t \tag{4-84}$$

where the following notation has been used:

$$\begin{aligned} &\Delta(\bullet) \equiv (\bullet)_{n+1} - (\bullet)_{n}; \\ &(\bullet)_{n+\alpha} = (\bullet)_{(t=t_{n+\alpha})}; \\ &t_{n+\alpha} = (1-\alpha)t_{n} + \alpha t_{n+1}, \alpha \in [0,1] \end{aligned} \tag{4-85}$$

Introducing the rotated strain increment $\Delta\boldsymbol{\varepsilon}_{\Re(n+\alpha)}$ at time interval Δt,

$$\Delta\boldsymbol{\varepsilon}_{\Re(n+\alpha)} \equiv \mathbf{d}_{\Re(n+\alpha)}\Delta t = \Re^{T}_{n+\alpha} \cdot \left(\mathbf{d}_{n+\alpha}\Delta t\right) \cdot \Re_{n+\alpha} \tag{4-86}$$

Eq. 84 can be written in a form similar to its infinitesimal strain counterpart as following:

$$\boldsymbol{\tau}_{\Re(n+1)} = \boldsymbol{\tau}_{\Re(n)} + \mathbf{c}_{\Re(n+\alpha)} : \left(\Delta\boldsymbol{\varepsilon}_{\Re(n+\alpha)} - \Delta\boldsymbol{\varepsilon}_{\Re(n+\alpha)}{}^{p}\right) \tag{4-87}$$

Define a intermediate position $\mathbf{x}_{n+\alpha}$ of using a linear interpolation of the current positions over each time interval $\left[t_n, t_{n+1}\right]$:

$$\mathbf{x}_{n+\alpha} = (1-\alpha)\mathbf{x}_n + \alpha\mathbf{x}_{n+1}, \alpha \in \left[0,1\right] \tag{4-88}$$

Therefore, the corresponding deformation gradients also has the relationship as

$$\mathbf{F}_{n+\alpha} = (1-\alpha)\mathbf{F}_n + \alpha\mathbf{F}_{n+1}, \alpha \in \left[0,1\right] \tag{4-89}$$

Using the right Cauchy-Green Strain $\mathbf{C} = \mathbf{F}^{T} \cdot \mathbf{F}$, we can get

$$\Delta\mathbf{C} = \mathbf{F}^{T}_{n+1} \cdot \mathbf{F}_{n+1} - \mathbf{F}^{T}_{n} \cdot \mathbf{F}_{n} \tag{4-90}$$

and

$$\dot{\mathbf{C}} = 2\mathbf{F}^{T} \cdot \mathbf{d} \cdot \mathbf{F} \tag{4-91}$$

Time discretization of this relation gives:

$$\Delta\mathbf{C} = \left(\dot{\mathbf{C}}\right)_{n+\alpha} \Delta t = 2\mathbf{F}^{T}_{n+\alpha} \cdot \mathbf{d}_{n+\alpha} \cdot \mathbf{F}_{n+\alpha}\Delta t \tag{4-92}$$

so we get the strain increment as

$$\Delta\varepsilon = \mathbf{d}_{n+\alpha}\Delta t = \frac{1}{2}\mathbf{F}^{-T}_{n+\alpha} \cdot \left(\Delta\mathbf{C}\right) \cdot \mathbf{F}^{-1}_{n+\alpha} \tag{4-93}$$

It can be shown that second-order accuracy is achieved for $\alpha = 1/2$; this corresponds to the mid-point strain (Hughes 1984).

4.6.3 Polar decomposition algorithm for Green-Naghdi-McInnis rate

For Green-Naghdi-McInnis objective stress rate, the rotation $\mathfrak{R}$ coincides with $\mathbf{R}$, which comes from the polar decomposition rotation defined by $\mathbf{F} = \mathbf{R} \cdot \mathbf{U}$. Using Cardan's formula to compute the eigenvalues $\left(\lambda_1^2, \lambda_2^2, \lambda_3^2\right)$ of $\mathbf{C} = \mathbf{F}^T \cdot \mathbf{F}$. The principal direction $\left(\mathbf{N}^{(1)}, \mathbf{N}^{(2)}, \mathbf{N}^{(3)}\right)$ of $\mathbf{C}$ can be formed in their tensor products form as following, if $\lambda_1 \neq \lambda_2 \neq \lambda_3$

$$\mathbf{N}^{(A)} \otimes \mathbf{N}^{(A)} = \frac{\left(\mathbf{C} - \lambda_B^2 \mathbf{1}\right) \cdot \left(\mathbf{C} - \lambda_C^2 \mathbf{1}\right)}{\left(\lambda_A^2 - \lambda_B^2\right)\left(\lambda_A^2 - \lambda_C^2\right)} \tag{4-94}$$

Since $\mathbf{C} = \mathbf{U}^2$, so $\mathbf{U}$ and $\mathbf{C}$ have the same eigenvalue and principal direction. And $\mathbf{U}$ can be expressed from its spectral decomposition as follows:

$$\mathbf{U} = \sum_{A=1}^{3} \lambda_A \frac{\left(\mathbf{C} - \lambda_B^2 \mathbf{1}\right) \cdot \left(\mathbf{C} - \lambda_C^2 \mathbf{1}\right)}{\left(\lambda_A^2 - \lambda_B^2\right)\left(\lambda_A^2 - \lambda_C^2\right)} \tag{4-95}$$

Where (A, B, C) is an even permutation of $(1,2,3)$.

For $\lambda_1 = \lambda_2 \neq \lambda_3$

$$\mathbf{N}^{(3)} \otimes \mathbf{N}^{(3)} = \frac{\mathbf{C} - \lambda_1^2 \mathbf{1}}{\lambda_3^2 - \lambda_1^2} \quad \mathbf{U} = \lambda_1 \mathbf{1} + (\lambda_3 - \lambda_1) \mathbf{N}^{(3)} \otimes \mathbf{N}^{(3)} \tag{4-96}$$

For $\lambda_1 = \lambda_2 = \lambda_3$

$$\mathbf{U} = \lambda_1 \mathbf{1} \tag{4-97}$$

It is shown in Ting (1985) that all three cases can be combined into a unique, singularity-free formula:

$$\mathbf{U} = \frac{1}{i_1 i_2 - i_3}\left[-\mathbf{C}^2 + (i_1^2 - i_2)\mathbf{C} + i_1 i_3 \mathbf{1}\right] \tag{4-98}$$

where $i_1 = \lambda_1 + \lambda_2 + \lambda_3$, $i_2 = \lambda_1\lambda_2 + \lambda_2\lambda_3 + \lambda_3\lambda_1$, $i_3 = \lambda_1\lambda_2\lambda_3$

Using the Cayley-Hamilton theorm, the inverse of is $\mathbf{U}$ given by:

$$\mathbf{U}^{-1} = \frac{1}{i_3}\left[\mathbf{C} - i_1\mathbf{U} + i_2\mathbf{1}\right] \tag{4-99}$$

And the rotation is obtained as $\mathbf{R} = \mathbf{F} \cdot \mathbf{U}^{-1}$ (4-100)

The close form algorithm for the polar decomposition is summarized in Table 2. The procedure of the rotated the Green-McInnis-Naghdi stress rate can be summarized as in Table 3.

Table 4-2. Algorithm for the Polar Decomposition of F

```
1. Principal invariants of matrix $\mathbf{F}$
   $I_1 = tr\mathbf{F} \; : \; I_2 = \frac{1}{2}\left(I_1^2 - tr\left[\mathbf{F}^2\right]\right) \; : \; I_3 = \det\mathbf{F}$
2. Eigenvalue $\lambda_A^2, A = 1,2,3$ of matrix $\mathbf{F}$
   Set $b = I_2 - I_1^2/3 \; : \; c = -\frac{2}{27}I_1^3 + \frac{I_1 I_3}{3} - I_3$
   IF $(|b| \le TOL)$ THEN
      $x_A = -c^{1/3}$
   ELSE
      $m = 2\sqrt{-b/3} \; : \; n = \frac{3c}{mb}$
      $t = \arctan\left[\sqrt{1-n^2}/n\right]/3 \; : \; x_A = m\cos\left[t + 2(A-1)\pi/3\right]$
   ENDIF
   $\lambda_A^2 = x_A + I_1/3$
3. Computer the stretch tensor $\mathbf{U}$
      Computer the invariants of $\mathbf{U}$
         $i_1 = \lambda_1 + \lambda_2 + \lambda_3$
         $i_2 = \lambda_1\lambda_2 + \lambda_1\lambda_3 + \lambda_2\lambda_3$
         $i_3 = \lambda_1\lambda_2\lambda_3$
      Set
         $D = i_1 i_2 - i_3$
         $\mathbf{U} = \frac{1}{D}\left[-\mathbf{F}^2 + \left(i_1^2 - i_2\right)\mathbf{F} + i_1 i_3 \mathbf{1}\right]$
         $\mathbf{U}^{-1} = \frac{1}{i_3}\left[\mathbf{F} - i_1\mathbf{U} + i_2\mathbf{1}\right]$
4. Computer the rotation tensor $\mathbf{R} = \mathbf{F}\mathbf{U}^{-1}$
```

Table 4-3. Rotated configuration for Green-Naghdi-McInnis stress rate.

1. Polar decomposition of $\mathbf{F}_n = \mathbf{R}_n \mathbf{U}_n$
2. $\mathfrak{R}_n = \mathbf{R}_n$
3. Polar decomposition of $\mathbf{F}_{n+1} = \mathbf{R}_{n+1} \mathbf{U}_{n+1}$
4. $\mathfrak{R}_{n+1} = \mathbf{R}_{n+1}$
5. $\mathbf{F}_{n+1/2} = \frac{1}{2}(\mathbf{F}_{n+1} + \mathbf{F}_n)$
6. Polar decomposition of $\mathbf{F}_{n+1/2} = \mathbf{R}_{n+1/2} \mathbf{U}_{n+1/2}$
7. $\mathfrak{R}_{n+1/2} = \mathbf{R}_{n+1/2}$

4.6.4 Time-stepping algorithms for Jaumann stress rate

For Jaumann objective stress rate, the skew-symmetric matrix $\dot{\mathbf{W}}$ is equal to the spin tensor $\boldsymbol{\omega}$,

$$\dot{\mathbf{W}} = \boldsymbol{\omega}; \quad \boldsymbol{\omega} = \frac{1}{2}\left(\boldsymbol{l} - \boldsymbol{l}^{\mathrm{T}}\right) \tag{4-101}$$

Where $\boldsymbol{l}$ is the velocity gradient.

For $\dot{\mathfrak{R}} = \dot{\mathbf{W}} \cdot \mathfrak{R}$, using the exponential scheme as advocated by Simo and Taylor (1985),

$$\mathfrak{R}_{n+1} = (\exp W) \cdot \mathfrak{R}_n; \quad W = \dot{\mathbf{W}}_{n+\alpha} \Delta t \tag{4-102}$$

$(\exp W)$ can be evaluated through the following algebra.

Introducing the following notation:

$$W \equiv \begin{bmatrix} 0 & -w_3 & w_2 \\ w_3 & 0 & -w_1 \\ -w_2 & w_1 & 0 \end{bmatrix}, \quad w \equiv \begin{bmatrix} w_1 \\ w_2 \\ w_3 \end{bmatrix} \tag{4-103}$$

According to Goldstein (1981) and Whittaker (1944),

$$\exp \boldsymbol{W} = \mathbf{1} + \frac{2}{1+\|\bar{\boldsymbol{w}}\|^2}(\bar{\boldsymbol{W}} + \bar{\boldsymbol{W}}^2); \qquad \bar{\boldsymbol{w}} \equiv \frac{\boldsymbol{w}}{\|\boldsymbol{w}\|}\tan\frac{\|\boldsymbol{w}\|}{2} \tag{4-104}$$

And we know that $\dot{\mathbf{F}} = \boldsymbol{l} \cdot \mathbf{F}$, time discretization with the mid-point rule gives:

$$\boldsymbol{l}_{n+1/2}\Delta \boldsymbol{t} = (\mathbf{F}_{n+1} - \mathbf{F}_n) \cdot \mathbf{F}^{-1}_{n+1/2} = \boldsymbol{G}_{1/2}\,; \; \boldsymbol{G}_{1/2} \equiv \frac{\partial(\boldsymbol{x}_{n+1} - \boldsymbol{x}_n)}{\partial \boldsymbol{x}_{n+1/2}} \tag{4-105}$$

so we can get

$$\boldsymbol{\omega}_{n+1/2}\Delta \boldsymbol{t} = \frac{1}{2}\left(\boldsymbol{G}_{1/2} - \boldsymbol{G}^T_{1/2}\right) \tag{4-106}$$

Once the following skew-symmetric tensor:

$$\boldsymbol{W} = \boldsymbol{\omega}_{n+\square}\,\Delta \boldsymbol{t} \tag{4-107}$$

is known, the rotation at is given by:

$$\boldsymbol{\chi}_{n+1} = (\exp \boldsymbol{W}) \cdot \boldsymbol{\chi}_n \tag{4-108}$$

For a time interval $[t_n, t_{n+1}]$, we know $\boldsymbol{F}_n$, $\boldsymbol{F}_{n+1}$, $\boldsymbol{\chi}_n$ and $\boldsymbol{\tau}_n$ at $\boldsymbol{t}_n$, the problem is find $\boldsymbol{\sigma}_{n+1}$, $\boldsymbol{\chi}_{n+1}$ and the tangent operator $\boldsymbol{c}^{a\lg}_{n+1}$. The step by step procedure is given in Table 3 for the mid point integration rule.

Table 4-4. Rotated configuration for Jaumann stress rate.

Assuming we know $\Re_n$ at t_n,

1. $\mathbf{F}_{n+1/2} = \frac{1}{2}(\mathbf{F}_{n+1} + \mathbf{F}_n)$
2. Polar decomposition of $\mathbf{F}_{n+1/2} = \mathbf{R}_{n+1/2}\mathbf{U}_{n+1/2}$
3. $\mathbf{G}_{1/2} = (\mathbf{F}_{n+1} - \mathbf{F}_n)\cdot\mathbf{F}_{n+1/2}^{-1}$
4. $\mathbf{W} = \omega_{n+1/2}\Delta t = \frac{1}{2}\left(G_{1/2} - G_{1/2}^{T}\right)$ (skew-symmetry matrix)
5. set $w \equiv \left[W_{32} \quad W_{13} \quad W_{21}\right]^{T}$
6. $\bar{w} \equiv \frac{w}{\|w\|}\tan\frac{\|w\|}{2}$
7. $\bar{W} \equiv \begin{bmatrix} 0 & -\bar{w}_3 & \bar{w}_2 \\ \bar{w}_3 & 0 & -\bar{w}_1 \\ -\bar{w}_2 & \bar{w}_1 & 0 \end{bmatrix}$
8. $\exp W = \mathbf{1} + \frac{2}{1+\|\bar{w}\|^2}(\bar{W} + \bar{W}^2)$
9. $\Re_{n+1} = (\exp W)\cdot\Re_n$
10. $\Re_{n+1/2} = \exp(\frac{W}{2})\cdot\Re_n$

4.6.5 Numerical implementation of finite strain elasto-plasticity

We summarize the different algorithm steps for the numerical implantation of finite strain elasto-plasticity formulated in rate form. For a time interval $\left[t_n, t_{n+1}\right]$ and a given quadrature point, the known information for this step calculation are $\mathbf{F}_n$, $\mathbf{F}_{n+1}$, $\Re_n$, $\boldsymbol{\tau}_n$, constitutive history variables and material parameters. The problem is to compute $\boldsymbol{\tau}_{n+1}$, $\Re_{n+1}$ and the tangent operator $c_{n+1}^{a\mathrm{lg}}$. The step by step procedure is given the following for the integration parameter $\alpha = 1/2$.

- (1) Compute the rotations $\Re_{n+1}$ and $\Re_{n+1/2}$; for McInnis stress rate, using Table 3; for Jaumann stress rate, using Table 4.

- (2) Compute the strain increment $\Delta\boldsymbol{\varepsilon}_{(n+1/2)} \equiv \mathbf{d}_{n+1/2}\Delta t$

$$\mathbf{F}_{n+1/2} = \frac{1}{2}\left(\mathbf{F}_{n+1} + \mathbf{F}_{n}\right)$$

$$\Delta\mathbf{C} = \mathbf{F}_{n+1}^{T}\mathbf{F}_{n+1} - \mathbf{F}_{n}^{T}\mathbf{F}_{n}$$

$$\Delta\boldsymbol{\varepsilon}_{(n+1/2)} = \frac{1}{2}\mathbf{F}_{n+1/2}^{-T}\cdot\left(\Delta\mathbf{C}\right)\cdot\mathbf{F}_{n+1/2}^{-1}$$

- (3) Computer the rotated strain increment:

$$\Delta\boldsymbol{\varepsilon}_{\Re(n+1/2)} \equiv \mathbf{d}_{\Re(n+1/2)}\Delta t = \Re_{n+1/2}^{T}\cdot\Delta\boldsymbol{\varepsilon}_{n+1/2}\cdot\Re_{n+1/2}$$

- (4) Computer the rotated Kirchhoff stresses at t_n

$$\boldsymbol{\tau}_{\Re(n)} = \Re_{n}^{T}\cdot\boldsymbol{\tau}_{(n)}\cdot\Re_{n}$$

- (5) Compute $c_{\Re(n+1/2)}$, the rotated elastic operator at $t_{n+1/2}$. If the material is isotropic, $c_{\Re} = c$; Otherwise, $c_{\Re(n+1/2)} = \left[Q(\Re_{n+1/2})\right]^{T}\left[c\right]\left[Q(\Re_{n+1/2})\right]$

- (6) Return mapping algorithm in the rotated configuration to compute

$$\boldsymbol{\tau}_{\Re(n+1)} = \boldsymbol{\tau}_{\Re(n)} + \mathbf{c}_{\Re(n+1/2)} : \left(\Delta\boldsymbol{\varepsilon}_{\Re(n+1/2)} - \Delta\boldsymbol{\varepsilon}_{\Re(n+1/2)}{}^{p}\right)$$

In this rotated format, the equations and the algorithm are identical to those for infinitesimal elasto-plasticity which will be explained in detail in the Chapter 5.

- (7) Compute the rotated algorithmic tangent operator $c^{alg}_{\Re(n+1)}$

- (8) Rotate back the stress and elasto-plastic tangent (and any other variables if they exist) at t_{n+1}

$$\boldsymbol{\tau}_{(n+1)} = \Re_{n+1} \cdot \boldsymbol{\tau}_{\Re(n+1)} \cdot \Re^{T}_{n+1}$$

$$\left[c^{alg}_{n+1}\right] = \left[Q(\Re_{n+1})\right]\left[c^{alg}_{\Re(n+1)}\right]\left[Q(\Re_{n+1})\right]^{T}$$

- (9) Obtain the Cauchy stress

$$\boldsymbol{\sigma}_{n+1} = \boldsymbol{\tau}_{n+1} / J_{n+1}$$

This algorithm obey the notion of incremental objectivity, which was formalized by Hughes and Winget (1980) and which means that under a rigid body motion, the strain increment must vanish and spurious stresses are precluded. This algorithm has been implemented into a computational module to test the simple shear example stated previous. Figure 5 shows the computation result from this algorithm. The comparison with the analysis solution of simple shear under different objective stress rate indicates very good agreement.

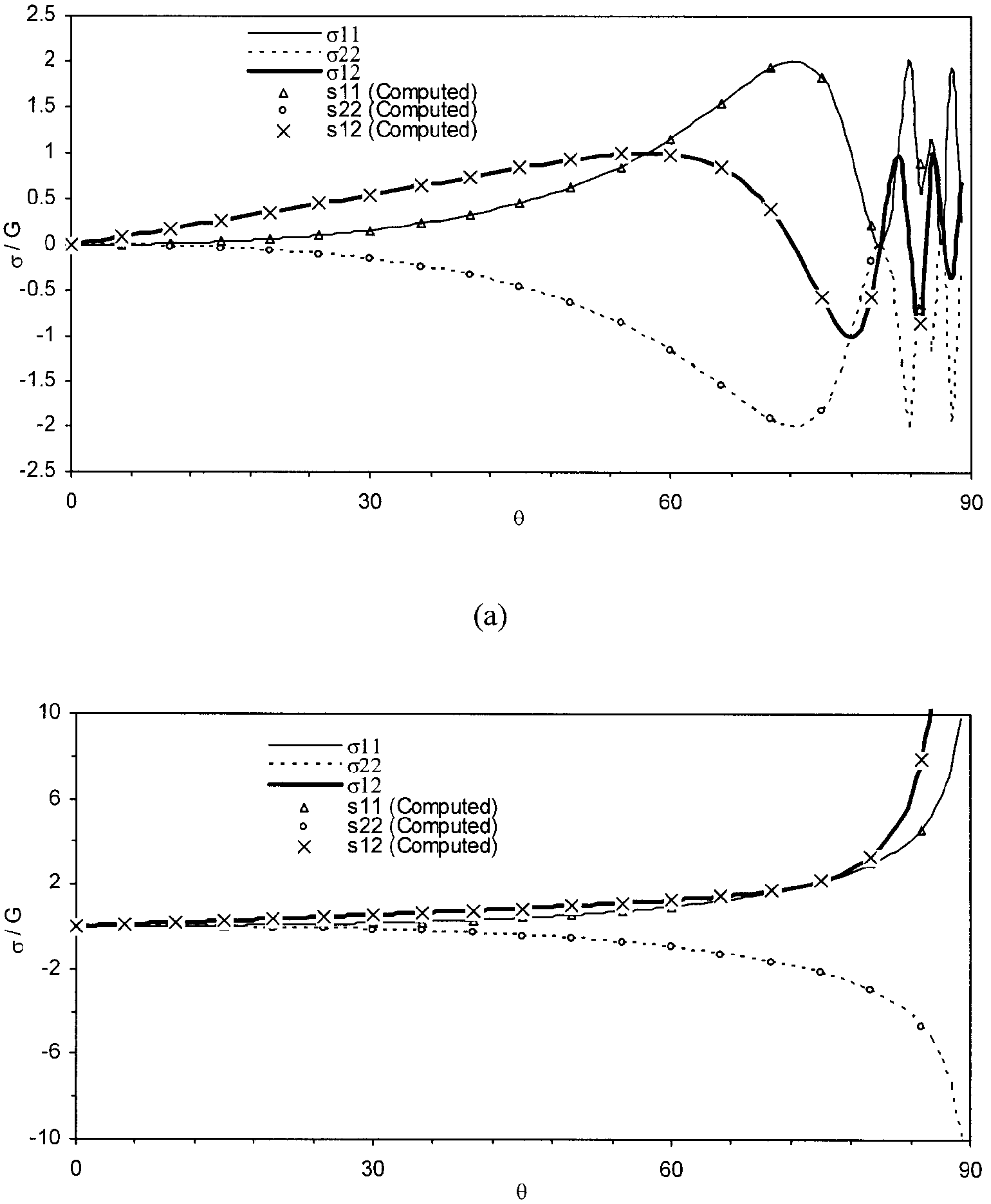

(a)

(b)

Figure 4-5. Comparison of finite strain algorithm implementation with the analytical solution of simple shear problem. (a). Jaumann stress rate. (b). Green-McInnis stress rate.

4.7 Conclusion

For large displacement analysis, the finite strain theory has been introduced to account for the large strain or large rotation for geometries nonlinearaity and material nonlinearity in finite element analysis. The basic formulation of deformation and motion is been reviewed. We confine our attention to the strain and stress measures that are most frequently employed in nonlinear finite element programs: the Green strain tensor and the rate of deformation. Different stress measures have been investigated. The objective rates, also called frame-invariant rates, of the Cauchy stress tensor are examined. The general algorithm for finite strain elasto-plasticity is investigated based on return mapping algorithm and mid-point rule ingeneration. Two type of rotation configuration are used to keep the incremental objectivity of the system. The computation result shows excellent agreement with analytical solution.

5 NONLINEAR FINITE ELEMENT ANALYSIS OF EARTHQUAKE-INDUCED DEFORMATION

5.1 Introduction

Nonlinear constitutive model and finite element analysis can be combined to predict liquefaction-induced permanent ground deformation numerically. This approach involves the use of elasto-plastic models of soil behavior under cyclic loading. The models are generally based on kinematic hardening theory of plasticity. The saturated soil is simulated as a two-phase material using Biot's coupled equations for the soil and water phases. These constitutive models are complex and incorporate parameters that are not usually measured in field and laboratory testing. Typical elasto-plastic model for liquefaction induced ground deformation analysis are used in DYNAFLOW (Prevost 1995), DYSAC2 (Muraleetharan et al. 1988), SWANDYNE4 (Zienkiewicz et al. 1990) and TARA-3 (Finn et al. 1986).

When the shear strength of the liquefied soil is slightly lower than the shear stress applied by gravity force, permanent deformations are likely to be small. If the difference between shear strength and applied shear stress is large, very large deformations may develop. Accurate evaluation of the effects of liquefaction-induced instability requires accurate estimation of the shear strength of liquefied soil. Meanwhile, reduced modulus plays an important role in the analyses (e.g., Finn 1998). The small-deformation formulation of finite element analyses gives unrealistically large displacement when the shear modulus is made extremely small (Towhata, et al. 1997). The small-strain formulation does not take into account the fact that the gravity-induced shear stress decreases with the development of deformation. When the deformation is large, the use of a large-deformation formulation is therefore significantly important.

In this chapter, the algorithm for J2 elasto-plasticity model in large strain will be introduced firstly. The return mapping algorithm for numerical integration is also explained for the rate constitutive equations. The third section formulates the strong and weak formulation of boundary value problems in the large deformation regime with both the material and geometry nonlinearities. The explicit dynamic scheme, which is used to solve the nonlinear soil system after liquefaction, is explained in the fourth section. The implementation of the finite strain FE approach is tested by simulating the single element test and the slump test procedure as explained in fifth section. In the sixth section, the analysis is applied to simulate the post-liquefaction ground deformation of the Upper San Fernando Dam after the 1971 San Fernando Earthquake. The discussion and conclusion about the proposed numerical method are presented in the last section

5.2 Simplified model for ground deformation analysis

Instability occurs when the applied shear stresses exceed the shear strength required to maintain equilibrium of the soil deposit. The soil then deforms until it reaches a configuration in which the shear stresses is less than the shear strength. The amount of deformation required to reach a stable configuration is influenced by the difference between the shear stresses and the shear strength of the liquefied soil.

Very few analyses account for the gravity effects caused by large amount of deformation, i.e., change in gravity-induced shear stress decrease with the development of deformation. The present research studies the ground deformation after earthquake by considering the change of gravity-induced shear stress as shown in Figure 1. The soil system is initially in a stable condition before the earthquake. After strong earthquake shaking, a portion of the soil liquefied and lost certain amount of the shear strength, or even lost the shear strength totally. The soil system is melted and tries to stabilize itself in another stage of equilibrium based on the new shear strength level. At the meantime, the geometrical change because of soil movement also decreases the gravity-induced shear stress. The time when the soil movement will be stop is depending on the balance of reduced shear strength and shear stress from gravity change. The final lateral movement of ground can be obtained by solving these two equilibrium states.

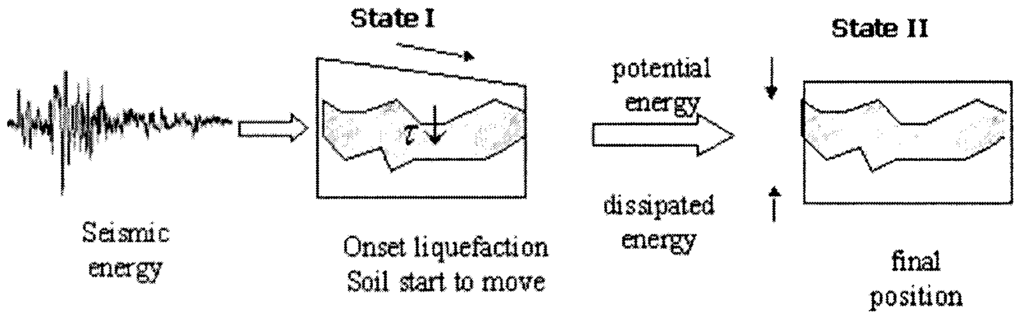

Figure 5-1. **Schematic of two equilibrium states considering the change of gravity induced shear stress due to ground deformation.**

The nonlinear finite element in large deformation is implemented to evaluate these two states of system equilibrium. The transition from the initial configuration to the final equilibrium state is simulated using an explicit dynamic analysis, which accounts for kinetic energy. Liquefied soils are assumed to deform in undrained conditions, and are modeled using J2 elasto-plasticity, objective stress rate, Lagarangian strain field, and hypoelastical additive theory (e.g., Simo and Hughes 1998).

5.3 Algorithm for finite strain J2 elasto-plasticity model

For rate-independent elasto-plasticity, inelastic response can be studied using rate constitutive equations (Liu et al. 1998, Simo and Hughes 1998). The return mapping algorithm provides an effective and robust integration scheme for the rate constitutive equations over a discrete sequence of time steps.

5.3.1 Associative plasticity with nonlinear hardening rules

The von-Mises yield criterion or J2 model can be written as

$$f(\boldsymbol{\sigma},\boldsymbol{\alpha},\kappa) = J_2(\boldsymbol{\sigma},\boldsymbol{\alpha}) - \kappa^2(\bar{e}^p) = 0 \tag{5-1}$$

$$J_2 = \frac{1}{2}|\boldsymbol{\xi}|^2 = \frac{1}{2}\xi_{ij}\xi_{ij}, \; \boldsymbol{\xi} = \mathbf{s} - \boldsymbol{\alpha} \tag{5-2}$$

$$\bar{e}^p = \int_0^t \sqrt{\frac{2}{3}} \left\| \dot{\boldsymbol{\varepsilon}}^p(\tau) \right\| d\tau \tag{5-3}$$

Here, $\boldsymbol{\sigma}$ is the Cauchy stress; κ is a parameter defining the size of the yield surface; $\dot{\boldsymbol{\varepsilon}}^p$ is the plastic strain rate and is $\bar{e}^p$ called the equivalent plastic strain; $\boldsymbol{\alpha}$ is the back-stress; $\mathbf{s}$ is the deviatoric stress of $\boldsymbol{\sigma}$ and defined as

$$\mathbf{s} = \boldsymbol{\sigma} - \frac{1}{3} tr(\boldsymbol{\sigma})\mathbf{1} \tag{5-4}$$

The evolution equations for this model are given as follows (Liu et al. 1998, Simo and Hughes 1998):

$$\dot{\boldsymbol{\sigma}} = \mathbf{C}^e : \left(\dot{\boldsymbol{\varepsilon}} - \dot{\boldsymbol{\varepsilon}}^p\right) \tag{5-5}$$

$$\dot{\boldsymbol{\alpha}} = \frac{2}{3} H_\alpha^{'}(\bar{e}^p)\dot{\boldsymbol{\varepsilon}}^p \tag{5-6}$$

$$\dot{\kappa} = \frac{1}{\sqrt{3}} \kappa'\left(\bar{e}^p\right)\dot{\bar{e}}^p \tag{5-7}$$

$\mathbf{C}^e$ is the fourth-order elastic modulus tensor,

$$\mathbf{C}^e = \lambda \mathbf{1} \otimes \mathbf{1} + 2\mu \mathbf{I} \tag{5-8}$$

where λ, μ are lame parameters, and $\mathbf{1}$ are $\mathbf{I}$, respectively, the second-order unit tensor and fourth-order unit tensor. $\kappa\left(\bar{e}^p\right)$ and $H_\alpha\left(\bar{e}^p\right)$ represent the hardening rules for the radius of the yield surface and the translation of the back stress, respectively.

Under the associative flow rule assumption, the plastic strain rate vector is normal to the yield surface function; define the unit vector normal to the yield surface as,

$$\mathbf{n} = \frac{\partial f}{\partial \boldsymbol{\sigma}} \Bigg/ \left\| \frac{\partial f}{\partial \boldsymbol{\sigma}} \right\| = \xi / \|\xi\| \tag{5-9}$$

the plastic strain rate can be written as

$$\dot{\boldsymbol{\varepsilon}}^p = \begin{cases} \gamma \mathbf{n}, & for\ plastic\ process \\ 0, & for\ elastic\ process \end{cases} \tag{5-10}$$

where γ is a parameter for plastic strain rate and determined by the consistency condition.

Using the consistency condition (i.e., upon yielding the stress point must remain on the yield surface if no unloading occurs), we have

$$\gamma = \left\| \dot{\boldsymbol{\varepsilon}}^p \right\| = \frac{\mathbf{n} : \dot{\boldsymbol{\sigma}}^{tr}}{2\mu\left(1 + \dfrac{\kappa' + H_\alpha^{'}}{3\mu}\right)} = \frac{\mathbf{n} : \dot{\boldsymbol{\varepsilon}}}{1 + \dfrac{\kappa' + H_\alpha^{'}}{3\mu}} \tag{5-11}$$

where $\dot{\boldsymbol{\sigma}}^{tr}$ is a trial stress rate, $\dot{\boldsymbol{\sigma}}^{tr} = \mathbf{C}^e : \dot{\boldsymbol{\varepsilon}}$. We obtain an evolution equation for stress in terms of the total strain rate

$$\dot{\boldsymbol{\sigma}} = \mathbf{C}^{ep} : \dot{\boldsymbol{\varepsilon}} \tag{5-12}$$

where $\mathbf{C}^{ep}$ is a fourth-order constitutive tensor which is referred as the continuum elasto-plastic moduli. It can be written explicitly as

$$\mathbf{C}^{ep} = \lambda \mathbf{1} \otimes \mathbf{1} + 2\mu \mathbf{I} - 2\mu \Lambda \mathbf{n} \otimes \mathbf{n} \tag{5-13}$$

where $\Lambda = \dfrac{1}{1 + \dfrac{\kappa' + H_\alpha^{'}}{3\mu}}$

5.3.2 Radial return algorithm

The radial return algorithm appears to be superior over other projection schemes for numerically integrating the elasto-plastic constitutive equation of the J2 model (Ortiz and Simo 1984, Simo and Hughes 1998). At the end of a typical time step $[t_n, t_{n+1}]$, the unit vector normal to the yield surface can be written as

$$\mathbf{n} = \frac{\partial f}{\partial \boldsymbol{\sigma}} \Bigg/ \left\| \frac{\partial f}{\partial \boldsymbol{\sigma}} \right\| = \boldsymbol{\xi}_{n+1} / \left\| \boldsymbol{\xi}_{n+1} \right\| \tag{5-14}$$

where

$$\boldsymbol{\xi}_{n+1} = \mathbf{s}_{n+1} - \boldsymbol{\alpha}_{n+1} \tag{5-15}$$

Using the mid-point rule, the equivalent plastic strain becomes

$$\bar{e}^{p}_{n+1} = \bar{e}^{p}_{n} + \int_{t_n}^{t_{n+1}} \sqrt{\frac{2}{3}} \left\| \dot{\boldsymbol{\varepsilon}}^{p}(\tau) \right\| d\tau = \bar{e}^{p}_{n} + \sqrt{\frac{2}{3}} \Delta\gamma \tag{5-16}$$

Let $\Delta\boldsymbol{\varepsilon}$ denote the strain increment, the stress at the end of the step is computed from the trial elastic stress $\boldsymbol{\sigma}^{tr}$

$$\boldsymbol{\sigma}_{n+1} = \boldsymbol{\sigma}^{tr}_{n+1} - 2\mu\Delta\gamma\mathbf{n}, \ \boldsymbol{\sigma}^{tr}_{n+1} = \boldsymbol{\sigma}_{n} + \mathbf{C}^{e} : \Delta\boldsymbol{\varepsilon} \tag{5-17}$$

and the deviatoric stress is updated by

$$\mathbf{s}_{n+1} = \mathbf{s}^{tr}_{n+1} - 2\mu\Delta\gamma\mathbf{n}, \ \mathbf{s}^{tr}_{n+1} = \mathbf{s}_{n} \tag{5-18}$$

also for

$$\begin{aligned} \alpha_{n+1} &= \alpha_{n} + \frac{2}{3} H'_{\alpha}\left(\bar{e}^{p}_{n+1/2}\right) \Delta\gamma\mathbf{n} \\ &= \alpha_{n} + \sqrt{\frac{2}{3}} \left[H_{\alpha}\left(\bar{e}^{p}_{n+1}\right) - H_{\alpha}\left(\bar{e}^{p}_{n}\right) \right] \mathbf{n} = \alpha_{n} + \sqrt{\frac{2}{3}} \Delta H_{\alpha} \mathbf{n} \end{aligned} \tag{5-19}$$

We have

$$\boldsymbol{\xi}_{n+1} = \mathbf{s}_{n+1} - \boldsymbol{\alpha}_{n+1} = \boldsymbol{\xi}^{tr}_{n+1} - \left[2\mu\Delta\gamma + \sqrt{\frac{2}{3}} \Delta H_{\alpha} \right] \mathbf{n} \tag{5-20}$$

where

$$\boldsymbol{\xi}^{tr}_{n+1} = \mathbf{s}^{tr}_{n+1} - \boldsymbol{\alpha}_{n} \tag{5-21}$$

so the unit normal is determined in terms of the trial elastic stress ξ_{n+1}^{tr}

$$\mathbf{n} = \xi_{n+1}^{tr} \Big/ \left\| \xi_{n+1}^{tr} \right\| \tag{5-22}$$

and the enforcement of the consistency condition reduces to a scalar equation which can be solved numerically:

$$g(\Delta\gamma) = -\sqrt{2}\kappa\left(\bar{e}_{n+1}^{p}\right) + \left\| \xi_{n+1}^{tr} \right\| - \left[2\mu\Delta\gamma + \sqrt{\frac{2}{3}}\Delta H_{\alpha} \right] = 0 \tag{5-23}$$

The value of the plastic strain increment parameter $\Delta\gamma$, can be determined from the above equation for any given functions $\kappa\left(\bar{e}^{p}\right)$ and $H_{\alpha}\left(\bar{e}^{p}\right)$. The solution of the equation may be accomplished by a local Newton iteration procedure.

For linear isotropic hardening rules, the consistency condition reduces to the equation as following,

$$\Delta\gamma = \frac{\left\| \xi_{n+1}^{tr} \right\| - \sqrt{2} K \bar{e}_{e}^{p}}{2\mu\left(1 + \frac{K}{3\mu}\right)} \tag{5-24}$$

Table 1 summarizes the return mapping algorithm for J2 plasticity under linear isotropic hardening for the rotated configuration which already described in Chapter 4 (See section 4.6.5 for detail).

Table 5-1. Return mapping algorithm for J2 plasticity with linear isotropic hardening.

In the rotated format (as defined in section 4.6.5), the equations and the algorithm are identical to those for infinitesimal elasto-plasticity,

```
1. trial (rotated) stress $\boldsymbol{\tau}^{tr}_{\Re(n+1)} = \boldsymbol{\tau}_{\Re(n)} + \mathbf{c}_{\Re(n+1/2)} : \Delta\boldsymbol{\varepsilon}_{\Re(n+1/2)}$
2. deviatoric stress $\boldsymbol{\tau}\mathbf{n} = \boldsymbol{\tau}^{tr}_{\Re(n+1)} - \frac{1}{3} tr(\boldsymbol{\tau}^{tr}_{\Re(n+1)})$
3. $J_2 = \left\| \frac{1}{2} \boldsymbol{\tau}\mathbf{n} : \boldsymbol{\tau}\mathbf{n} \right\|$
4. $f^{tr}_{n+1} = J_2 - \sqrt{2}(\sigma_Y + K\overline{e}^{p}_{n})$
5. If $f^{tr}_{n+1} < 0$ then
        set $(\bullet)_{n+1} = (\bullet)^{tr}_{n+1}$ & Exit
6. Else
        $\Delta\gamma = \frac{\langle f^{tr}_{n+1} \rangle / 2\mu}{1 + K / 3\mu}$
        $\mathbf{n}_{n+1} = \boldsymbol{\tau}\mathbf{n} / J_2$
        $\boldsymbol{\tau}_{n+1} = \boldsymbol{\tau}^{tr}_{\chi(n+1)} - 2\mu\Delta\gamma\mathbf{n}_{n+1}$
        $\overline{e}^{p}_{n+1} = \overline{e}^{p}_{n} + \sqrt{\frac{2}{3}}\Delta\gamma$
   End if
```

5.4 Strong and weak forms with material and geometrical nonlinearitis

Once the constitutive model and the kinematics have been defined, boundary value problems may be examined. Initially composed of nonlinear partial differential equations and of boundary conditions, the strong formulation is transformed into a variational problem and discretized into finite elements. The variational formulation, which takes into account material and geometrical nonlinearities, was introduced according to work done by McMeeking and Rice (1974).

5.4.1 Strong form of equation of motion in initial configuration

The boundary value problem of Fig. 2 may be stated in the initial configuration using the following strong formulation:

Find the displacement field $\mathbf{u}(\mathbf{X},t)$ of point $\mathbf{X}$ at time t so that:

$$\frac{\partial \Sigma_{ji}}{\partial X_j} + f_i - \rho_0 \frac{d^2 u_i}{dt^2} = 0, \ \forall\, \mathbf{X} \in \Omega_0 \tag{5-25}$$

$$\Sigma_{ij} N_j = h_i^0, \ \forall\, \mathbf{X} \in \Gamma_h^0 \quad \text{(prescribed traction)} \tag{5-26}$$

$$u_i = g_i^0, \ \forall\, \mathbf{X} \in \Gamma_g^0 \quad \text{(prescribed displacement)} \tag{5-27}$$

where

Σ	nonsymmetric first Piola Kirchhoff stress tensor
$\mathbf{f}(\mathbf{X},t)$	body force per unit volume at time t and at point $\mathbf{X}$
$\rho_0(\mathbf{X})$	mass per unit volume at point $\mathbf{X}$
Ω_0	initial configuration of solid
Γ_0	boundary of Ω_0 : $\Gamma_0 = \Gamma_g^0 \cup \Gamma_h^0$
Γ_h^0	part of boundary Γ_0 with prescribed traction
$\mathbf{h}_0(\mathbf{X},t)$	prescribed traction at time t at $\mathbf{X}$ on Γ_h^0
$\mathbf{N}$	unit vector normal to boundary Γ_0
Γ_g^0	part of boundary Γ_0 with prescribed displacement
$\mathbf{g}_0(\mathbf{X},t)$	prescribed displacement at time t at point $\mathbf{X}$ on Γ_g^0

The boundary value problem of Fig. 2 may be restated in the initial configuration in terms of rates: Find the velocity field $\dot{\mathbf{u}}(\mathbf{X},t)$ of point **X** at time *t*, such that:

$$\frac{\partial \dot{\Sigma}_{ji}}{\partial X_j} + \dot{f}_i - \rho_0 \frac{d^2 \dot{u}_i}{dt^2} = 0 \,,\ \forall\ \mathbf{X} \in \Omega_0 \tag{5-28}$$

$$\dot{\Sigma}_{ij} N_j = \dot{h}_i^0 \,,\ \forall\ \mathbf{X} \in \Gamma_h^0 \quad \text{(prescribed traction)} \tag{5-29}$$

$$\dot{u}_i = \dot{g}_i^0 \,,\ \forall\ \mathbf{X} \in \Gamma_g^0 \quad \text{(prescribed velocity)} \tag{5-30}$$

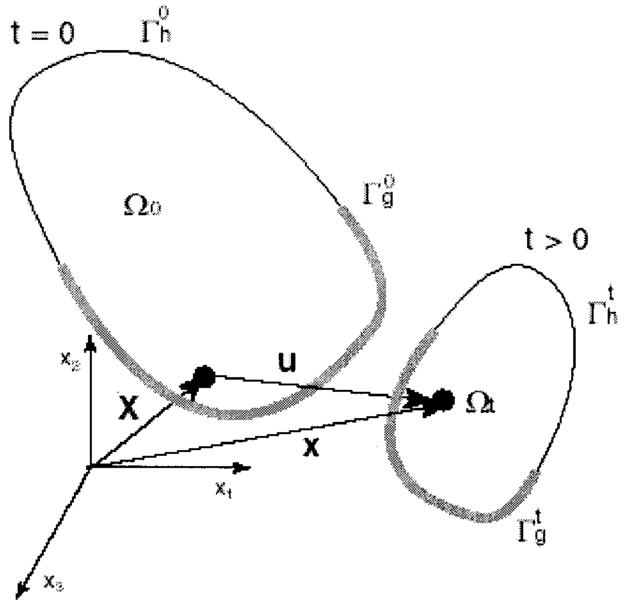

Figure 5-2. **Geometry of a boundary value problem (initial and present configuration of a body).**

5.4.2 Weak form in initial configuration

The boundary value problem of Eq. 25, which consists of nonlinear partial differential equations and boundary conditions, can be stated as a weak form using variational calculus (Hughes 1984).

By definition, the variational displacement field **w(X)** satisfies zero displacement boundary conditions on Γ_g^0 and is differentiable within the material volume Ω_0. $\mathcal{W}_0$ denotes the space of all variational fields **w(X)**, i.e.:

$$\mathcal{W}_0 = \{\mathbf{w}, \mathbf{w}(\mathbf{X}) = 0 \text{ on } \Gamma_g^0\} \tag{5-31}$$

$\mathcal{W}_0$ has for spatial dimension $n_{sd} = 2$ for plane-strain or axisymmetric problems and $n_{sd} = 3$ for three-dimensional problems. The weak form in the initial configuration is to find the displacement field **u**(**X**,*t*) that satisfies the prescribed displacement conditions $\forall\ \mathbf{w} \in \mathcal{W}_0$. Eq. 25 becomes:

$$\int_{\Omega_0} \rho_0 \frac{d^2 u_i}{dt^2} w_i d\Omega_0 + \int_{\Omega_0} \Sigma_{ji} \frac{\partial w_i}{\partial X_j} d\Omega = \int_{\Gamma_0} h_i^0 w_i d\Omega_0 + \int_{\Omega_0} f_i w_i d\Omega_0 \quad \forall \mathbf{w} \in W_0 \tag{5-32}$$

Eq. 32 holds at times $t+\Delta t$:

$$\begin{aligned} &\int_{\Omega_0} \rho_0 \frac{d^2 u_i(t+dt)}{dt^2} w_i d\Omega_0 + \int_{\Omega_0} \Sigma_{ji}(t+dt) \frac{\partial w_i}{\partial X_j} d\Omega \\ &= \int_{\Gamma_0} h_i^0(t+dt) w_i d\Omega_0 + \int_{\Omega_0} f_i(t+dt) w_i d\Omega_0 \end{aligned} \tag{5-33}$$

The increments of Piola-Kirchhoff stress tensor and displacement are respectively between time t and $t+\Delta t$:

$$\Delta\Sigma_{ji} = \Sigma_{ji}(t+\Delta t) - \Sigma_{ji}(t) \tag{5-34}$$

Substitute into Eq. 33:

$$\begin{aligned}&\int_{\Omega_0} \rho_0 \frac{d^2 u_i(t+dt)}{dt^2} w_i d\Omega_0 + \int_{\Omega_0} \Delta\Sigma_{ji} \frac{\partial w_i}{\partial X_j} d\Omega_0 \\ &= \int_{\Gamma_0} h_i^0(t+dt) w_i d\Omega_0 + \int_{\Omega_0} f_i(t+dt) w_i d\Omega_0 - \int_{\Omega_0} \Sigma_{ji}(t) \frac{\partial w_i}{\partial X_j} d\Omega_0\end{aligned} \tag{5-35}$$

If the time is discretized in time steps t_n where n varies from 0 to N. The increments of Piola-Kirchhoff stress tensor from time t_n to time t_{n+1} is:

$$\Delta\Sigma_{ji}^{n+1} = \Sigma_{ij}^{n+1} - \Sigma_{ji}^{n} \tag{5-36}$$

We will end up with the following equation:

$$\begin{aligned}&\int_{\Omega_0} \rho_0 \frac{d^2 u_i^{n+1}}{dt^2} w_i d\Omega_0 + \int_{\Omega_0} \Delta\Sigma_{ji} \frac{\partial w_i}{\partial X_j} d\Omega_0 \\ &= \int_{\Gamma_0} h_i^{0,n+1} w_i d\Omega_0 + \int_{\Omega_0} f_i^{0,n+1} w_i d\Omega_0 - \int_{\Omega_0} \Sigma_{ji}^{n} \frac{\partial w_i}{\partial X_j} d\Omega_0\end{aligned} \tag{5-37}$$

Related the unit masses to the Jacobian of transformation through:

$$\frac{\rho_0}{\rho} = \frac{d\Omega_t}{d\Omega_0} = J = \det[\mathbf{F}] \tag{5-38}$$

where ρ_0 is the mass per unit volume at $t = 0$, and ρ is the mass per unit volume at time t. The integrals of Eq. 38 can be evaluated in the deformed configuration Ω_t and its deformed boundary Γ_t, i.e.:

$$\begin{aligned}&\int_{\Omega_0} \rho_0 \frac{d^2 u_i^{n+1}}{dt^2} w_i d\Omega_0 - \int_{\Gamma_0} h_i^{0,n+1} w_i d\Gamma_0 + \int_{\Omega_0} f_i^{0,n+1} w_i d\Omega_0 \\ &= \int_{\Omega_{n+1}} \rho \frac{d^2 u_i^{n+1}}{dt^2} w_i d\Omega_{n+1} - \int_{\Gamma_{n+1}} h_i^{n+1}{}_i w_i d\Gamma_{n+1} + \int_{\Omega_{n+1}} f_i^{n+1} / J \, w_i d\Omega_{n+1}\end{aligned} \tag{5-39}$$

Recall the relations between different stress measurements from Chapter 4 (see Table 4-1), we will have:

$$\int_{\Omega_0} \Sigma^n_{ji} \frac{\partial w_i}{\partial X_j} d\Omega_0 = \int_{\Omega_0} \tau^n_{ki} \frac{\partial w_i}{\partial X_j} \frac{\partial X_j}{\partial x_k} d\Omega_0 = \int_{\Omega_n} \frac{\tau^n_{ki}}{J} \frac{\partial w_i}{\partial x_k} d\Omega_n = \int_{\Omega_n} \sigma^n_{ki} w_{(i,k)} d\Omega_n \tag{5-40}$$

The increments of Piola-Kirchhoff stress tensor from time t_n to time t_{n+1} is assumed proportional to its rate, i.e.:

$$\Delta\Sigma_{ji} = \dot{\Sigma}_{ij} dt \tag{5-41}$$

The velocity is related to the incremental displacement $\Delta\mathbf{u}_n$ from time t_n to time t_{n+1} through:

$$\Delta\mathbf{u}_n = \mathbf{v}_n dt \text{ i.e., } \Delta u_i^n = v_i^n dt \tag{5-42}$$

where $\Delta\mathbf{u}_{n+1}$ is the incremental displacement from times t_n to t_{n+1}:

$$\Delta\mathbf{u}_{n+1} = \mathbf{u}_{n+1} - \mathbf{u}_n \quad \text{i.e., } \Delta u_i^{n+1} = u_i^{n+1} - u_i^n \tag{5-43}$$

Recalling the following relation between stress rates:

$$\dot{\Sigma}_{ji} = \frac{\partial X_j}{\partial x_k}\left(\widehat{\tau}_{ki} + \tau_{kl} \frac{\partial v_l}{\partial x_i}\right) \tag{5-44}$$

We can find that

$$\begin{aligned} \int_{\Omega_0} \Delta\Sigma_{ji} \frac{\partial w_i}{\partial X_j} d\Omega_0 &= \int_{\Omega_t} \left(\frac{1}{J} \widehat{\tau}_{ki} \Delta t + \sigma_{kl} \frac{\partial \Delta u_l}{\partial x_i} \right) \frac{\partial w_i}{\partial x_k} d\Omega_t \\ &= \int_{\Omega_t} \breve{\sigma}_{ki} \Delta t \frac{\partial w_i}{\partial x_k} d\Omega_t + \int_{\Omega_t} \sigma_{kl} \frac{\partial \Delta u_l}{\partial x_i} \frac{\partial w_i}{\partial x_k} d\Omega_t \end{aligned} \tag{5-45}$$

Introducing the incremental stress-strain relation by using the fourth order constitutive equation:

$$\Delta\sigma_{ij}^{n} = \breve{\sigma}_{ij}^{n}\Delta t = C_{ijkl}^{n+1}\Delta\varepsilon_{kl}^{n+1} = C_{ijkl}^{n+1}\Delta u_{(k,l)}^{n+1} \tag{5-46}$$

The variational equation can be written as,

$$\begin{aligned} &\int_{\Omega_{n+1}} \rho \frac{d^2 u_i^{n+1}}{dt^2} w_i d\Omega + \int_{\Omega_{n+1}} C_{ijkl}^{n+1}\Delta u_{(k,l)}^{n+1} \frac{\partial w_i}{\partial x_j} d\Omega + \int_{\Omega_{n+1}} \sigma_{kl}^{n+1} \frac{\partial \Delta u_l^{n+1}}{\partial x_i} \frac{\partial w_i}{\partial x_k} d\Omega \\ &= \int_{\Gamma_{n+1}} h_i^{n+1}{}_{i} w_i d\Omega + \int_{\Omega_{n+1}} f_i^{n+1}/J\, w_i d\Omega - \int_{\Omega_n} \sigma_{ki}^{n} w_{(i,k)} d\Omega \end{aligned} \tag{5-47}$$

It is convenient to replace second-order tensors with vectors and fourth-order tensor with matrix for two-dimensional, plane-strain, axisymmetric, and three-dimensional cases.

$$C_{ijkl}^{n+1}\Delta u_{(k,l)}^{n+1} w_{(i,j)} = \boldsymbol{\varepsilon}(\mathbf{w})^T \mathbf{D}_{n+1}\, \boldsymbol{\varepsilon}(\Delta\mathbf{u}_{n+1}) \quad \text{and} \quad \sigma_{ij}^{n} w_{(i,j)} = \boldsymbol{\varepsilon}(\mathbf{w})^T \boldsymbol{\sigma}_n \tag{5-48}$$

The space of all variational fields **w**(**x**) is denoted $\mathcal{W}_t$:

$$\mathcal{W}_t = \{\mathbf{w}, \mathbf{w}(\mathbf{x}) = 0 \text{ on } \Gamma_g^t\} \tag{5-49}$$

the weak form becomes: Find the displacement $\mathbf{u}_{n+1} = \mathbf{u}_n + \Delta\mathbf{u}_{n+1}$ which satisfies the boundary conditions on Γ_g so that:

$$\begin{aligned} &\int_{\Omega_{n+1}} \rho \frac{d^2 u_i^{n+1}}{dt^2} w_i d\Omega + \int_{\Omega_{n+1}} \boldsymbol{\varepsilon}(\mathbf{w})^T \mathbf{D}_{n+1}\, \boldsymbol{\varepsilon}(\Delta\mathbf{u}_{n+1}) d\Omega + \int_{\Omega_{n+1}} \sigma_{kl}^{n+1} \Delta u_{l,i}^{n+1} w_{i,k} d\Omega \\ &= \int_{\Gamma_{n+1}} h_i^{n+1}{}_{i} w_i d\Omega + \int_{\Omega_{n+1}} f_i^{n+1}/J\, w_i d\Omega - \int_{\Omega_n} \boldsymbol{\varepsilon}(\mathbf{w})^T \boldsymbol{\sigma}_n d\Omega \end{aligned} \tag{5-50}$$

The large deformation formulation has been implemented in the existing finite element program GEOFEEX, which is developed from LINOS (Bardet 1986). The finite strain J2 plastic model has been added to the GEOFEEX as an independent material module. The original QUAD element has been modified to adopt the large deformation formulation to consider the geometrical nonlinearity. Two types of objective stress rate, Jaumman rate and Green-Naghdi-McInnis are included.

5.5 Computational methods for nonlinear deformation

This section introduces the numerical methods for solving the equilibrium equations for the nonlinear system. Here we use the explicit Newmark algorithms (Hughes 1984, Bardet 1996), which are numerical techniques in finite elements commonly used to solve hyperbolic problems.

5.5.1 Newmark integration schemes

For the equation of motion in a general form

$$\mathbf{Ma} + \mathbf{N}(\mathbf{v},\mathbf{d}) = \mathbf{F}^{ext} \tag{5-51}$$

where $\mathbf{M}$ is the generalized mass matrix, $\mathbf{a}$ the generalized acceleration vector, $\mathbf{v}$ the generalized velocity vector, $\mathbf{d}$ the generalized displacement vector, $\mathbf{N}$ the nonlinear term representing the internal force vector, and the vector of externally applied force. In computational mechanics, $\mathbf{N}$ is usually assumed differentiable. The corresponding tangent stiffness $\mathbf{K}_T$ and tangent damping $\mathbf{C}_T$ are defined as:

$$\mathbf{K}_T = \partial\mathbf{N} / \partial\mathbf{d} \text{ and } \mathbf{C}_T = \partial\mathbf{N} / \partial\mathbf{v} \tag{5-52}$$

The initial conditions complete the discrete equation of motion and form an initial value problem:

$$\mathbf{d}(0) = \mathbf{d}_0 \text{ and } \dot{\mathbf{d}}(0) = \mathbf{v}_0 \tag{5-53}$$

The initial value problem can be solved by time-discretization of Eq. 52. There are several time-discretization algorithms which can be used for this purpose. In this research work, the explicit version of Newmark algorithm is adopted.

The explicit Newmark algorithm is used to decouple the linear system of equation, and avoids the solution of a nonlinear system, which may become singular (Bardet 1996). The basic equation of explicit Newmark algorithm is as follows

$$\mathbf{Ma}_{n+1} + \mathbf{N}(\tilde{\mathbf{v}}_{n+1}, \tilde{\mathbf{d}}_{n+1}) = \mathbf{F}_{n+1}^{ext} \tag{5-54}$$

$$\mathbf{d}_{n+1} = \tilde{\mathbf{d}}_{n+1} = \mathbf{d}_n + \Delta t \mathbf{v}_n + \frac{\Delta t^2}{2} \mathbf{a}_n \tag{5-55}$$

$$\mathbf{v}_{n+1} = \tilde{\mathbf{v}}_{n+1} + \gamma \Delta t \mathbf{a}_{n+1} \tag{5-56}$$

$$\tilde{\mathbf{v}}_{n+1} = \mathbf{v}_n + \Delta t (1 - \gamma) \mathbf{a}_n \tag{5-57}$$

where Δt is the time step, γ is the constant of time integration, $\tilde{\mathbf{v}}_{n+1}$ and $\tilde{\mathbf{d}}_{n+1}$ are so called predictors, and $\mathbf{v}_{n+1}$ and $\mathbf{d}_{n+1}$ are the correctors. The effective stiffness matrix is therefore proportional to the mass matrix:

$$\mathbf{K}^* = \frac{1}{\Delta t^2 \beta} \mathbf{M} \tag{5-58}$$

Here β is the constant of the time integration. Table 2 summarizes the implementation procedure for the explicit Newmark algorithm.

Table 5-2. Explicit Newmark algorithm.

```
1. Initialize
   $\tilde{\mathbf{d}}_{n+1} = \mathbf{d}_n + \Delta t \mathbf{v}_n + \frac{\Delta t^2}{2}\mathbf{a}_n$
   $\tilde{\mathbf{v}}_{n+1} = \mathbf{v}_n + \Delta t(1-\gamma)\mathbf{a}_n$
2. The residual or "out of balance" force is calculated
   $\Delta\mathbf{F} = \mathbf{F}_n^{ext} - \mathbf{N}(\tilde{\mathbf{d}}_n, \tilde{\mathbf{v}}_n)$
3. Solving the linear matrix system for $\mathbf{a}_{n+1}$: $\mathbf{M}\mathbf{a}_{n+1} = \Delta\mathbf{F}$
4. Update solution
   $\mathbf{v}_{n+1} = \tilde{\mathbf{v}}_{n+1} + \gamma\Delta t\mathbf{a}_{n+1}$
   $\mathbf{d}_{n+1} = \tilde{\mathbf{d}}_{n+1}$
5. Execute next time step: $n \leftarrow n+1$, go to step 1.
```

Choosing the $\beta = 0$ and $\gamma = 1/2$, the explicit Newmark algorithm corresponds to the well-known central difference method. The advantage of the explicit formulation is to use the diagonal mass and damping matrix to decouple the equations. The disadvantage of the explicit scheme is that it is conditionally stable. The critical time step for the un-damped explicit scheme is:

$$\Delta t_c = 2/\omega_{\max} \tag{5-59}$$

The critical time step corresponding to the stability limit for the damped case is

$$\Delta t_c = \frac{2}{\omega_{\max}}\left(\sqrt{1+\xi^2} - \xi\right) \tag{5-60}$$

where the damping ratio is in the case of Rayleigh damping:

$$\xi = \frac{a}{2\omega} + \frac{b\omega}{2} \quad \mathbf{C} = a\mathbf{M} + b\mathbf{K} \tag{5-61}$$

5.6 Simulation examples of finite strain computations

Two types of validation problems, single element test and slump test, have been used to examine the implementation of the finite deformation elasto-plastic model.

5.6.1 Single element test

The implementation of the proposed finite strain J2 finite element method in the computer program GEOFEEX was first tested by simulating a single four nodes QUAD element using the explicit dynamic scheme. The boundary condition of this single element is shown in Figure 3. The base of the single element and one side of the element are fixed in vertical and horizontal direction, respectively. The element is 1 m high with Young's modulus 20 mPa and unit weight 20 kN/m^2. The element is allowed to move vertically and horizontally. The deformation of the element will be driven by the self-weight of the material to find the final equivalent position based on assigned shear strength (or radius of failure surface). Constant volume condition is enforced using Poisson's ratio equal to 0.4999.

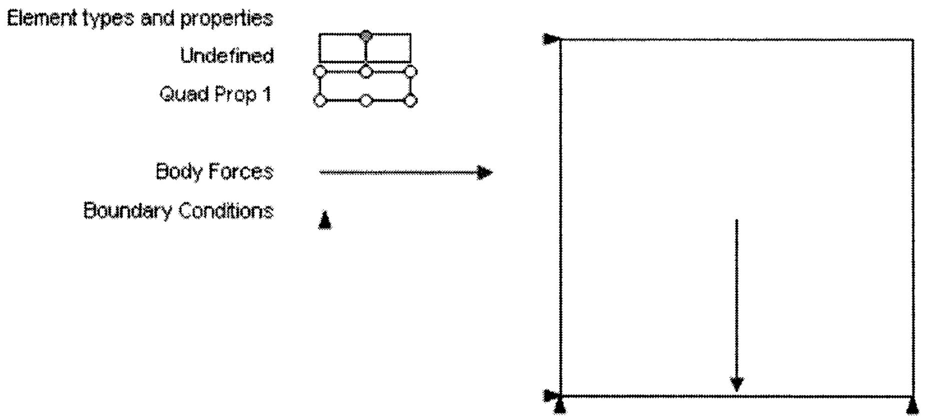

Figure 5-3. Boundary condition of single element test.

The Green-McInnis stress rate is used in this large deformation computation to avoid potential stress oscillation which has been observed in Jaunman stress rate (Dienes 1979). The explicit Newmark computation scheme has been used to find a converged solution for this nonlinear system with very small time step 0.0001 sec. Figure 4 shows the vertical displacement versus different J2 values. The settlement increases dramatically as the J2 value (or shear strength) drops. The element settles 90% of its original height when J2 is close to 2 kPa. It can be seen that the deformation of the single element demonstrates the strong nonlinear behavior. As the J2 value close to the zero, the settlement of the single element almost keeps constant.

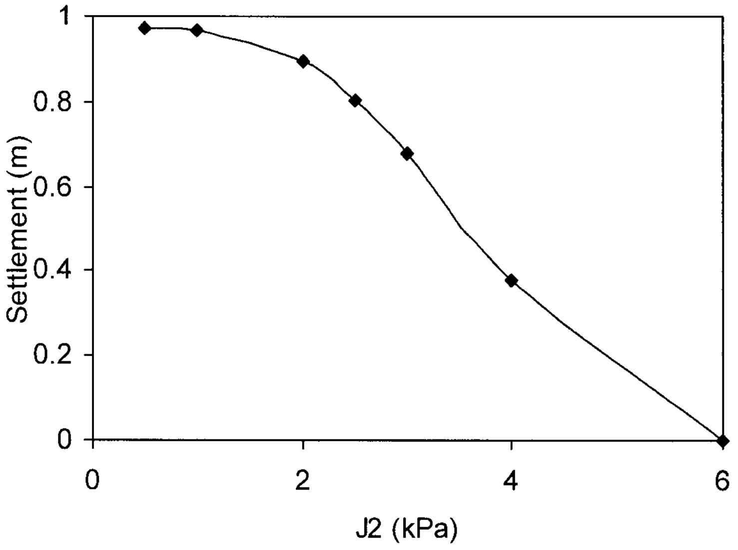

Figure 5-4. Computed vertical settlement versus J2 indicating that the settlement increases with the reduced J2 value.

Figure 5 shows the converged result of horizontal and vertical displacement for J2=4 kPa. After reaching the yield surface, the element finds its new equivalent position while the volume is kept constant. The deformation is stabilized after 1.6 seconds computation. It is impossible to do this type of calculation without large deformation formulation.

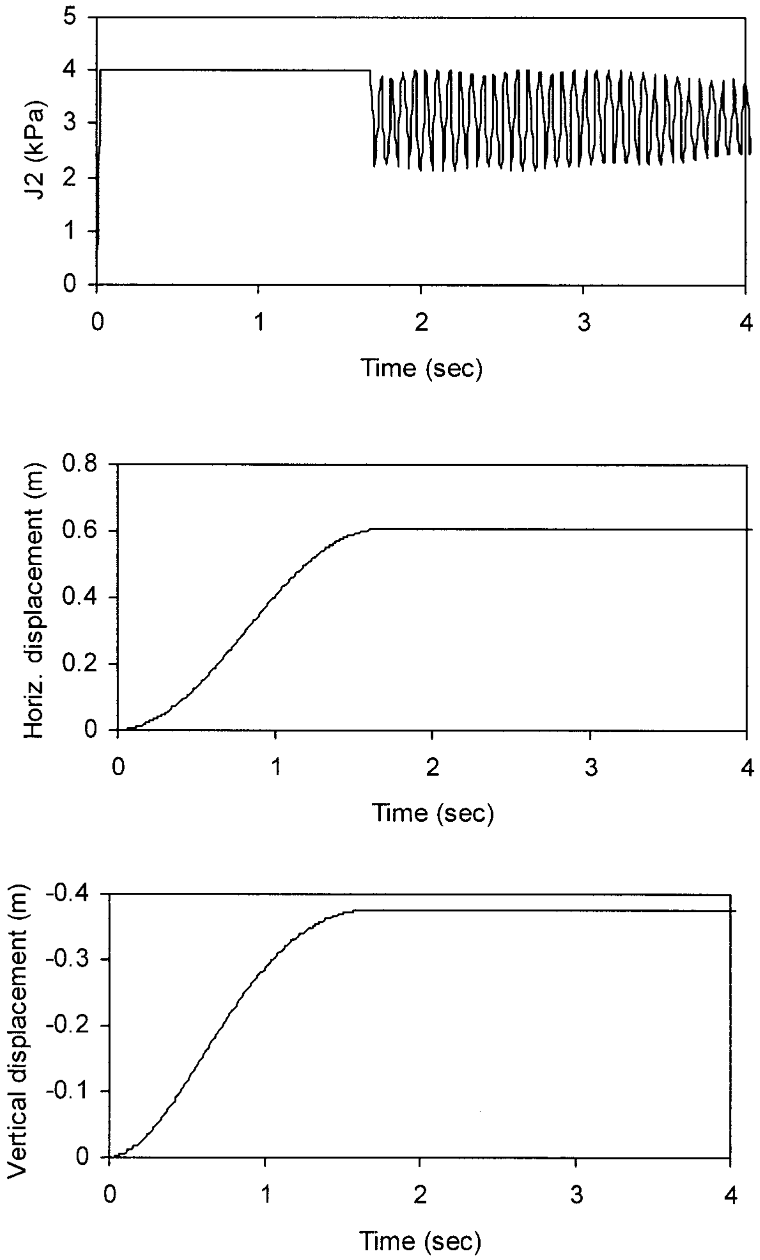

Figure 5-5. Converged result of horizontal and vertical displacement (with J2=4kPa).

5.6.2 Slump test of fresh concrete

The implemented finite element procedure has been used to study the slump test which involves large deformation. The slump test, frequently performed on fresh concrete as a measure of its strength, or ability to flow, is well documented by Tattersall and Banfill (1983). As illustrated schematically in the Figure 6, the slump measurement consists of filling a cylindrical model with the material to be tested in the specified way, lifting the model off and allowing the material to collapse under its gravity. The height of the final deformed, or slumped, concrete is measured. The difference between the initial and final heights is termed the slump height.

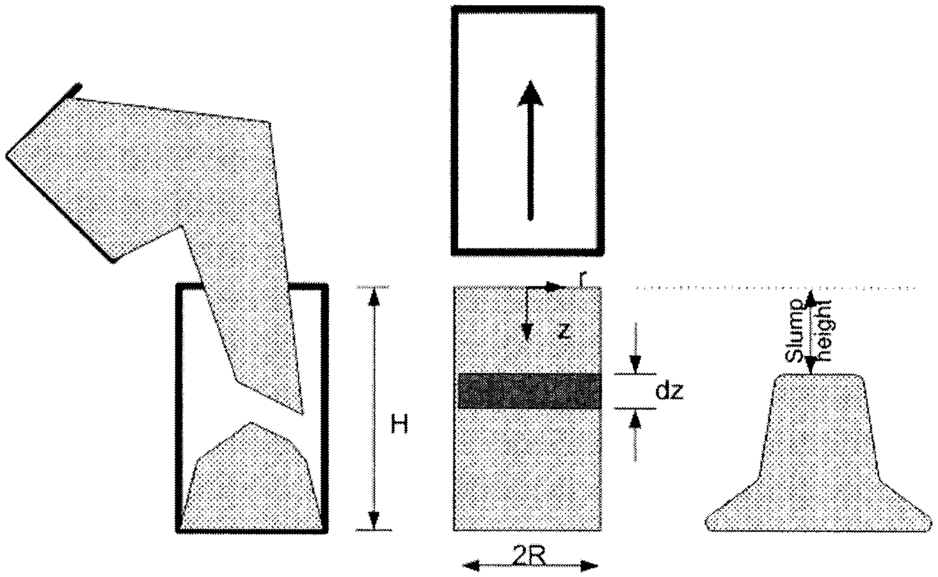

Figure 5-6. Schematic diagram of the slump test showing the slump procedure (after Pashias et al. 1996).

The slump test offers a quick and easy way of measuring the yield stress of strongly flocculated suspensions without the need for sophisticated electronic equipment. The theoretical analysis relating the slump height to the yield stress was first undertaken by Murata (1984) for a conical geometry. Christensen (1991) corrected the simple integration error in the original Murata theory and conducted several experimental tests to verify the analytical solution. The analytical solution of slump test to a circular cylindrical geometry was proposed (Chandler 1986; Pashias et al. 1996). The finite element solution of slump test based on the infinitesimal strain theory was presented by Christensen (1991) and Tanigawa and Mori (1986). The comparison of finite element solution with theoretical results indicates that the classical infinitesimal plasticity approach is not adequate to solve the slump test problem. Famiglietti and Provost (1994) investigate this problem and suggest a finite deformation elasto-plastic model is appropriate to simulate the slump test.

The slump test with a cylindrical geometry has been used as a validation problem of the implemented finite deformation elasto-plastic model in GEOFEEX. The slumping and the corresponding stress profile throughout the material are illustrates in Figure 7. At some point along the height of the undeformed cylinder, the material experiences a stress that is large than the yield stress τ_y. The material flows to another equivalent state. Once the slumping is completed, the stress distribution is identical to that of the undeformed material for the upper non-yielded section, while flow occurs in the remaining material until the stress is reduced to the yield stress. The analytical solution for this model is adopted from Pashias et al. (1996), i.e.

$$s' = 1 - 2\tau_y' \left[1 - \ln(2\tau_y')\right] \tag{5-62}$$

here s' and τ_y' are the dimensionless slump height and yielded stress scaled by γH, respectively.

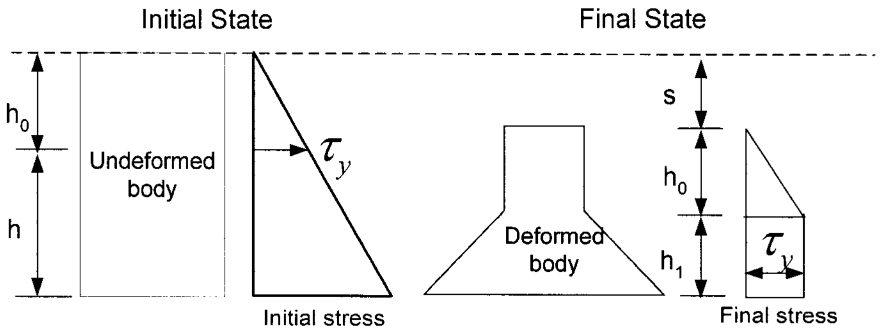

Figure 5-7. **Initial and final states stress distribution of slump test model to determine the analytical solution (after Pashivas et al. 1996).**

The finite element mesh used for the validation of the finite deformation J2 model applied to the slump test consists of 50 four-node axisymmetric elements as shown in Figure 8. Consistent with the axisymmetric specification, nodes along the axis of symmetry were required to remain along the axis throughout the deformation. Hyperbolic analysis is employed with 4 stress points per element.

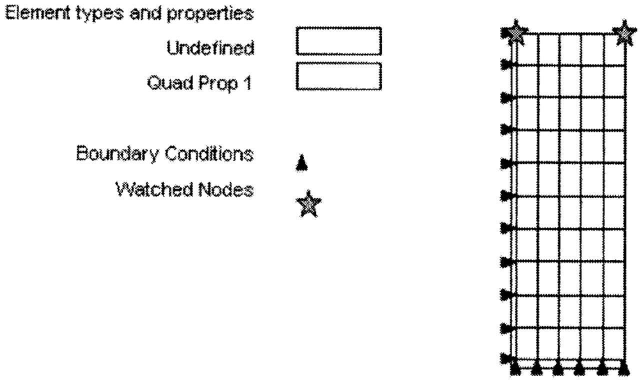

Figure 5-8. **Finite element mesh and boundary condition of simulated slump test.**

The result of nonlinear finite element calculation has been illustrated in the Figure 8 upon with the approximated close form solution in Eq. 62. The result is normalized by the height of the slump. It indicates that at small to medium level deformation the computation has a fair good agreement with the close form solution. In the very large strain range, the finite element provides much more large deformation compared to with the approximate solution. A plot of deformed mesh at dimensionless yield strength at 0.25 is shown in Figure 9 along the displacement vector for each element.

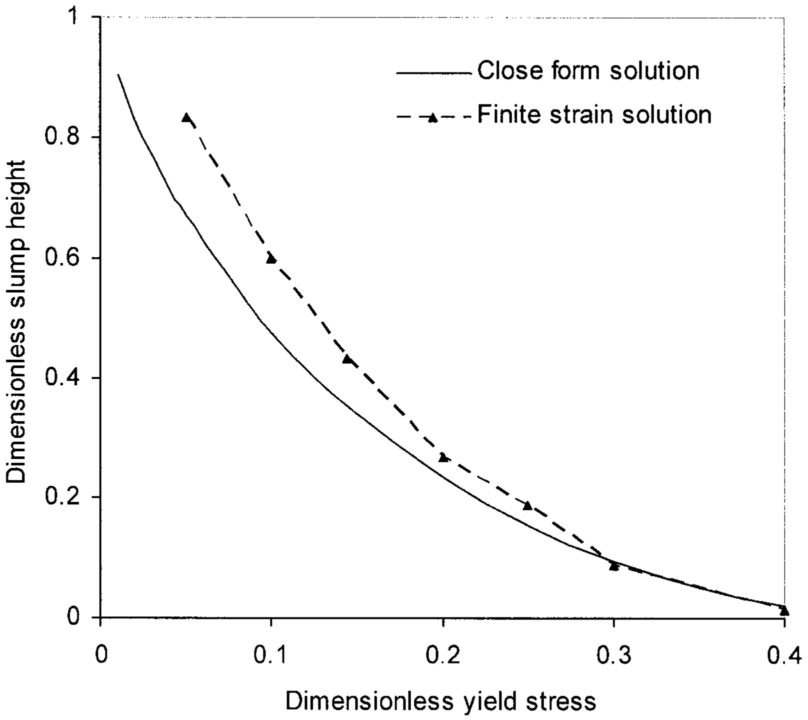

Figure 5-9. Dimensionless yield stress versus dimensionless slump height.

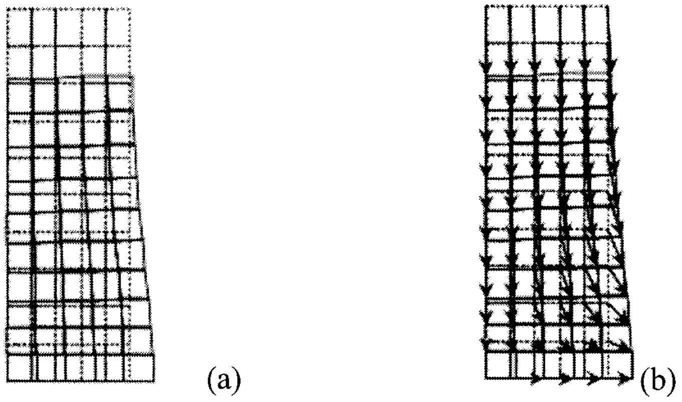

Figure 5-10. Computed result of slump test with dimensionless yield strength 0.25. (a) Deformed and undeformed mesh (Solid line is deformed mesh and dash line is undeformed mesh). (b) Displacement vectors showing the slump flow.

5.7 Evaluation of the Upper San Fernando Dam in the 1971 San Fernando Earthquake

The Upper San Fernando Dam was subjected to strong near source ground motions during the 1971 San Fernando earthquake and the 1994 Northridge earthquake. The implemented finite strain finite element analysis has been applied to simulate the permanent ground deformation of the Upper San Fernando Dam after the 1971 San Fernando earthquake. Post-liquefaction strength and stiffness have been applied to liquefied elements to find the final position of the earth structure.

5.7.1 Background of the Upper San Fernando Dam

The Upper San Fernando Dam (USFD), along with the Lower San Fernando Dam, is owned and operated by Los Angeles Department of Water and Power (LADWP), was one of the important water storage facility located in Van Norman Complex of northeast of Los Angeles as seen in Figure 11. The USFD and LSFD, upon with other structures such as Los Angeles Dam, the Los Angeles Aqueduct Filtration Plant, the High Speed and Bypass Channel, are very critical water facilities to the Los Angels area.

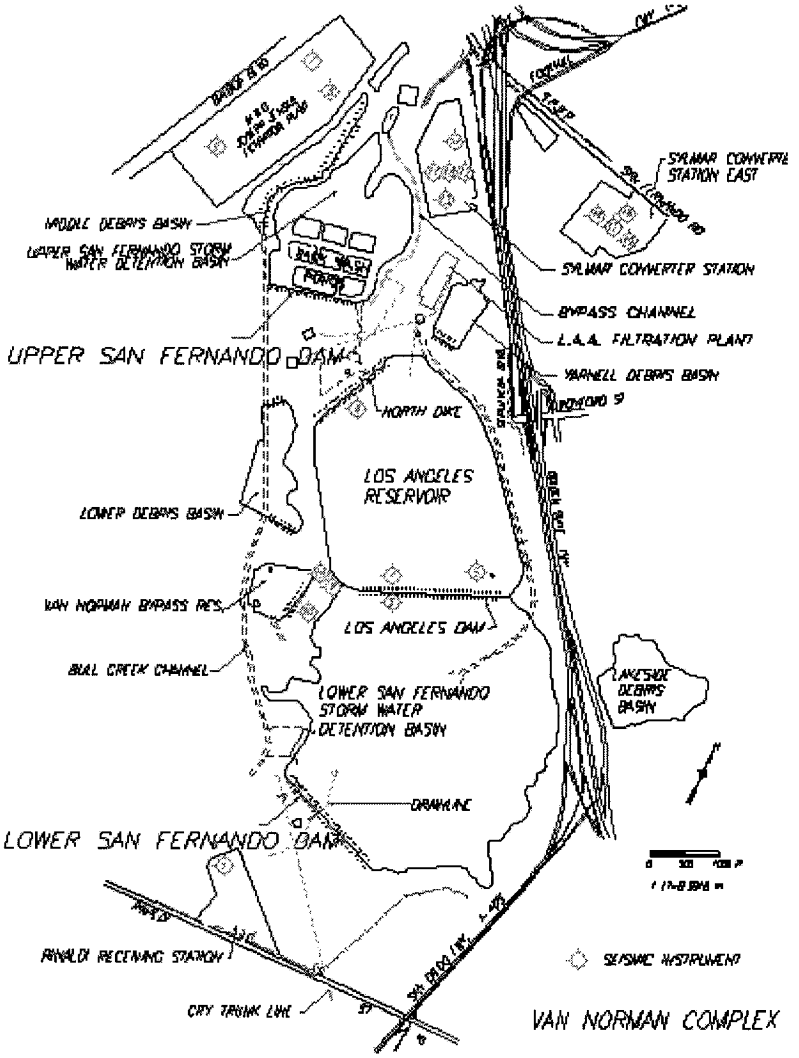

Figure 5-11. Van Norman Complex and its major facilities including the Upper and Lower San Fernando Dams (courtesy of LADWP).

The USFD was constructed between 1919 and 1921 using a semi hydraulic fill technique (Seed et al. 1973). Figure 12 shows the typical transverse cross-section of the Upper San Fernando Dam. The embankment of the USFD is founded on deposits of recent alluvium, consisting of stiff clays and clayey gravels about 15 m to 20 m in thickness. The upstream and downstream are consisted of hydraulic fill material. In 1922, the USFD was raised by adding rolled fill on the upstream slope. The maximum height of the dam is about 24.4 meter. The completed section of the dam has a 2.5:1 concrete-paved upstream slope, a crest of 20 feet wide, and a downstream slope of 2.5:1 as shown in Figure 11. The reservoir water level was about at elevation 371m and 363m in the 1971 San Fernando Earthquake and the 1994 Northridge Earthquake, respectively.

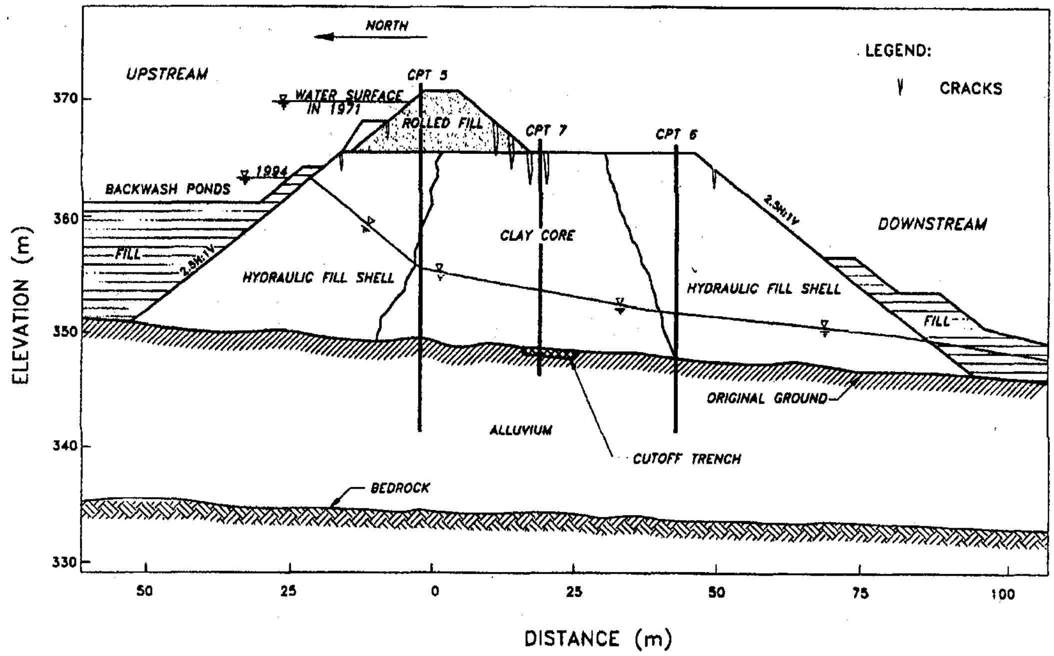

Figure 5-12. Typical cross section of the Upper San Fernando Dam with indicated ground water level at 1971 and 1994 (from Bardet and Davis 1996).

Both the Upper and Low dams suffered major damage during the 1971 San Fernando Earthquake. The 1971 San Fernando Earthquake occurred on February 9, 1971, had an Mw of 6.6, and an epicenter about 11 km from the dams. Peak ground accelerations at the site were estimated to be around 0.6g (Seed et al. 1973). The earthquake damaged the USFD causing up to 0.9m of settlement, 2.0 m of downstream movement, and up to 0.6 m of longitudinal movement. Several longitudinal cracks were observed along the upstream face near the reservoir level (Serff et al. 1976). Liquefaction was suggested by sand boils below the toe and increased water levels in the three standpipe piezometers. Following the 1971 earthquake, emergency repairs were performed to keep the USFD in service until the completion of the Los Angeles Reservoir in 1977. It was then removed from service, and with any significant alternation became a retention structure for storm water control (Bardet and Davis 1996). The downstream movement of the Upper San Fernando Dam led to some cracking of the embankment. However although the crest moved downstream about 5 feet and settled about 3 feet there was no breach resulting in loss of water from the reservoir. If this had not been the case and water from the Upper Van Norman Lake had been released, overtopping of the Lower Dam would have ensued.

During the 1994 Northridge earthquake, the USFD, which was out of service and retained only a few meters of water, performed better than in 1971 event. Some minor damage, sand boils and cracks are been reported from earthquake reconnaissance right after the earthquake (Bardet and Davis 1996). The dam crest moved 15 cm in the upstream direction and slightly moved in the downstream direction. The maximum settlement in the order of 45 cm takes place at the same location as the maximum lateral movement. For the current study, the performance of the USFD during the 1994 Northridge earthquake is not studied since the observed deformation is very small.

5.7.2 Soil parameters of the Upper San Fernando Dam

A program of field and laboratory investigations of the characteristics of the soils comprising the embankments of the Upper and Lower San Fernando Dams was initiated almost immediately after the earthquake (Seed et al. 1973). The standard penetration test on a split spoon sampler followed by a 3 inch diameter thin wall Shelby tube sample was carried on at various cross sections along the USFD. Figure 12 shows one example of this cross section with abbreviated drill logs. The results of standard penetration tests are also shown on the cross sections. It maybe seen that the blow count were very low (less than 15) in the silt and clay core of the central portion of the hydraulic fill, whereas the blow count in the alluvium zone was a significant increase. The field seismic surveys determined that the shear wave velocity of the hydraulic fill was about 180 m/s (600 ft/s).

On the basis of the information obtained from the drilling and sampling from previous field investigation, the USFD is divided into six material zones including lower alluvium, upper alluvium, upstream hydraulic fill, downstream hydraulic fill, clay core and rolled fill. The geometry and the boundaries between the major soil zones for finite element analysis is established as shown in Figure 13.

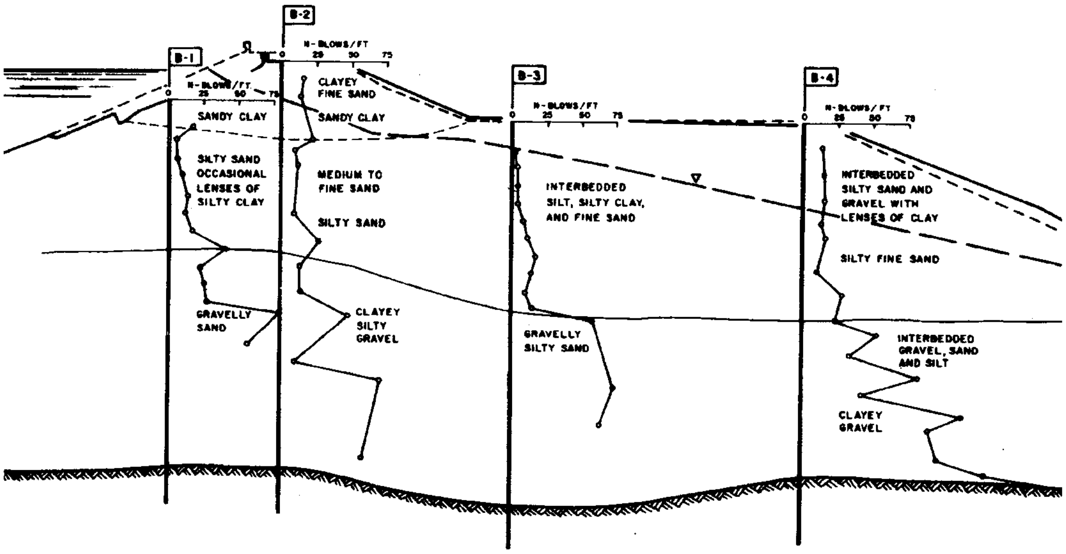

Figure 5-13. One example of cross sections through the USFD with soil profiles and SPT test results.

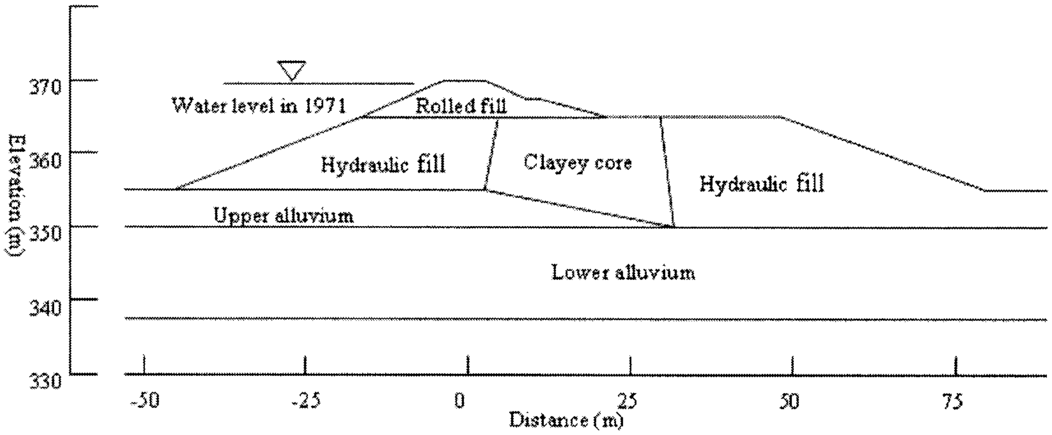

Figure 5-14. Cross section used in finite element analysis and corresponding six soil material zones of the USFD.

Material properties were derived primarily from the laboratory and in-situ testing performed in 1973 (Seed et al. 1973). The elastic modulus for the current elasto-plastic J2 finite strain model can be estimated using typical values under static loading conditions from the low-strain shear modulus and a modulus reduction factor, (MRF). The size of failure surface for J2 plasticity will be determined from the residual strengthens before and after the liquefaction.

In general, the low-strain shear modulus, G_{max}, can be determined from the in-siu measured shear wave velocity, i.e.

$$G_{\max} = \rho v_s^2 \tag{5-63}$$

here ρ is the soil mass density and υ_s is the in-situ shear wave velocity. When shear wave velocity measurements are not available, G_{max} can be estimated in several ways. Seed and Idriss (1970) proposed the empirical relationship between the shear modulus and the confining stress, i.e.

$$G_{\max} = 21.7 K_{2\max} P_a \left(\frac{\sigma_m^{'}}{P_a} \right)^{0.5} \tag{5-64}$$

where P_a is the atmospheric pressure (commonly taken as 100 kPa); $\sigma_m^{'}$ is the effective mean normal stress; and K_{2max} is a soil modulus coefficient which can be correlated with the standard penetration resistance $(N_1)_{60}$ (Seed et al. 1986). Empirical relationship between G_{max} and the confining pressure are also available based on the void ratio of sand (Hardin and Drnevich 1972). The shear modulus and bulk modulus can be expressed in the following equations:

$$G_{\max} = K_g P_a \left(\frac{\sigma_m'}{P_a} \right)^n \qquad B = K_b P_a \left(\frac{\sigma_m'}{P_a} \right)^m \tag{5-65}$$

where B is the bulk modulus, K_g is the shear modulus constant, n is the shear modulus exponent (normally n=0.5), K_b is the bulk modulus constant, and m is the bulk modulus exponent.

Table 3 lists the soil properties for the five different zones. These properties are obtained from Seed et al. (1973).

Table 5-3. Soil stiffness and strength parameters of the Upper San Fernando Dam.

	Unit weight (kN/m3)	$K_{2\max}$	K_g	K_b	c' (kPa)	ϕ
Lower alluvioum	20.3	110	2387	6000	0	37
Hydraulic fill sand	19.2	30	651	1630	0	37
Upper alluvium	20.3	40	868	2170	0	37
Clayey core	19.2	--	651	1630	0	37
Hydraulic fill sand	19.2	30	651	1630	0	37
Rolled fill	22	52	1128	2821	124.5	25

A critical input parameter for the dynamic deformation analysis is the post-liquefaction residual shear strength of the dam and alluvium materials. Residual strength of liquefied materials has a major impact on the post-liquefaction stability of an earth structure. The selection of residual strength remains a very controversial issue, as discussed by Finn (1998). Usually Residual strengths are often obtained from back analysis of case histories (Seed and Harder 1990) or from direct laboratory tests, where the residual strength is expressed as an undrained shear strength. Stark and Mesri (1992) also proposed a residual strength ratio method S_u / σ'_{v0}, where S_u is the residual shear strength and σ'_{v0} is the average value of initial vertical effective stress within the significant liquefied material. Limit equilibrium analysis have been performed on the USFD to estimate values of residual strength (Harder et al. 1989). Back analysis of the Upper San Fernando Dam indicated that an average ratio S_u / σ'_{v0} is about 0.13 to 0.19 for the hydraulic fill material. The current study uses the S_u / σ'_{v0} ratio of 0.15 to estimate the undrained shear strength for liquefied layer as recommended by Byrne and Beaty (1999). The undrained residual strength is about 23 kPa in average for the liquefied loose hydraulic fill sand.

A reduced stiffness also should be specified for the liquefied material in the deformation analysis. The post-liquefaction soil shear modulus can be defined using the residual shear strength as proposed by Beaty and Byrne (2000) and Wu (2001),

$$G_{Liq} = K_{Liq} S_r \tag{5-66}$$

here K_{liq} is a parameter defining the stiffness of liquefied soil. The stiffness and strength of the liquefied soil element are governed by the assigned stiffness G_{liq} and residual shear strength S_u. For the liquefied soil element, a residual strength of 23 kPa was assigned based on the review of blow count data. The corresponding reduced shear modulus is estimated from Eq. 67. The soil parameters related to liquefaction used for finite element analysis is listed in Table 4. The equivalent

N1(60) value is obtained from Seed et al. (1973). The K_{liq} value is suggested by Wu (2001).

Table 5-4. Residual strength and reduced shear modulus for hydraulic fill zone after liquefaction.

Soil zone	$N_{1(60)}$	S_u (kPa)	K_{Liq}	G_{Liq} (kPa)
Upstream hydraulic fill	14	23	400	9200
Downstream hydraulic fill	14	23	400	9200

5.7.3 Procedure of finite element analysis

A total of 769 QUAD elements are used to simulate the six different material zones as identified in Figure 14. The finite element mesh is shown in Figure 15.

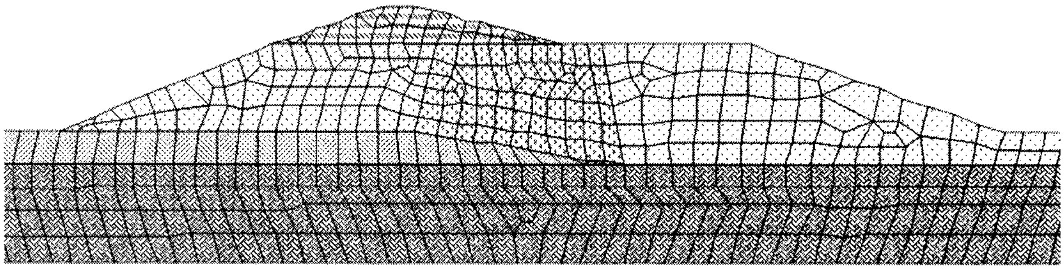

Figure 5-15. Finite element meshes of the USFD (different shadings indicate the boundary of six soil zones).

The initial equivalent state and the final equivalent stage before and after liquefaction are simulated by the following computation procedures:

Pre-liquefaction analysis

The analysis prior to liquefaction is identical to the routine finite element static stress analysis. Suitable values of elastic modulus and shear strength are assigned to each material zone. The water pressure due to reservoir water level at elevation 371 m at the time the 1971 San Fernando Earthquake happened was applied to element nodes at reservoir bed and upstream surface. The parameters of J2 plastic model for each material zone are listed in Table 5. The Young's modulus E is obtained from shear modulus by using Poisson ratio. The radius of failure surface r is calculated used the equation, i.e.

$$r = 2S_u / \sqrt{3} \qquad (5\text{-}67)$$

here S_u is shear strength.

Table 5-5. J2 plastic parameters for different material zones in pre-liquefaction analysis.

Name	Lower alluvioum	Upstream hydraulic fill	Upper alluvium	Clayey core	Downstream hydraulic fill	Rolled fill
Property number/name	1	2	3	4	5	6
Young's modulus *E* (kPa)	230165	32662	69143	52722	40082	35020
Poisson ratio ν	0.33	0.33	0.33	0.33	0.33	0.33
Radius of failure surface r (kPa)	138	71	90	57	107	132
Unit mass of material ρ (kN/m^3)	2.03	1.92	2.03	1.92	1.92	2.2

Step by step integration algorithm is used for this initial static analysis. The full Newton-Rapson method is utilized to solve the nonlinear system. The large deformation formulation is not invoked in this step. Figure 16 shows the distributed horizontal and vertical stress of the initial static analysis. The distribution of the horizontal and vertical stress is very similar for this two dimensional problem.

The maximum value of the horizontal and vertical stress, which occurs at the bottom of the dam under the crest, is about 370 kPa and 610 kPa, respectively. The stress status from this analysis will be reserved as initial stress status for the next step computation.

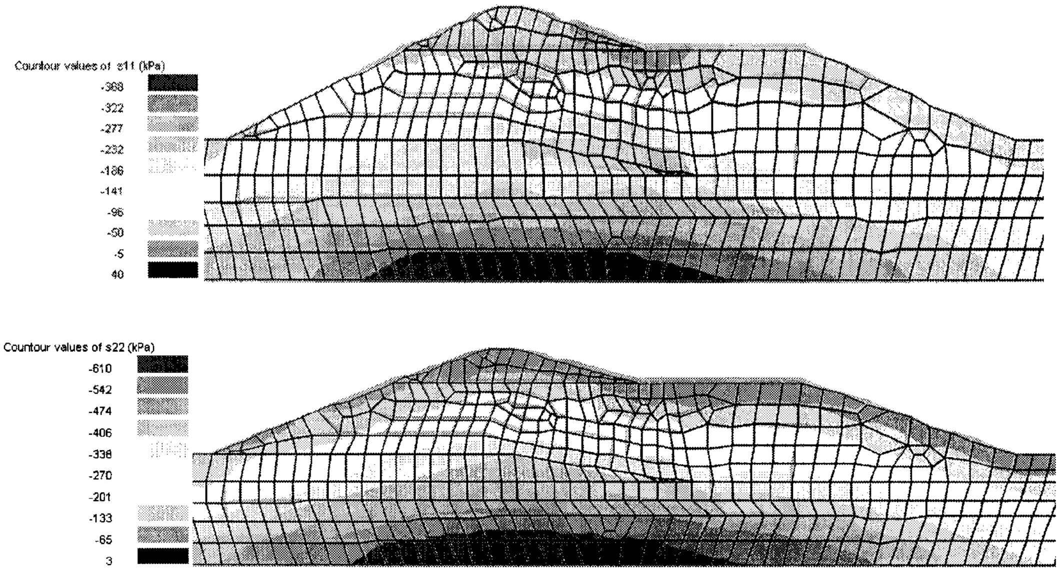

Figure 5-16. Horizontal and vertical stress distributions in the USFD after the initial static stress analysis.

Post-liquefaction analysis

The final position which decided for the liquefaction in the hydraulic fill zone is found by reducing the soil properties of the hydraulic fill zone to the post-liquefaction value. Liquefaction was permitted throughout the saturated hydraulic fill zone, but not in the other embankment zones or the foundation. The liquefaction zone was determined from previous analysis by Seed et al. (1973). This liquefied zone was compatible with the analysis result from Beaty and Byrne (2000). The finite strain elasto-plastic J2 model is applied with Green-McInnis stress rate option in this step analysis. The parameters of J2 for the hydraulic fill zone is obtained from post liquefaction soil properties as listed in Table 6. The Young's modulus and radio of failure surface is adjusted to reflect the residual shear strength and reduced the shear modulus. The Poisson's ratio of the hydraulic fill zone is set to 0.499 to simulate the undrained condition of the liquefied soil. The explicit solution scheme described in previous section is used for this nonlinear system where the dynamic equations of equilibrium are satisfied. The mass of each element is lumped at nodal points. Hyperbolic analysis was employed with 4 stress points per element. The stress status from the pre-liquefaction analysis has been taken as the initial stress status.

Table 5-6. J2 plastic model parameters for different material zones in post-liquefaction analysis.

Name	Lower alluvioum	Upstream hydraulic fill	Upper alluvium	Clayey core	Downstream hydraulic fill	Rolled fill
Property number/name	1	2	3	4	5	6
Young's modulus E (kPa)	230165	9200	69143	52722	9200	35020
Poisson ratio ν	0.33	0.50	0.33	0.33	0.50	0.33
Radius of failure surface r (kPa)	138	23	90	57	23	132
Unit mass of material ρ (kN/m^3)	2.03	1.92	2.03	1.92	1.92	2.2

5.7.4 Results of earthquake deformation analysis

The computed deformation pattern is illustrated in Figure 17. The deformation is occurred among the hydraulic fill zone and the rolled fill crest area. Most of the embankment has moved in the downstream direction, including the crest, except some lateral movement toward the upstream at the upstream surface. This agrees with post-earthquake observations documented by (Serff et al 1976). The change in the displacement direction, from downstream to upstream, occurs on the upstream face about the interface between the rolled fill zone and the upstream hydraulic fill zone.

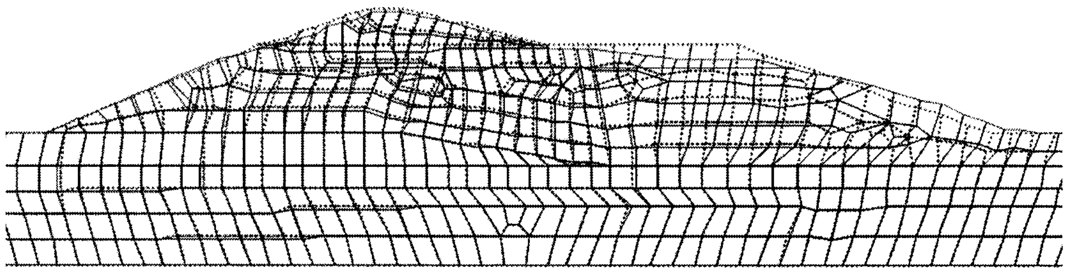

Figure 5-17. Deformed and undeformed finite element mesh of the Upper San Fernando Dam (Solid line is deformed mesh and dash line is undeformed mesh).

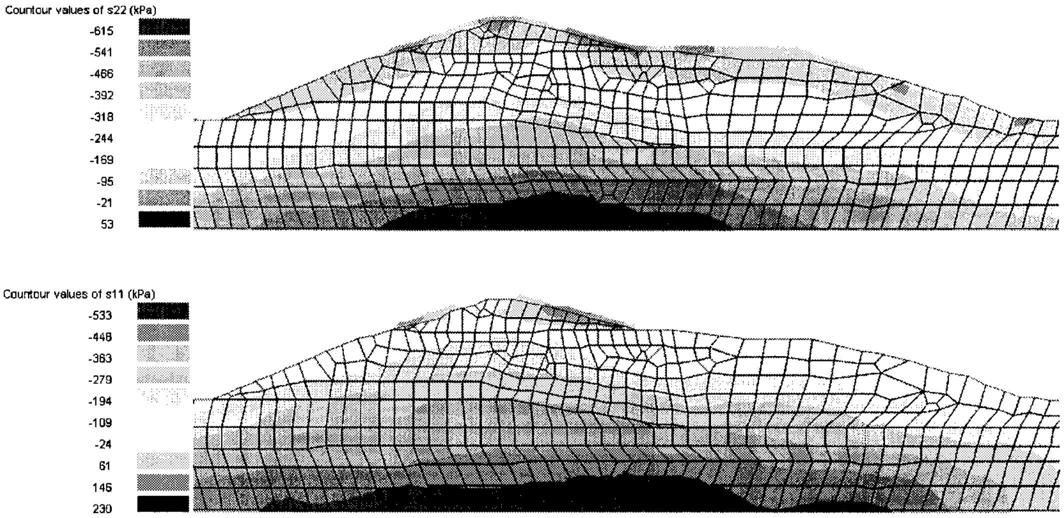

Figure 5-18. Horizontal and vertical stress distributions in the USFD after the post-liquefaction anaylsis.

Displacements along the dam surface computed by the FE program are shown in Figure 19. The horizontal distance is measured from the center line of the crest as defined in Figure 14. The measured displacements from Serff et al. (1976) are plotted in the Figure 19 to compare with the calculated result from this study. The vertical displacements computed in this study agree well with the measured values from the dam crest to the edge of the downstream slope, whereas the numerical calculation underestimates the horizontal displacement for the dam crest.

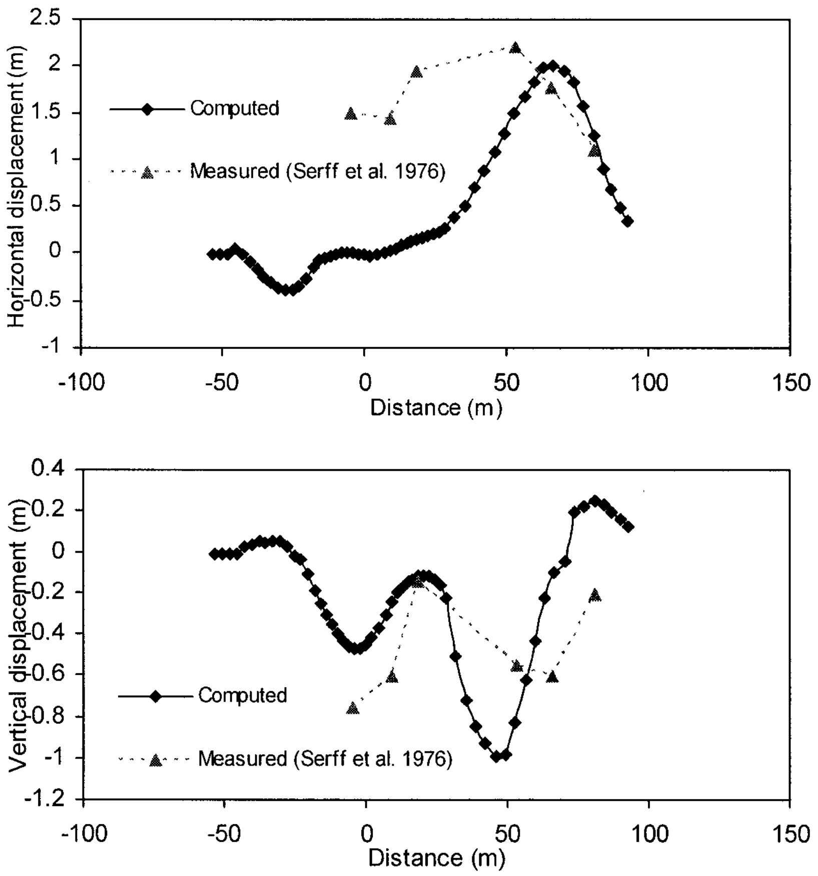

Figure 5-19. Computed horizontal displacement and vertical settlement along the dam surface compared with measured result from Serff et al. (1996).

The dam crest is predicted to move 0.2m and settle 0.5m. The surface of downstream slope is predicted to move downstream about 2.0 m and settle almost 1.0 m. The computed deformations at the downstream surface agree well with the observed deformations. It is believed that the non-liquefied rolled fill and clayey core prevented the dam crest from moving downstream because of the high shear strength and stiffness. Most of the settlement and lateral movement are happened at the downstream hydraulic fill zone. The maximum settlement is 2.1 m which happened at the top of downstream hydraulic fill zone.

5.8 Discussion and future research

The implemented two-dimensional nonlinear finite element with finite strain J2 model, although it can consider the gravity effect on the liquefied soil system, oversimplifies the actual post-liquefaction behavior of the materials. There is a need for further research to complete the present work.

The current study predicts the earthquake-induced deformation by assuming the zone of liquefaction based on previous research work. The extent of liquefaction and amount of pore-water pressures maybe well assessed using the existing effective stress models (Martin et al. 1975, Ishihara and Towhata 1980, Iai et al. 1992). They could be used for predicting reduced undrain shear strength but this was not been done here. Effective stress models concentrated on buildup of pore water pressure during cyclic loading is capable of determining the onset liquefaction. It should be investigated that how to apply the effective stress models, which was developed for small strain experiment and are not tested for large strain, to evaluate the ground deformation over large area.

The finite strain J2 plastic model is used in this study because it suits the undrained behavior of liquefied soil (small elastic strain and large plastic strain with constant plastic volume). Other advanced elasto-plastic soil constitutive models in addition to J2 plastic model should be further studied to simulate the ground deformation under drained or undrained condition. The current research work is based on the hypoelastic rate model which are widely used in numerical analysis for rock and soil material which exhibit strong nonlinear behavior, although the hyperelastic-based plasticity model is more satisfying from a theoretical point view. The hyperelastic stress-strain relations based on the multiplicative decomposition of the deformation gradient ($\mathbf{F} = \mathbf{F}^e\mathbf{F}^p$) should be study in the future investigation.

The well-documented case histories and proposed geostatistical tools for parameters analysis and estimation need to be integrated with the current numerical method to assess the ground deformation over region area. It is recommended to extend the recent approach to a three-dimensional finite element combined with GIS and spatial analysis to apply for mapping areas prone to deformation due to liquefaction during future earthquakes.

5.9 Conclusion

A finite element method which is based on finite strain J2 elasto-plastic model and accounts for material and geometry nonlinearities of the system has been proposed for earthquake induced ground deformation analysis. The generalized J2 plasticity has been described to specify the tangent modulus for the mid-point increment stress calculation. The final position of the nonlinear system under low shear strength is found by solving the dynamic equation of motion. The implementation of this J2 finite strain model has been used to simulate the single element test and slump test model.

The GEOFEEX finite strain model is applied to study the deformation of the Upper San Fernando Dam by considering the reduced shear strength and stiffness for the liquefied material. Reasonable to good agreement was obtained between field observations and analysis.

6 CONCLUSION

Both empirical methodology and numerical procedure have been investigated realistically evaluate the liquefaction-induced large ground deformation. The advances in information technology, Web service and XML, have been used to store and exchange valuable information about liquefaction-induced ground deformation case histories. The uncertainty of prediction using empirical ground deformation model has been evaluated using GIS and geostatistic. The large deformation caused by low shear strength and reduced modulus after liquefaction are studied using finite strain theory based on J2 elasto-plastic model and nonlinear finite element program.

In Chapter 2, a relational database framework was developed for storing the large amount of data on liquefaction-induced ground deformation, including the data sets on displacement vectors and soil SPT and CPT boreholes. Two relational databases LIDD and BOD were developed for structuring and storing the large amount of data on liquefaction-induced ground deformation, including the data sets on displacement vectors and soil SPT and CPT boreholes. LIDD, which stands for Liquefaction-Induced ground Deformation, contain displacement vectors and earthquake characteristics. BOD, an acronym for BOrehole Database, contains all soil properties profiles in the areas of liquefaction-induced ground deformation. Both LIDD and BOD are compatible with GIS techniques. The LIDD database contains 16,000 displacement vectors, and the BOD database 902 SPT and 229 CPT soundings. The complete set of ground deformation data and geotechnical information provide enough information for developing and improving the methods for assessing and quantifying the liquefaction potential of ground deformation, and developing new generations of models for liquefaction-induced deformation. A system architecture called GIME which emerging Web services standard to build infrastructures in the geotechnical and other distributed data integration projects has been proposed to exchange the geotechnical data.

In Chapter 3, a methodology for predicting liquefaction-induced ground deformation over large areas has been presented and illustrated using a case study in Port Island after the 1995 Hyogoken-Nanbu earthquake. The methodology relies upon the ground-deformation model of Bardet et al. (2002), geostatistics and geographic information system (GIS). The prediction of liquefaction-induced ground deformation over large regions requires data on soil boreholes, high resolution topography and ground water surface elevation. Geostatistics and GIS are combined to generate the model parameters over extended areas, and to examine the standard deviations of model parameters and results. The comparison of predicted and observed results shows that the methodology is capable of predicting the ground deformation observed in 1995, even though the ground deformation model was calibrated from earthquake case histories prior to 1994. The proposed methodology is intended for the microzonation of liquefaction hazards worldwide.

In Chapter 4, the finite strain theory has been introduced to account for the large strain or large rotation for geometries nonlinearaity and material nonlinearity in finite element analysis. The basic formulation of deformation and motion is been defined. We confine our attention to the strain and stress measures that are most frequently employed in nonlinear finite element programs: the Green strain tensor and the rate of deformation. Different stress measures have been investigated. The objective rates, also called frame-invariant rates, of the Cauchy stress tensor are examined.

In Chapter 5, a finite element method based on finite strain J2 elasto-plastic model has been proposed for earthquake induced ground deformation analysis which accounts for material and geometry nonlinearities of the system. This model is implemented in the existing finite element program GEOFEEX. Explicit dynamic scheme has been applied to solve the equation of motion to find the solution of the nonlinear system under low shear strength. The implementation of this J2 finite strain model has been used to simulate the single element test and slump test model. The GEOFEEX finite strain model is applied to the Upper San Fernando Dam to study the deformation by considering the reduced shear strength and stiffness for the liquefied material. Reasonable to good agreement was obtained between field observations and the analysis.

In addition to the major finding in present work, future researches have been discussed. The well-documented case histories and proposed geostatistical tools for parameters analysis and estimation need to be integrated with the current numerical method to assess the ground deformation over region area. It is recommended to extend the recent approach to a three-dimensional finite element combined with GIS and spatial analysis to apply for mapping areas prone to deformation due to liquefaction during future earthquakes.

REFERENCES

1. Adachi T. and Oka, F. (1982). "Constitutive equations for normally consolidated clay based on elasto-visco plasticity." *Soils and Foundations*, Vol. 22, No. 4, 57-70.

2. ArcGIS. (2002), "ArcGISTM Geostatistical analyst: Statistical Tools for data exploration, modeling, and advanced surface generation", *ESRI White Paper*, ESRI, Redlands, CA.

3. Bailey, T. and A. Gatrell, 1995, "Interactive spatial data analysis," *Longman Scientific & Technical*, England.

4. Balakrishnan, A. and Kutter, B. L. (1999) "Settlement, sliding and liquefaction remediation of layered soil", *Journal of Geotechnical and Geoenvironmental Engineering*, Vol. 125, No. 11, 968-978.

5. Bardet, J. P. (2003). "Advances in Analysis of Soil Liquefaction during Earthquakes," in *Interna-tional Handbook of Earthquake and Engineering Seismology* (Edited by W. H. K. Lee, H. Kanamori, P. C. Jennings, and C. Kisslinger), Chapter 77, in press.

6. Bardet, J. P. (1995). "A Scaled Memory Model for the Cyclic Behavior of Soils." *Journal of Geotechnical Engineering, ASCE*, Vol. 121, No. 11, 766 – 775.

7. Bardet, J. P. (1986). "A Bounding Surface Plasticity Model for Sands." *Journal of Engineering Mechanics, ASCE*, Vol. 112, No. 11, 1198 -1217.

8. Bardet, J. P., and C. A. Davis. (1996) "Performance of San Fernando Dams during the 1994 Northridge Earthquake," *Journal of Geotechnical Engineering*, ASCE, Vol. 122, No. 7, 554-564.

9. Bardet, J. P., Hu, J., Tobita, T. and Swift, J. (1999a). "Liquefaction Ground Deformation Database," *A report to PG&E-Caltrans-PEER Program of Applied Earthquake Engineering Research on Life-lines, Task 3A04*, Civil Engineering Department, University of Southern California.

10. Bardet, J. P., Mace, N. and Tobita, T. (1999b). "Liquefaction-induced ground deformation and failure" *A report to PEER/PG&E, Task 4 – Phase 1*, Civil Engineering Department, University of Southern California.

11. Bardet J. P., Tobita, T., Mace, N., and Hu, J. (2002). "Regional modeling of liquefaction-induced ground deformation." *Earthquake Spectra*, Earthquake Engineering Research Institute, 18(1), 19-46.

12. Bartlett, S. F., and Youd, T. L. (1992). "Empirical analysis of horizontal ground displacement generated by liquefaction-induced lateral spreads." *Technical report NCEER-92-0021*, National Center for Earthquake Engineering Research, State University of New York, Buffalo.

13. Bartlett, S. F. and Youd, T. L. (1995). "Empirical prediction of Lateral Spread Displacement." *Journal of Geotechnical Engineering*, ASCE, 121(4), 316-329. 10.

14. Baziar, M. H., Dobry, R. and Elgamal, A. W. M. (1992) "Engineering evaluation of permanent ground deformation due to seismically-induced liquefaction," *Technical report NCEER-92-0007*, National Center for Earthquake Engineering Research, State University of New York, Buffalo.

15. Beaty, M. H. and Byrne, P. M. (2000). "A synthesized approach for predicting liquefaction and resulting displacements." *12th World Conference on Earthquake Engineering*, Paper No. 1589.

16. Borcherdt, R. D. (1993). "Characterization and predictive GIS mapping of strong ground shaking for earthquake hazard reduction in urban areas", *Proceedings of the 3rd United States/Japan workshop on Urban Earthquake Hazard Reduction*, Feb. 1993.

17. Borcherdt, R. D. (1997). "Spatial ground-motion amplification analysis", Geotechnical Special Publication 67, Spatial analysis in Soil Dynamics and Earthquake Engineering, ASCE, New York, 56-69.

18. Byrne, P. M. (1997). "Liquefaction-induced displacements," *NCEER Workshop on Post-liquefaction Ground Deformation*, Presentation Notes, August

19. Byrne, P. M. (1991). "A model for predicting liquefaction induced displacement." Proceedings of the Second International Conference on Recent Advances in Geotechnical Eearthquake Engineering and Soil Dynamics, St. Louis, Missouri, 2, 1027-1035.

20. Byrne, P. M., Salgado, F. and Jitno, H. (1992). "Earthquake induced displacements of soil-structure systems." *Proceedings: Tenth World Conference on Earthquake Engineering*, Madrid, Spain, 1407-1412.

21. Carrara, A., et al. (1999). "Use of GIS technology in the prediction and monitoring of landslide hazard", *Natural Hazards*, 20, 2-3, 117-135.

22. Chandler, J. L. (1986). "The stacking and solar drying process for disposal of bauxite tailings in Jamaica." *Proceedings of the International Conference on Bauxite Tailings*, Kingston, Jamaica (1986), 101-105.

23. Chiles, J. P. and P. Delfiner. (1999). "Geostatistics – Modeling Spatial Uncertainty," *John Wiley & Sons*, New York.

24. Christensen, G. (1991). "Modeling the flow of fresh concrete: the slump test." *Ph.D. thesis*, Princeton University.

25. Codd, E. (1970). "A Relational Model for Large Shared Data Banks", *CACM*, Vol. 13, No. 6.

26. Dafalias, Y. F., and Herrmann, L. R. (1982). "Bounding surface formulation of soil plasticity." *Soil Mechanics – Transient and Cyclic Loads*, G. Pande and O. C. Zienkiewicz, eds., John Wiley and Sons, Inc., London, 253-282.

27. Davis, C., and Bardet, J. P. (1996). "Performance of Two Reservoirs during the 1994 Northridge Earthquake," *Journal of Geotechnical Engineering, ASCE*, Vol. 122, No. 8, pp. 613-622.

28. Deutsch, C. V., and Journel, A. G. (1992). "GSLIB, geostatistical software library and user's guide," *Oxford University Press*, New York.

29. Dienes, J. K. (1979). "On the analysis of rotation and stress rate in deforming bodies." *Acta Mechanica,* Vol. 32, 217-232.

30. Dobry, R., Taboada, V. and Liu, L. (1995). "Centrifuge modeling of liquefaction effects during earthquakes" *Proceedings of the 1rst International Conference on Earthquake Geotechnical Engineering*, IS-Tokyo, Keynote and Theme lectures, 129-162.

31. Doroudian, M., Vucetic, M. and Martin, G. R. (1996). "Development of geotechnical data base for Los Angeles and its potential for seismic microzonation." Proceedings of the Fifth International Conference on Seismic Zonation, October 17-18-19, 1995, Nice, France, Vol. II, 1514-1521.

32. Eckstein, R. E. (1999). "XML, Pocket Reference," *O'Reilly*, Sebastopol, CA.

33. Elms, D. G. (2000). "Refinements to the Newmark sliding block model." *Proc 12th World Conference on Earthquake Engineering*, Auckland, New Zealand.

34. Famiglietti, C. M. and Prevost, J. H. (1994). "Solution of the slump test using a finite deformation elasto-plastic drucker-prager model." International Journal for Numerical Methods in Engineering, Vol. 37, 3869-3903.

35. Fiegel, G. L. and Kutter, B.L. (1994) "A Mechanism of liquefaction for layered soils." *Journal of Geotechnical Engineering*, Vol. 120, No. 4, pp. 737-755.

36. Finn, W. D. L.(2000). "State-of-art of geotechnical earthquake engineering practice." *Soil Dynamic and Earthquake Engineering*, Vol. 20, 1-15.

37. Finn, W. D. L. (1998). "Seismic safety of embankment dams: developments in research ad practice 1988-1998." *In Proceedings of the 1998 Specialty Conference on Geotechnical Earthquake Engineering and Soil Dynamics III*, Seattle, 813-853.

38. Finn, W. D. L., Yogendrakumar, M., Yoshida N., and Yoshida, H. (1986). "TRRA-3: a program for nonlinear static and dynamic effective stress analysis." The University of British Columbia, Vancouver, B.C.

39. FLAC. (1995). "Fast Lagrangian Analysis of Continua," Version 3.3, *Itasca Consulting Group Inc*, Minneapolis, Minesota

40. Friberg, P., Tuttle, M. and Jacob, K.H. (1991). "Relational database and GIS technology for earthquake hazard zonation", *Proceedings of the Fourth International Conference on Seismic Zonation*, Vol 3, 585-592.

41. Frost, J. D., Carroll, D. P. and Rockaway, T. D. (1997) "Spatial liquefaction analysis", *Geotechnical Special Publication 67*, Spatial Analysis in Soil Dynamics and Earthquake Engineering, ASCE, New York, 70-86.

42. Frost, J.D. and Chameau, J.L. (1993). "Considerations in Integrating Geographic Information System Technology in Earthquake Hazard Analyses", *Proceedings of National Science Foundation Workshop on Geographic Information Systems and their Application in Geotechnical Earthquake Engineering*, Atlanta, pp. 49-55

43. GoldenSoftware. (1997). "Surfer 7.0". *GoldenSoftware Inc.*, Golden, Colorado.

44. Goldstein, H. (1981). "Classical Mechanics," 2nd ed., *Addison-Wesley*, Mass.

45. Green, A. E. and Naghdi, P. M. (1965). "A general theory of an elastic-plastic continuum." *Arch. Rat. Mech. Anal.* Vol. 18, 251-281.

46. Green, A. E. and McInnis, B. C. (1967). "Generalized hypo-elasticity" *Proc. Roy. Soc.* A57, 220-230.

47. Gurtin, M. E. (1981). “An Introduction to Continuum Mechanics”, *Academic Press*, San Diego.

48. Hamada, M., Isoyama, R. and Wakamatsu,K. (1996a). “Liquefaction-induced ground displacement and its related damage to lifelines facilities.” *Soils and Foundations,* Special issue on Geotechnical Aspects of the January 17 1995 Hyogoken Nambu Earthquake, Japanese Geotechnical Society, 81 - 97.

49. Hamada, M. and K. Wakamatsu. (1996b). “Liquefaction, Ground Deformation and their Caused Damage to Structures,” *The 1995 Hyogoken-Nanbu Earthquake-Investigation into damage to Civil Engineering Structures*, Committee of Earthquake Engineering, Japan society of Civil Engineers, 45-92.

50. Hamada, M., and T. D. O'Rourke. (1992). “Case histories of liquefaction and lifeline performance during past earthquakes,” *Technical report NCEER-92-0001*, National Center for Earthquake Engineering Research, State University of New York, Buffalo, 2 Vols.

51. Hamada, M., Yasuda, S., Isoyama, R. and Emoto, K. (1986) “Study on Liquefaction induced permanent ground displacement," *Report for the Association for the Development of Earthquake Prediction in Japan.*

52. Hardin, B. O. and Drnevich, V. P. (1972). “Shear modulus and damping in soils: design equations and curves.” *J. Soil Mech. Found. Div.*, 1, 2-89.

53. Hill, R. (1958). “A general theory of uniqueness and stability in elasto-plastic solids,” *Journal of Mechanics and Physics of Solids*, Vol. 6, 236-249.

54. Hillier, F. S. and Lieberman, G. J. (1995). “Introduction to Operations Research”. 6th Ed. *McGrawHill*, New York.

55. Horii, K. (1968). “Damages on Road Bridges.” *Report on the Niigata Earthquake*, Tokyo Denki University Press, pp 431-450.

56. Hughes, T. J. R. (1984). “Numerical implementation of constitutive models: rate-independent deviatoric plasticity,” in *Theoretical Foundations for Large Scale Computations of Nonlinear Material Behavior*, Martinus Nijhoff Publishers, Dordrecht, The Netherlands 29-57.

57. Hughes, T. J. R. and Winget, J. (1980). “Finite rotation effects in numerical integration of rate constitutive equations arising in large-deformation analysis.” *International Journal for Numerical Methods in Engineering*, Vol. 15, 1862-1867.

58. Iai, S. (1991). “A Strain Space Multiple Mechanism Model for Cyclic Behavior of Sand and its Application.” *Earthquake Engineering Research Note No. 43*, Port and Harbor Research Institute, Ministry of Transport, Japan.

59. Iai S., Ichii K., Morita T. and Miyata M. (1997). “Seismic performance of caisson walls on loose saturated sand foundation.” *Proceedings of the fourteenth international conference on soil mechanics and foundation engineering*, A.A.Balkema, 1997.

60. Ishihara, K. (1996). “Soil Behavior in Earthquake Geotechnics.” *Clarendon press*, Oxford.

61. Ishihara, K. (1993). “Liquefaction and flow failure during earthquakes.” The 33rd Rankine lecture, *Géotechnique*, 43(3), 351 - 415.

62. Ishihara, K. and Towhata, I. (1980). “One-dimensional soil response analysis during earthquakes based on effective stress analysis.” *Journal of the faculty of engineering*, The University of Tokyo (B), Vol. XXXV, No. 4, 655-700.

63. Isaaks, E.H., Srivastava, R.M. (1990). “Applied Geostatistics”. *Oxford University Press.*

64. Japan Oceanographic Data Center (JODC). http://www.jodc.go.jp/index.html.

65. Jennings, R. (1997). “Using Access97. 2nd Ed.” *Que corporation*, 201W. 103rd street, Indianapolis, IN 46290.

66. Jibson, R. (1994). "Predicting earthquake-induced landslide displacement using Newmark's sliding block analysis," *Transportation Research Record 1411*, Transportation Research Board, Washington, D.C., 9-17.

67. Kawai, T. (1985). “DIANA – Dynamic Interaction Approach and Nonlinear Analysis.” Science University of Tokyo.

68. Key, S. W. (1974). “HONDO- A finite element computer program for the large deformation response of axisymmetric solids.” *Report 74-0039, Sandia National Laboratories*, Albuquerque, N.M.

69. Key, S. W., Stone, C. M. and Krieg, R. D. (1981). “Dynamic relaxation applied to the quasi-static, large deformation, inelastic response of axisymmetric solids” in *Nonlinear Finite Element Analysis in Structural Mechanics, Springer*, Berlin.

70. Kim, S. J. and Oden, J. T. (1985). “Finite element analysis of a class of problems in finite elasto-plasticity based on the thermodynamical theory of materials of type N.” *Comput. Methods Appl. Mech. Eng.*, Vol. 79, 277-302.

71. Koketsu, K., Yoshida, S. and Higashihara, H. (1998). "A fault model of the 1995 Kobe earthquake derivefrom the GPS data on the Akashi Kaikyo Bridge and other datasets", *Earth Planets Space*, 50, 803–811.

72. Kokusho, T. (1999). "Water Film in Liquefied Sand and Its Effect on Lateral Spread," *Journal of Geotechnical and Geoenvironmental Engineering*, Vol. 125, No. 10, 817-826.

73. Kramer, S. L. (1996). "Geotechnical Earthquake Engineering." *Prentice-Hall*, Upper Saddle River, New Jersey.

74. Lee, E. H. and Liu, D. T. (1967). "Finite strain elastic-plastic theory particularly for plane wave analysis." *Journal of Applied Physics*, Vol. 38.

75. Liu, W. K., Guo, Y., Tang, S. and Belytschko, T. (1998). "A multiple-quadrature eight-node hexahedral finite element for large deformation elastoplastic analysis," *Comput. Methods Appl. Mech. Engrg*, Vol. 154, 69-132.

76. Maguire, D.J. (1991). "An Overview and Definition of GIS, Geographical Information System", Vol. 1, D.J. Maguire, M.F. Goodchild and D.W. Rhind, Eds., *Longman Scientific and Technical*, New York, NY, 9-20.

77. Marsden J. E. and Hughes, T. J. R. (1994). "Mathematical Foundations of Elasticity," *Dover*, New York.

78. Martin, G.R., Finn, W.D.L. and Seed, H.B. (1975) "Fundamentals of liquefaction under cyclic loading." *Journal of the Geotechnical Engineering Division*, ASCE, Vol. 101, No GT5, 423-438.

79. McMeeking, R. M. and Rice, J. R. (1975). "Finite-element formulation for problems of large elastoplastic deformation," *International Journal of Solids and Structures*, Vol. 11, 601-616

80. Mehrabadi, M. M. and Nemat-Nasser, S. (1987). "Some basic kinematical relations for finite deformations of continua." Mechanics of Materials, Vol. 6, 127-138.

81. Miles, S. B. and Ho, C. L. (1999) "Rigorous landslide hazard zonation using Newmark's method and stochastic ground motion simulation", *Soil Dynamics and Earthquake Engineering*, Vol. 18, No. 4, 305-323.

82. Moriwaki, Y., Beikae, M., and Idriss, I. M. (1988). "Nonlinear seismic analysis of the Upper San Fernando Dam under the 1971 San Fernando earthquake." *Proceeding of 9th World Conference on Earthquake Engineering*, Tokyo and Kyoto, Japan, Vol. VIII, 237-241.

83. Muraleetharan, K. K., Mish, K. D., Yogachandran, C. and Arulanandan, K. (1988). "DYSAC2: dynamic soil analysis code for 2-dimensional problems." *Department of Civil Engineering, University of California, Davis*, California.

84. Murata, J. (1984). "Flow and deformation of fresh concrete." *Master. Constr. (Paris).* Vol. 17, 117-129.

85. Nagtegaal, J. C. and De Jong, J. D. (1982). "Some aspects of non-isotropic work-hardening in finite strain plasticity." In *Plasticity of Metals of Finite strain: Theory, Experiment and Computations*, 65-102.

86. Newmark, N, M. (1965). "Effects of earthquakes on dams and embankments." *Géotechnique*, 15(2).

87. Oldroyd, J. G. (1950). "On the formulation of rheological equations of state." *Proc. Roy. Soc.* Vol. 220, 523-541.

88. Olea, R.A. (1999). "Geostatistics for Engineers and Earth Scientists." *Kluwer Academic Publishers*, Boston.

89. O'Rourke, T. D. (1998) "An Overview of Geotechnical and Lifeline Earthquake Engineering", *ASCE Geotechnical Special Publication No. 75*, Reston, VA, Vol. II, 1392-1426.

90. Ortiz, M. and Simo J. C. (1986). "An analysis of a new class of integration algorithm for elastoplastic constitutive relations." *International Journal for Numerical Methods in Engineering*, 23, 353-366.

91. Pashias, N. and Boger, D. V. (1994). Comparison of bauxite suspensions." *7th National Conference on Rheology*, Brisbane, 163-166.

92. Prager, W. (1959). "Introduction to Plasticity." *Addison-Wesley*, Reading, MA.

93. Prevost, J. H. (1995), "DYNAFLOW: A nonlinear transient finite element analysis program." *Technical report*, Dept. of Civil Eng. and Op. Research, Princeton University, Princeton, NJ.

94. Prevost, J. H. 1989 "DYNA1D: A Computer Program for Nonlinear Seismic Site Response Analysis - Technical Documentation." *Multidisciplinary Center for Earthquake Engineering Research,* Report NCEER-89-0025.

95. Raschke, S.A. and Hryciw, R. D. (1997). "Vision Cone Penetrometer (VisCPT) for Direct Subsurface Soil Observation", ASCE Journal of Geotechnical and Geoenvironmental Engineering, Vol. 123, No. 11, pp. 1074-1076.

96. Rauch, A. F. (1997). "EPOLLS: An empirical method for predicting surface displacements due to liquefaction-induced lateral spreading in earthquakes." Ph.D. Dissertation, *Virginia Polytechnic Institute and State University.*

97. Roth, W. H. (1985). "Evaluation of earthquake-induced deformations of Pleasant Valley Dam." *Report for the City of Los Angeles*, Dames & Moore, Los Angeles.

98. Sano, Y. (1998) "GIS Evaluation of Northridge Earthquake Ground Deformation and Water Supply Damage", Master Thesis, Cornell University.

99. Sasaki, Y., Towahata, I., Tokida, K., Yamada, K., Matsumoto, H., Tamari, Y. and Saya, S. (1992). "Mechanism of permanent displacement of ground caused by seismic liquefaction," *Soils and Foundations*, Vol. 32, No. 3, 76-96.

100. Seed, H. B. and Harder, L .F. (1990). "SPT-based analysis of cyclic pore pressure generation and undrained residual strength." *In Proceedings of the H. Bolton Seed Memorial Symposium*, University of California, Berkeley, Vol. 2, 351-376.

101. Seed, H. B. and Idriss, I. M. (1970). "Soil moduli and damping factors for dynamic response analysis." *Report EERC 70-10*, Earthquake Engineering Research Center, University of California, Berkeley, CA.

102. Seed, H.B., Lee, K.L., Idriss, I.M., Makdisi, F. (1973). "Analysis of the slides in the San Fernando dams during the earthquake of Feb. 9, 1971," *Report No.EERC-73/2, Earthquake Engineering Research Center*, University of California, Berkeley, California.

103. Seed, H. B., Lee, K. L., Idriss, I. M. and Makdisi, F. I. (1975). "The slides in the San Fernando Dams during the earthquake of February 9, 1971." *Journal of Geotechnical Engineering, ASCE*, Vol. 101 No. 7, 651-688.

104. Seed, H. B., Tokimatsu, K. and Harder, L. F. (1985) "Influence of SPT Procedure in Soil Lique-faction Resistance Evaluation," *Journal of Geotechnical Engineering*, ASCE, Vol. 111, No. 12, 1425-1445.

105. Serff, N., Seed, H. B., Makdisi, F. I. And Chang, C. Y. (1976). "Earthquake induced deformations of earth dams." *EERC Report No. 76-4*, University of California, Berkeley.

106. Simo, J. C. and Pister, K. S. (1984). "Remarks on rate comstitutive equations for finite deformation problems: Computational implications." *Comput. Methods appl. Mech. Eng.*, Vol. 46, 201-215.

107. Simo, J. C. and Hughes, T. J. R. (1998). “Computational Inelasticity”, *Springer*, New York.

108. Simo, J. C., Taylor, R. L. and Pister, K. S. (1985). “Variational and projection methods for the volume constraint in finite deformation elasto-plasticity.” *Comput. Methods Appl. Mech. Eng.* 51, 177-208.

109. Simo, J. C. and Taylor, R. L. (1991). “Quasi-incompressible finite elasticity in principal stretches. Continuum basis and numerical algorithm.” *Comput. Methods Appl. Mech. Eng.* 85, 273-310.

110. Star, J. L., and Estes, J. E. (1990). “Geographic Information System – An Introduction,” *Prentice Hall*, Englewood, NJ, 303 p.

111. Stark, T.D. and Mesri. G. (1992). “Undrained shear strength of liquefied sands for stability analysis.” *Journal Geotechnical Engineering*, Vol. 118, No. 11, 1727-1747.

112. SVG. (2003). Scalable Vector Graphics v1.1, 2003. URL http://www.w3.org/Graphics/SVG/Overview.htm8

113. Taboata, V. and Dobry, R. (1998). “Centrifuge modeling of earthquake-induced lateral spreading in sand”, *Journal of Geotechnical and Geoenvironmental Engineering*, Vol. 124, No. 12, 1195-1206.

114. Taguchi, Y. and Hamada, M. (1994). “Study on permanent ground displacements due to liquefaction using geotechnical information system”, *Fifth U.S. National Conference on Earthquake Engineering*, Oakland, California, Vol. IV, 179-188.

115. Tanaka, Y. and Okimura, T. (2001) “In-depth Geotechnical Database, Kobe Jibankun, for Seimic Hazard Study”, *COSMOS Workshop on Archiving and Web Dissemination of Geo-technical Data*, Richmond, CA.

116. Tanigawa, Y. and Mori, H. (1986). “Rheological analysis of slumping behavior of fresh concrete,” *Proceedings of the 29th Japan Congress on Materials Research*, 129-136.

117. Tateishi, A., Taguchi, Y, Oka, F. and Yashima, A. (1995). "A Cyclic Elasto-Plastic Model for Sand and Its Application Under various Stress Conditions.” *Proceeding of 1st International Conference On Earthquake Geotechnical. Engineering*, Vol. 1, 399-404, Balkema, Rotterdam.

118. Tattersall, G. H. and Banfill, P. G. F. (1983). “The Rheology of Fresh Concrete.” *Pitman*, London.

119. Ting, T.T. (1985). "Determination of $C^{1/2}$, $C^{-1/2}$ and more general isotropic tensor functions of C," *Journal of Elasticity*, Vol. 15, 319-323.

120. Tokimatsu, K., Mizuno, H., and Kakurai, M. (1996). "Building Damage Associated with Geotechnical Problems." *Soils and Foundations*, Special Issue on the Geotechnical Aspects of the January 17 1995 Hyogoken-Nambu Earthquake, January, 219-234.

121. Towhata, I. and Ishihara, K. (1985). "Shear work and pore water pressure in undrained shear." *Japanese Society of Soil Mechanics and Foundation Engineering, Soils and Foundations*, 25(3), 73-84.

122. Towhata, I., Orense, R. P. and Toyota, H. (1997) "Mathematical principles in prediction of lateral ground displacement induced by seismic liquefaction". *Soils and Foundations*, 39(2), 1-19.

123. Truesdell C. and Noll. W. (1965). "The nonlinear field theories," *Handbuch der Physik, Band III/3, Springer-Verlag*, Berlin.

124. Viescas, J. L. (1997). "Running Microsoft Access 97", *Microsoft Press*, Redmond, Washington 98052-6399.

125. Yang, Z. (2000). "Numerical Modeling of Earthquake Site Response Including Dilation and Liquefaction," *Ph.D. Dissertation*, Columbia U., New York, NY.

126. Yegian, M. K., Marciano, E. A. and Gharaman, V. G. (1991) "Earthquake-induced permanent deformation: probabilistic approach," *Journal of Geotechnical Engineering*, ASCE, Vol. 117, No. 1, 35-50.

127. Youd, T. L. and Perkins, D. M. (1987). "Mapping of Liquefaction Severity Index," *Journal of Geotechnical Engineering Division*, ASCE, No. 11, 1374-1392.

128. Youd, T. L. and Idriss, I. M. (Editors). (1997). "Proceeding of the NCEER Workshop on Evaluation of Liquefaction Resistance of Soils", *NCEER Technical Report NCEER-97-0022*, Buffalo, New York.

129. Youd, T.L., Hansen, C. M. and Bartlett, S. F. (2002) "Revised MLR Equations for Prediction of Lateral Spread Displacement," *Journal of Geotechnical and Geoenvironmental Engineering*, ASCE, Vol. 128, No. 12, 1007-1017.

130. Zienkiewicz, O. C., Chan, A. H. C., Pastor, M., Paul, D. K. and Shiomi, T. (1990). "Static and dynamic behaviour of soils: a rational approach to quantitative solutions: Part I - fully saturated problems," *Proceedings of the Royal Society, Series A*. 429, 285-309.

131. W3 Consortium. (2000). http://www.w3.org.

132. Wackernagel, H. (1995). "Multivariate Geostatistics," *Springer-Verlag*, Berlin Heidelberg, Germany.

133. Wald, D. J. (1996). "Slip history of the 1995 Kobe, Japan, earthquake determined from strong motion, teleseismic and geodetic data," *Journal of Physics Earth*, Vol. 44, 489–503.

134. Whittaker, E. T. (1944). "A treatise on the analytical dynamics of particles and rigid bodies," *Dover*, New York.

135. Wu, G. (2001). "Earthquake-induced deformation analyses of the Upper San Fernando Dam under the 1971 San Fernando Earthquake." *Canadian Geotechnical Journal*, Vol. 38, 1-15.